

---

# System Identification of Optic-Flow Processing Neurons in the Fly: Single Cell and Small Circuit Models

Franz Weber

---



München 2011



---

# **System Identification of Optic-Flow Processing Neurons in the Fly: Single Cell and Small Circuit Models**

Franz Weber

---

Dissertation of the  
the Graduate School of Systemic Neurosciences  
of the Ludwig–Maximilians–Universität  
München  
Submitted by  
Franz Weber

München,  
October 13, 2011

First Reviewer / Supervisor: Prof. Dr. Alexander Borst

Second Reviewer / Supervisor: Dr. Christian K. Machens

Day of Oral Defense: December 8, 2011

# Contents

Summary	viii
<b>1 Introduction</b>	<b>1</b>
1.1 System Identification . . . . .	2
1.1.1 Tuning Curves . . . . .	3
1.1.2 Spike-Triggered Average . . . . .	3
1.1.3 Linear-Nonlinear Model . . . . .	6
1.1.4 Generalized Linear Model . . . . .	7
1.2 The Visual System of the Fly . . . . .	9
1.2.1 Retina and Photoreceptors . . . . .	10
1.2.2 Lamina . . . . .	10
1.2.3 Medulla . . . . .	11
1.2.4 The Lobula Complex . . . . .	12
1.2.5 Circuitry of the Lobula Plate Tangential Cells . . . . .	12
1.2.6 Receptive Fields of the Lobula Plate Tangential Cells . . . . .	17
1.2.7 Processing of Dynamic Motion Stimuli by H1 . . . . .	20
1.3 The Reichardt Detector . . . . .	21
1.3.1 The Structure of the Reichardt Detector . . . . .	21
1.3.2 Evidence for the Reichardt Detector . . . . .	22
1.3.3 Biophysical Implementation of the Reichardt Detector . . . . .	24
1.4 Thesis Projects . . . . .	25
<b>2 Materials and Methods</b>	<b>27</b>
2.1 Visual Stimulation . . . . .	27
2.2 Preparation and Recording . . . . .	28
2.3 Self-Motion Induced Optic-Flow . . . . .	29
2.3.1 Mathematical Description of Optic-Flow . . . . .	29

2.3.2	Comparison of Rotation and Translation . . . . .	31
2.3.3	Optic-Flow Norm . . . . .	32
2.4	Visual Stimuli . . . . .	32
2.4.1	Brownian Motion Stimulus . . . . .	32
2.4.2	Local White-Noise Stimulus . . . . .	33
2.4.3	White-Noise Self-Motion Stimulus . . . . .	34
2.4.4	Random Rotation Stimulus . . . . .	35
2.5	Modeling and Data Analysis . . . . .	36
2.5.1	Modeling an Array of Reichardt Detectors . . . . .	36
2.5.2	Estimation of the Dynamic Receptive Field . . . . .	37
2.5.3	Space-Time Separation of the Dynamic Receptive Field . . . . .	38
2.5.4	Estimation of the Static Nonlinearity . . . . .	39
2.5.5	Biophysically Extended LN-Model . . . . .	39
2.5.6	Estimation of Self-Motion Filters . . . . .	42
2.5.7	Generative Spiking Model . . . . .	43
2.5.8	Evaluation of Firing-Rate Models . . . . .	45
2.5.9	Linear Decoding . . . . .	47
2.5.10	Self-Motion Tuning Maps . . . . .	47
<b>3</b>	<b>Results</b>	<b>49</b>
3.1	The Spatio-Temporal Response Properties of the Tangential Cells . . . . .	49
3.1.1	Processing of Sparse and Dense Motion . . . . .	50
3.1.2	Local Reliability of Motion Processing . . . . .	64
3.2	Self-Motion Encoding by the Tangential Cells . . . . .	68
3.2.1	Responses to the White-Noise Self-Motion Stimulus . . . . .	69
3.3	The Functional Role of an Inter-Hemispheric Projection . . . . .	75
3.3.1	A Generative Spiking Model for Vi and H1 . . . . .	76
3.3.2	H1 Improves the Optic-Flow Representation in Vi . . . . .	82
<b>4</b>	<b>Discussion</b>	<b>93</b>
4.1	Compartmental Modeling and System Identification . . . . .	94
4.2	Space-Time Separability of the Dynamic Receptive Fields . . . . .	96
4.3	LN-Models and Adaptation . . . . .	97
4.4	Gain Modulation in Spiking Neurons . . . . .	98
4.5	Rotation and Translation Encoding by the Tangential Cells . . . . .	100
4.6	Receptive Fields and Generative Models . . . . .	102

4.7	Noise Correlations and Generative Models . . . . .	103
4.8	Dependence of Functional Connectivity on Stimulation Strength . . . . .	104
4.9	Role of Correlations in Sensory Areas . . . . .	105
	<b>Acknowledgments</b>	<b>121</b>



# Summary

Flies heavily rely on optic-flow to maintain a stable course during flight. In the blowfly, the lobula plate comprises about 60 motion-sensitive neurons that process optic-flow information. To characterize these so-called lobula plate tangential cells, I pursued a system identification approach: I recorded the activity of single or pairs of neurons, while presenting optic-flow stimuli of varying complexity. By means of system identification methods, I then estimated single cell or small circuit models describing the processing of optic-flow by the tangential cells.

A standard approach to functionally characterize sensory neurons is the linear-nonlinear (LN) model comprising a linear stage, followed by a nonlinear response function. To estimate the components of an LN-model for optic-flow processing neurons, I presented novel random motion stimuli with individually moving dots. The linear stage can be represented as a time-varying vector field, referred to as dynamic receptive field. I found that the dynamic receptive field can be fully described by a separate spatial and temporal component. Next, I examined the dependence of the LN-model components on the stimulus strength as controlled by the density of motion dots. I found that an increase of the stimulus strength leaves the receptive field unchanged but strongly modulates the gain and selectivity of the response nonlinearity. To correct for these systematic changes, I developed an explicit biophysical model of the neuron's input-output relation, which could account for the neural responses under all stimulus conditions.

To probe how well the optic-flow is encoded by the tangential cells, I presented dynamic rotational and translational self-motions within various environments differing in their textures, while recording the cells' responses. To quantify the encoding of rotational or translational optic-flow, I tested how well the presented rotations or translations can be reconstructed from the recorded spikes. I found that rotations are better encoded in the neural responses than translations. Especially, when simultaneously presenting rotations and translations, the representation of rotations is less affected than the representation of translations.

To understand how the lateral interactions between neurons influence the optic-flow processing, I simultaneously recorded from a pair of tangential cells (left Vi and right H1 cell) while presenting dynamic, rotational self-motion stimuli. To characterize the functional connectivity between Vi and H1, I fitted a generalized linear model (GLM) to the recorded responses. The GLM can be interpreted as an extension of the LN-model which accounts for lateral interactions between the recorded neurons. The GLM revealed a uni-directional coupling from H1 to Vi. Further analysis showed that the coupling improves the optic-flow encoding in Vi by increasing the gain of its rotation tuning. Interestingly, the coupling between Vi and H1 is adjusted to a value such that the information per spike is maximized in Vi.

Hence, by the applied system identification approach, I characterized the dynamic receptive fields of the tangential cells, tested the robustness of the optic-flow encoding, and studied how the neural connectivity improves the optic-flow processing.

# Chapter 1

## Introduction

Animals move with ease through their surrounding three-dimensional environment. Primates including ourselves as well as flies thereby heavily rely on vision. First ideas on the importance of vision for stable navigation through our world have been formulated by von Helmholtz (1925). Gibson coined the term 'optic-flow' for the motion pattern on the retina, when we move relative to the world (Gibson, 1950). Figure 1.1 illustrates the optic-flow resulting from a forward translation. For stable navigation, the nervous system has to estimate from the retinal optic-flow pattern the self-motion. In an ideal world with constant velocities and homogeneous distances between the animal and the surrounding objects, this problem is well-posed: In this case, each optic-flow pattern corresponds unambiguously to a combination of a specific rotation and translation (Koenderink and van Doorn, 1987). The difficulty of self-motion perception arises from the inhomogeneous depth structure of natural environments, their strongly differing textures and contrast distributions, all disturbing the ideal optic-flow pattern (Franz et al., 2004).

The processing of optic-flow stimuli has been intensively studied in flies (for review see (Borst et al., 2010)). The lobula plate in the visual system of the fly comprises neurons which preferentially respond to specific optic-flow patterns Hausen (1984); Krapp and Hengstenberg (1996). To characterize these so-called lobula plate tangential cells, motion stimuli of varying complexity have been presented in the past, while recording the neural responses (see e.g. (Krapp et al., 1998; Borst, 2003; Haag and Borst, 2003; Wertz et al., 2009; van Hateren et al., 2005)). Various types of models have been formulated to describe how the stimuli are processed by the tangential cells.

The general term system identification has been coined for approaches trying to unravel how sensory stimuli are transformed to the recorded, neural response (Wu et al., 2006; Marmarelis and Marmarelis, 1978). All models falling under this term share one common



**Figure 1.1: Illustration of Optic-Flow.** Self-motion causes a permanent shift of the images on the retina. The resulting pattern of local velocities (represented by the arrows) is called optic-flow. The image illustrates the optic-flow induced by a forward translation.

feature: They are all top-down models derived from the recorded responses. Hence, the main focus is not a detailed physiological description of the recorded neurons, but rather a phenomenological characterization how an input (stimulus) is mapped to the output (response). The resulting input-output model characterizes the neural processing in functional terms. By means of system identification, I characterized the lobula plate tangential cells. Single cell as well as small circuit models were estimated to describe how dynamic optic-flow stimuli are processed by these neurons. In the following, I will introduce basic concepts of system identification and then review the visual system of the fly as well as the Reichardt detector, a well-established model for local motion detection.

## 1.1 System Identification

To understand how sensory systems operate, neuroscientists have long sought to quantify how single neurons or populations of neurons respond to sensory stimuli. Most models in sensory neuroscience are based on experiments, where tightly controlled stimuli are presented to the animal, while recording the responses of sensory neurons. Quantitative analysis of the recorded data aims at characterizing the functional relationship between stimuli and neural responses. This approach yielded a large variety of computational and quantitative models describing all kinds of sensory systems in different animals including insects and vertebrates (for review see (Dayan and Abbott, 2001; Rieke et al., 1999; Wu et al., 2006)). The large number of different studies makes it difficult to describe a general methodology summarizing all previously developed models. Nevertheless, there were different attempts to formulate a unifying framework applying to all kinds of models (Wu et al., 2006; Rieke et al., 1999). Typically, models in sensory neuroscience are derived from

a classical input-output analysis: Giving the known input to the system and its recorded output, the goal is to find a simple, general model transforming the input to the output. In the engineering literature such a phenomenological characterization is called system identification, a term also used for input-output models in neuroscience by Wu et al. (2006); Marmarelis and Marmarelis (1978). Other terms describing the same basic approach are receptive field estimation (Aertsen and Johannesma, 1981; DeAngelis et al., 1995), reverse correlation (Ringach et al., 1997; Haag and Borst, 1997), spike-triggered neural characterization (Schwartz et al., 2006), or white-noise analysis (Chichilnisky, 2001), each stressing another aspect of the applied methodology. Here, I will not try to add another general framework. Instead, I will introduce basic concepts and approaches which have been widely and successfully applied as well as recent attempts to characterize the responses of neural populations.

### 1.1.1 Tuning Curves

A standard tool to characterize the stimulus selectivity of single neurons is the neural tuning curve (Butts and Goldman, 2006; Dayan and Abbott, 2001), a plot of the average firing rate of single neurons in dependence of one or two stimulus parameters. The stimuli to determine tuning curves are typically very restricted. Tuning curves have long served as an invaluable tool to characterize neurons in virtually every sensory system ranging from the olfactory system (Wilson et al., 2004), visual system (Henry et al., 1974), motion-sensitive neurons in monkeys (Albright, 1984) and flies (Haag and Borst, 2003) to the wind-detection system in crickets (Theunissen and Miller, 1991). As an example, Figure 1.2A shows the extracellular recording of a single neuron in the monkey visual cortex, while presenting a light bar moving at different orientations. The number of action potentials fired depends on the orientation of the bar. Figure 1.2B illustrates the same effect by a tuning curve, showing the mean firing rate of a neuron in cat visual cortex in dependence of the bar orientation.

### 1.1.2 Spike-Triggered Average

Due to time limitations during experiments, the number of different stimuli which can be presented to reliably estimate tuning curves is restricted. The spike-triggered average (STA), an approach to increase the number of presented stimuli, is complementary to the tuning curve: Instead of averaging the neural responses for a given set of stimuli, the STA represents the average of stimuli for a given response (Dayan and Abbott, 2001). A typical

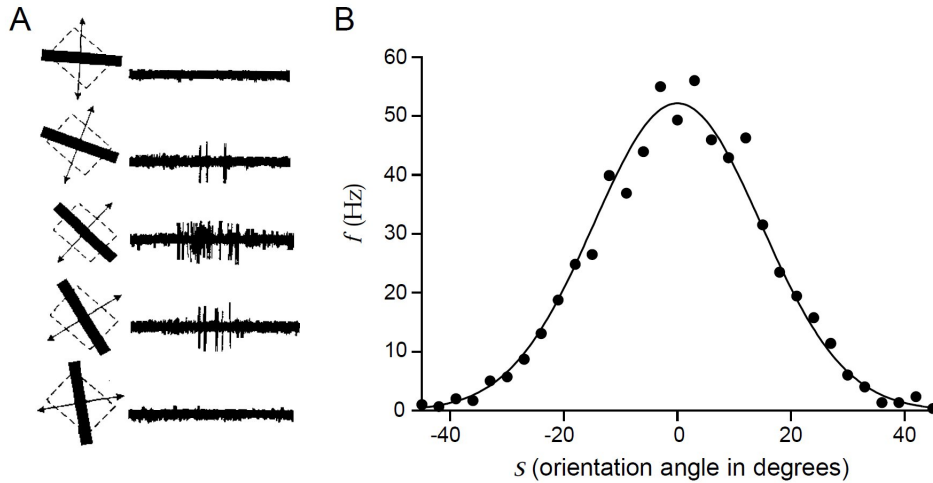


**Figure 1.2: Characterizing Neurons by their Stimulus Tuning** (A) Extracellular recording of a neuron in monkey visual cortex. A light bar was moved across the receptive field (dashed rectangle) of a single neurons. The orientation of the light bar is indicated by the black bar. The traces on the right show the extracellularly recorded activity. (B) Tuning curve of a neuron in cat visual cortex. Each dot represents the average firing rate for the bar orientation indicated on the x-axis. The figure is taken from Dayan and Abbott (2001). The data for (A) originally stems from Hubel and Wiesel (1968). The data for (B) was originally taken from Henry et al. (1974).

choice for the response is the appearance of a spike. The spike-triggered average then describes the average stimulus which makes the neuron most likely spike. At the expense of reducing the range of responses to 'spike' or 'no spike', this approach allows largely enriching the set of presented stimuli.

Since tuning curves are calculated by averaging the neural response for given set of stimuli, any dynamics present in the response is averaged out. Moreover, the chosen stimuli are typically restricted in their dynamics. E.g. for the neural tuning depicted in Figure 1.2 a light bar was moved at constant velocity across the receptive field. Contrarily, the STA describes dynamic aspects of stimulus processing. It is typically computed for stimuli that strongly vary over time. Hence, the STA describes the average stimulus waveform or fluctuation preceding a spike.

The calculation of the STA is illustrated in Figure 1.3A: At each time point the presented stimulus consists of an array of randomly chosen pixel values. It is assumed that, for each time point, the neural response is completely determined by the preceding stimulus. The stimulus intervals preceding a spike are marked by red boxes. Averaging all stimuli preceding a spike yields the STA. In the example, the STA represents a spatio-temporal

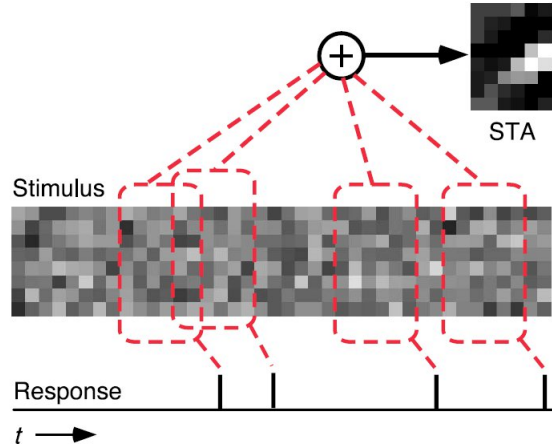


**Figure 1.3: Illustration of Spike-Triggered Average.** The stimulus consists of an array of eight pixels, randomly changes their values at each time point. The neural response is schematically represented as a time axis (bottom). Each time point where a spike was fired is indicated by a black tick. Stimulus intervals preceding a spike are marked by red boxes. The stimulus intervals extend over 6 time steps, and, thus, comprise 48 spatio-temporal pixel values. Averaging all spike-triggered stimuli yields the spike-triggered average. Figure taken from (Schwartz et al., 2006).

matrix describing how, in average, the values of the pixel array evolve in time before a spike is elicited.

Formally, if the recorded neuron fired  $n$  spikes at time points  $t_i$ ,  $i = 1, \dots, n$ , the STA  $C(\tau)$  can be written as

$$C(\tau) = \frac{1}{n} \int_0^T dt s(t - \tau) r(t) = \frac{1}{n} \sum_{i=1}^n s(t_i - \tau) \quad (1.1)$$

with  $s(t)$  describing the time varying stimulus presented for  $T$  seconds. The function  $r(t)$  represents the neural response function, which is 1, if the neuron fired a spike at a time point  $t$ , and 0 otherwise. The first Equality of equation 1.1 can be interpreted as cross-correlation of the presented stimulus and the recorded response.

The STA allows predicting the response of the neuron given the stimulus  $s(t)$ : The more similar a particular waveform to the STA, the more likely it is that the neuron will fire a spike. The firing rate of the neuron at time  $t$  can be estimated by convolving the stimulus with the STA,

$$\hat{r}(t) = r_0 + \int_0^\infty d\tau C(\tau) s(t - \tau), \quad (1.2)$$

where  $r_0$  accounts for the neuron's background firing, when  $s = 0$ .

So far, the STA has been intuitively introduced as the average stimulus waveform preceding a spike. A more formal justification of Equation 1.2 is to consider the STA as the linear kernel in a Volterra expansion (Rieke et al., 1999; Dayan and Abbott, 2001).

The Volterra expansion is the functional equivalent of the Taylor series. It allows expressing the neural response,  $r(t)$ , in powers of the stimulus  $s(t)$ ,

$$\begin{aligned} r(t) = r_0 & \int d\tau C(\tau) s(t - \tau) + \int d\tau_1 d\tau_2 C_2(\tau_1, \tau_2) s(t - \tau_1) s(t - \tau_2) \\ & + \int d\tau_1 d\tau_2 d\tau_3 C_3(\tau_1, \tau_2, \tau_3) s(t - \tau_1) s(t - \tau_2) s(t - \tau_3) + \dots \end{aligned} \quad (1.3)$$

Comparison with Equation 1.2 shows that the STA corresponds to the first linear filter in the Volterra expansion.  $C(\tau)$  is also called the first Wiener kernel or the linear receptive field. It can be shown that, if  $s(t)$  is a white-noise stimulus, the STA equals  $C(\tau)$  (Dayan and Abbott, 2001).

Note that the estimate of the firing rate by Equation 1.2 is a linear function of the stimulus. This linear estimate suffers from two obvious problems: The predicted firing rate can become negative and does not saturate for large stimulus values. One way to overcome these problems is to include higher-order kernels in the prediction. However, to reliably estimate higher order kernels, increasing amounts of data are needed. Practically, only estimates up to the second-order kernel are feasible (Dayan and Abbott, 2001).

### 1.1.3 Linear-Nonlinear Model

A simpler approach to account for basic nonlinearities as spike-rate saturation or non-negative firing rates is to include a static nonlinearity  $f$  into Equation 1.2,

$$\hat{r}(t) = f \left( r_0 + \int_0^\infty d\tau C(\tau) s(t - \tau) \right). \quad (1.4)$$

The resulting model consists of a cascade of the linear filter  $C(\tau)$  and the nonlinearity  $f$ , and is therefore referred to as linear-nonlinear (LN) model illustrated in Figure 1.4. To simulate a spike train, the estimated firing rate can be used to drive a Poisson generator whose rate is determined by the output of the nonlinearity. Using a Poisson distribution to generate spikes, it is implicitly assumed that the appearance of a spike only depends on the recent stimulus and not on the history of previous spikes (Schwartz et al., 2006; Dayan and Abbott, 2001).

LN-models have been successfully applied to describe the stimulus processing in a variety of sensory areas as the retina (Berry and Meister, 1998), lateral geniculate nucleus (LGN)

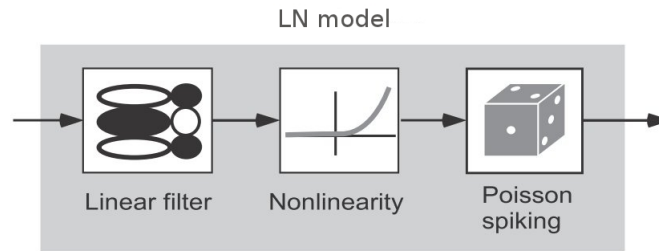


**Figure 1.4: Linear-Nonlinear Model.** In the LN-model the stimulus is first convolved with a linear filter (receptive field). The output of the linear filter is then fed through a nonlinearity yielding the time-variable firing rate. To generate spikes, the firing rate can be used to drive a Poisson generator. Figure taken from (Schwartz et al., 2006).

(DeAngelis et al., 1995; Lesica et al., 2007), visual cortex (Ringach et al., 1997), the auditory system (Aertsen and Johannesma, 1981; Linden et al., 2003), the olfactory system in crickets (Geffen et al., 2009), or the visual motion system in flies (Haag and Borst, 1997). However, especially at more central cortical stages, these models often show a poor performance in predicting the neural responses (Machens et al., 2004; Linden et al., 2003; David et al., 2004). A reason for this might be that central neurons are more nonlinear than peripheral ones (Carandini et al., 2005) and that their responses often strongly depend on the behavioral state of the animal (Reynolds and Chelazzi, 2004; Atiani et al., 2009). A further problem might be that, in the LN-model, the response depends only on the stimulus. Hence, recurrent interactions between sensory neurons are not explicitly accounted for. Instead, the LN-model describes the receptive field of a single neuron as arising from its feedforward inputs from the sensory organ and recurrent inputs from other neurons.

#### 1.1.4 Generalized Linear Model

In principle, a whole population of neurons could be modeled by a population of LN-models fitted independently to each of the recorded neurons. However, simultaneous recordings of pairs of neurons revealed that the responses of sensory neurons are typically correlated (Zohary et al., 1994; Pillow et al., 2008; Bair and Movshon, 2004; Kazama and Wilson, 2009; Cafaro and Rieke, 2010; Kohn and Smith, 2005; Smith and Kohn, 2008; Schneidman et al., 2006; Schulz and Carandini, 2010; Trong and Rieke, 2008). Such correlations in the spike trains of simultaneously recorded neurons cannot be reproduced by a population of LN-models, since in each LN-model spikes are generated independently by a Poisson generator. A model accounting for dependencies between neurons, the so-called generalized

linear model (GLM), was developed by (Paninski et al., 2007; Pillow et al., 2008; Okatan et al., 2005; Gerwinn et al., 2010).

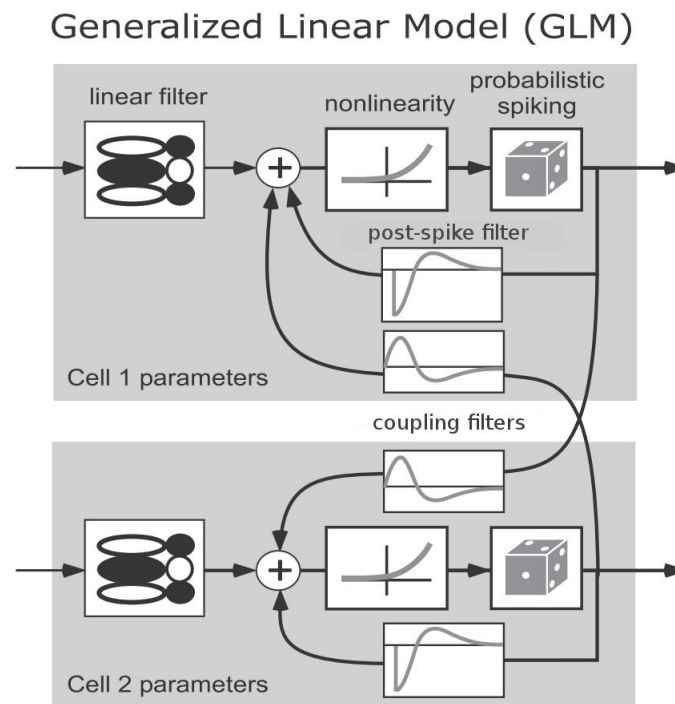


**Figure 1.5: Generalized Linear Model.** The scheme illustrates a generalized linear model (GLM) to simulate a two-neuron circuit. The stimulus dependency of each neuron is modeled by a linear filter. The impact of each neuron’s own spiking history is modeled by the post-spike filter. Interactions between the neurons are captured by the coupling filters. The outputs of the three linear filters are summed and transformed by a static nonlinearity to the firing rate, which drives a Poisson generator to simulate spike trains. Figure taken and modified from Paninski et al. (2007).

In Figure 1.5, the GLM is illustrated for a two-neuron circuit. As in the LN-model, the stimulus dependency of each neuron’s firing rate is modeled by a linear filter. Spike trains generated by a LN-model with a Poisson generator do not account for the refractory period or further history dependent effects as bursting (Pillow et al., 2005; Paninski et al., 2007). To account for the impact of previous spikes on the neuron’s firing rate, the preceding spike train is convolved with the post-spike filter (see Figure 1.5). Interactions between the neurons are captured by two further linear filters, the coupling filters. For each neuron, the outputs of the three linear filters are summed and then fed through a static nonlinearity yielding an estimate of the firing rate. To generate spikes, the firing rate is used to drive a Poisson generator. The GLM has been successfully applied to reproduce correlations between retinal ganglion cells (Pillow et al., 2008), to model neural interactions in the

monkey and human sensorimotor cortex (Truccolo et al., 2010) and to elucidate the role of feedback in the thalamus (Babadi et al., 2010).

## 1.2 The Visual System of the Fly

Visual processing in the fly starts with the photoreceptors in the retina (see Figure 1.6). The photo-receptors send axons into the first neuropile, the lamina. From there, motion information is transmitted through the outer optic chiasm to the second visual neuropile, the medulla. The axons of the medullar neurons finally project through inner chiasm to the second neuropile, the lobula complex, consisting of the lobula and the lobula plate. The lobula plate comprises about 60 motion-sensitive neurons known as lobula plate tangential cells. Lamina, medulla, and the lobula complex are all organized into retinotopically arranged columns. Due to this retinotopic organization, the neighborhood relationships of points in visual space are preserved throughout the visual system. Thus, each neuropile represents a retinotopic map, where light emitted from two neighboring spots induces activity in neurons within two neighboring columns.

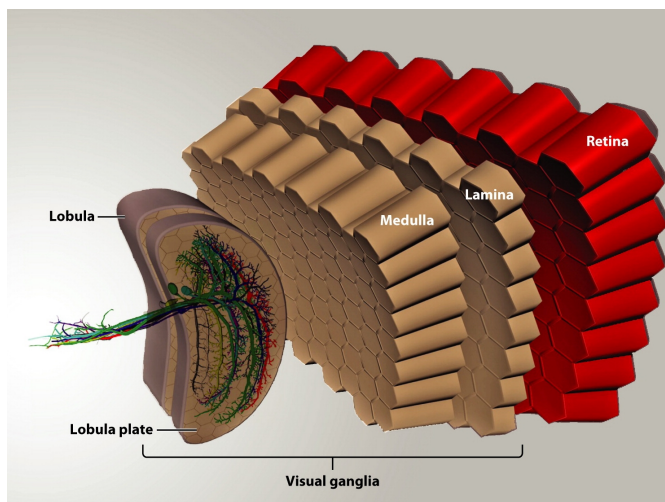


**Figure 1.6: Anatomy of the Fly Visual System.** Scheme illustrating the anatomy of the fly visual system. The visual system is retinotopically arranged. From the retina axons project to the lamina. Neurons of the next neuropile, the medulla, synapse to the lobula and the lobula plate forming the lobula complex. Within the lobula plate the synaptic output of pre-synaptic elements are integrated by the motion-sensitive tangential cells. The colored neurons represent detailed anatomical reconstructions from 2-photon image stacks of the ten VS-cells. The dendrites of the tangential cells run perpendicular to the columns. Figure taken from Borst et al. (2010).

### 1.2.1 Retina and Photoreceptors

The compound eye of the blowfly comprises about 5000 hexagonal ommatidia (Strausfeld, 1984). The angular separation between the optical axes of two neighboring ommatidia is inhomogeneously distributed across the visual field (Petrowitz et al., 2000): The interommatidial angle is smallest at the equator in the frontal visual field (about  $1^\circ$ ). The spatial resolution is about two times lower in the caudal part and up to three times lower in the dorsal part of the visual field. In the frontal visual space the optical axes of both eyes overlap, i.e. the most frontal ommatidia of the left eye sample regions on the right side of visual space and vice versa. In the blowfly, this binocular overlap region extends up to  $15^\circ$  on the contralateral side (Beersma et al., 1977).

Each ommatidium comprises one lens and eight photoreceptors. The lens consists of a cornea and a cone. Light is guided through these structures before hitting the light-absorbing pigments in the photoreceptors. Rhodopsin 1 serves as light-absorbing photopigment in R1-R6 with greatest sensitivity in the UV and green range (O'Tousa et al., 1985). Contrarily, the rhodopsins in R7 and R8 exhibit different absorption spectra indicating a role in color vision (Cook and Desplan, 2001). The photoreceptors R1-R6 are arranged as an outer ring with R7 and R8 in the center. Consequently, each of the photoreceptors R1-R6 has a different optical axis (Land, 1997). The six photoreceptors of six neighboring ommatidia looking at the same spot in visual space send their axons to the same post-synaptic target in the lamina (Braitenberg, 1967). This arrangement, called neural superposition, increases light sensitivity without affecting the eye's spatial resolution (Kirschfeld, 1972). It has been shown that the photoreceptors R1-R6 are involved in motion processing (Heisenberg and Buchner, 1977; Yamaguchi et al., 2008), while R7 and R8 mediate color vision (Gao et al., 2008; Yamaguchi et al., 2010). In contrast to R1-R6, the axons of R7-8 do not project to the lamina, but directly target neurons in the medulla.

### 1.2.2 Lamina

The lamina represents the first neuropile of the visual system. It exhibits a highly regular structure arising from the assembly of identical, columnar units, the so-called cartridges. The columnar structure of the lamina preserves retinotopy, i.e. two neighboring cartridges correspond to two neighboring points in visual space. The so-called monopolar cells L1-L3 and an amacrine cell are directly innervated by the photoreceptors R1-R6 (Meinertzhagen and O'Neil, 1991). Contrarily, the monopolar cells L4 and L5 receive indirect input via L2 and the amacrine cell (Meinertzhagen and O'Neil, 1991; Braitenberg, 1970). The axons of

the monopolar cells project to the medulla. L1 innervates the layers M1 and M5 of the medulla, whereas L2 synapses to the medullar layer M2 (Bausenwein and Fischbach, 1992). By measuring calcium signals in the terminals of L2, it could be shown that L2 is not sensitive to motion direction (Reiff et al., 2010). Calcium signals showed a strong response to brightness decrements (off-signals), but not to increments (on-signals). Hence, L2 rectifies the input from the photoreceptors, thereby only providing information about decrements in the brightness signal to its post-synaptic targets in the medulla. By specifically blocking the synaptic output of L1 or L2, a recent study found that these monopolar cells constitute two functionally different pathways (Joesch et al., 2010): Blocking L1, lobula plate tangential cells show no response to moving on-edges (on-signals). Contrarily, if the output of L2 is blocked, tangential cells mainly only respond to moving off-edges (off-signals). These experiments demonstrate that L1 feeds into an on-channel, whereas L2 provides input to a separate off-channel.

### 1.2.3 Medulla

The next neuropile is the medulla, where the important computations involved in motion-processing are thought to take place. The medulla is built of retinotopically arranged columns, which are divided into ten layers. The number of medullar columns matches the number of cartridges in the lamina. Each column is innervated by the axons of the photoreceptors R7 and R8 and by the laminar monopolar cells L1-L3. In total, each column comprises more than 60 medullar or trans-medullar cells which inter-connect the medullar layers or project to downstream structures (Strausfeld, 1976; Fischbach and Dittrich, 1989). The medulla is the first stage in the visual system where the computation of motion could be experimentally demonstrated: Using the activity-dependent 2-deoxyglucose staining technique, it could be shown that motion stimulation lead to a layer-specific staining of the medulla (Bausenwein and Fischbach, 1992; Bausenwein et al., 1992). During whole-field stimulation layers M1, M2, M9, and M10 were labeled, while stimulation by a single bar resulted in the staining of layers M1, M5, and M7. This finding suggests the presence of various parallel motion pathways specialized for different motion types.

The separation in on- and off-channels at the level of the lamina anatomically persists in the medulla. The laminar monopolar cell L1 (on-channel) innervates the medullar layers M1 and M5, where it connects to the dendrites of the medullar Mi1-cell (Bausenwein and Fischbach, 1992). This cell, in turn, synapses onto T4-cells projecting to the lobula plate. L2, the laminar input to the off-channel, connects in the medullar layer M2 to the Tm1-cells. These neurons synapse in the lobula onto the T5-cells, which send their axons into

the lobula plate.

### 1.2.4 The Lobula Complex

The axons of medullar neurons target the lobula complex, which comprises two structures: the lobula and the lobula plate. As the pre-synaptic neuropiles, the lobula exhibits a retinotopic columnar organization. However, compared to the medulla, it comprises less columns reducing the visual resolution (Strausfeld, 1989) and consists of only six different layers. By means of the 2-deoxyglucose technique, it could be shown that three layers of the lobula are sensitive to motion stimuli (Buchner et al., 1984). The most posterior layer of the lobula is part of the presumable off-channel: The axons of the medullar Tm1 cells, which are connected to L2, synapse within this layer onto the dendrites of the T5 cells.

As the lobula, the lobula plate is organized into retinotopic columns, but comprises only four layers. Activity dependent labeling by the 2-deoxyglucose technique demonstrated that the four layers are responsive to four different motion-directions (Buchner et al., 1984; Bausenwein and Fischbach, 1992; Bausenwein et al., 1992): Neurons in the two anterior layers respond to horizontal motion (front-to-back, back-to-front), whereas the activity in the two posterior layers represents vertical motion (up and down).

The synaptic outputs of the columnar elements are integrated by the motion-sensitive lobula plate tangential cells (Hausen, 1984; Hengstenberg et al., 1982). The dendrites of the tangential cells run orthogonal to the columns and cover several hundred columns. The layer where the dendrite of a specific tangential cells ramifies determines the neuron's preferred motion-direction. The motion-sensitivity of the tangential cells arises from the integration of pre-synaptic motion-sensitive elements. Possible candidates are the T4 and T5 cells, since both cells exhibit directionally selective responses to moving gratings (Douglass and Strausfeld, 1995, 1996). Moreover, in Strausfeld and Lee (1991) a chemical synapse between a tangential cell and T4 could be identified.

### 1.2.5 Circuitry of the Lobula Plate Tangential Cells

The lobula plate comprises about 60 interneurons, which integrate on their dendrites the synaptic outputs of several hundred columns. These lobula plate tangential cells are ideally suited for electrophysiological experiments, since they are large and identified, i.e. the same cell can be found in every fly. Especially, the area within the lobula plate covered by the dendrite of a specific cell is stereotyped across flies, while the detailed branching pattern of the dendrites is less conserved (Cuntz et al., 2008). By ablation experiments it

could be shown that the tangential cells are involved in the optomotor response of the fly (Heisenberg et al., 1978; Geiger and Naessl, 1981; Hausen and Wehrhahn, 1983). Many of the tangential cells synapse onto descending neurons, which directly connect to and control muscles or provide optic-flow information to the thoracic ganglion involved in motor control (Strausfeld and Seyan, 1985; Strausfeld et al., 1987; Huston and Krapp, 2008).

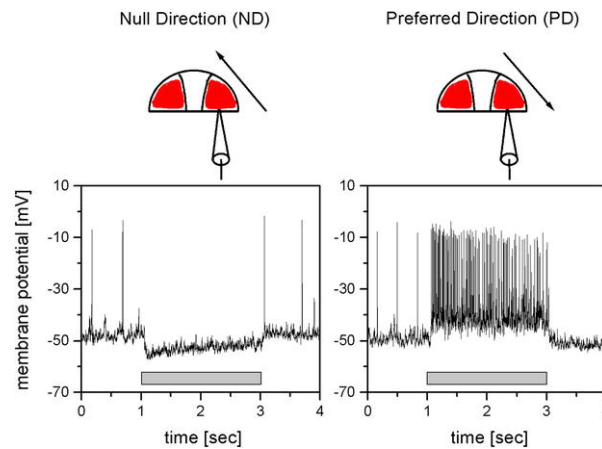


**Figure 1.7: Intracellular Recording of an HSE-cell.** Back-to-front motion hyperpolarizes the cell, whereas front-to-back motion leads to a graded shift of the membrane potential overlaid with spikes of irregular amplitude. The gray bars indicates the time interval where the motion stimulus was presented. The motion direction is schematically shown by the black arrows. Figure taken from Borst and Haag (2002).

The most characteristic feature of the lobula plate tangential cells is their directionally selective response to visual motion. Figure 1.7 shows an example recording of a tangential cell (HSE cell). This neuron responds to back-to-front motion (null direction) with a hyperpolarization of its membrane potential. Contrarily, motion in the opposite direction (preferred direction) leads to a depolarization overlaid with spikes of irregular amplitude. The lobula plate tangential cells can be grouped according to their different response characteristics (Borst and Haag, 2002): (1) They can be categorized according to their overall preferred direction: whether they respond mainly to horizontal or vertical motion. (2) Another distinguishing feature is the response mode: One group of tangential cells responds to motion in their preferred direction by a graded shift of the membrane potential, while others respond with an increase of their frequency of action potentials, and a third group with a mixture of both modes (see Figure 1.8). (3) Finally the tangential cells can be classified according to their projection area: A first group of tangential cells projects with their axon to the contralateral brain hemisphere (heterolateral tangential cells), while

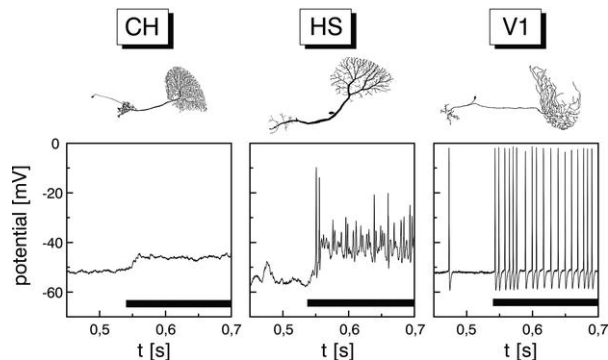


**Figure 1.8: Response Modes of the Tangential Cells.** The lobula plate tangential cells can be grouped according to their response modes to visual motion. One group of tangential cells responds to motion in their preferred direction by a graded shift of the membrane potential. An example is the CH cell (left). The HS cell (middle) is a representative of the second group which responds to a preferred stimulus with a depolarization of the membrane potential overlaid with action potentials of variable amplitude. The V1 cell (right) is an example of a tangential cell firing full-blown action potentials. A preferred stimulus increases the frequency of action potentials. Figure taken from Borst and Haag (2002).

the axons of others remain on the ipsilateral side (ipsilateral tangential cells). The lobula plate tangential cells exhibit a complex recurrent connectivity (Borst and Haag, 2002; Borst et al., 2010; Borst and Weber, 2011). All well characterized tangential cells and their known connectivity are schematically depicted in Figure 1.9.

When categorizing the tangential cells according to their preferred direction, they fall into two groups: Horizontal (H) and vertical (V) cells. The dendrites of the horizontal cells lie within the anterior layer of the lobula plate. Among those are the three horizontal system (HS) cells, which are sensitive to motion in the upper, equatorial, and lower part of the visual space (Hausen, 1982a,b). They are accordingly named the northern (HSN), equatorial (HSE), and southern horizontal (HSS) cell. The HS cells respond to front-to-back motion in their receptive field with a depolarization of their membrane potential overlaid by action potentials of variable amplitude (see Figure 1.8) and are hyperpolarized by motion in the opposite direction.

The three HS cells form electrical synapses with the two centrifugal horizontal (CH) cells (Eckert and Dvorak, 1983). HSN and HSE are indirectly coupled to each other via the dCH cell, whereas vCH connects to HSE and HSN. As the HS cells, the CH cells are also mainly sensitive to front-to-back motion. Both neurons are an example for tangential cells encoding motion in their preferred direction by a graded shift of the membrane potential (Figure 1.8).

Further representatives of the horizontal cells are the neurons H1, H2, H3, and H4 (Hausen,

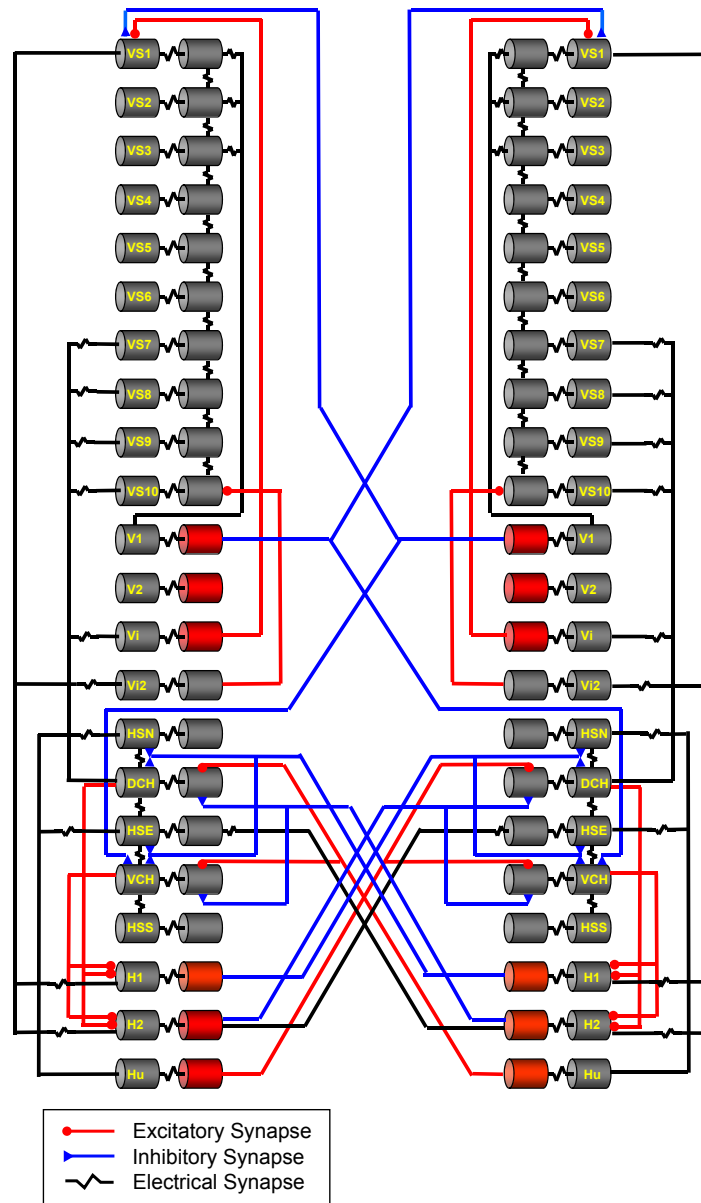


**Figure 1.9: Circuitry of the Lobula Plate.** Circuit diagram of a network simulation of the left and right lobula plate involving 22 well characterized neurons and their connectivity. Each neuron comprises two compartments depicting their axon and dendrite (the labeled compartment). The axons of spiking tangential cells are drawn in red. Representing neurons by two compartments allows categorizing interactions into axo-axonal, dendro-dendritic and axo-dendritic connections. The connection type (electrical synapse, excitatory or inhibitory chemical synapse) are depicted by black, blue, or red lines (see legend). The neurons V2, Vi2 and Hu are not mentioned in the text. The connectivity of V2, a spiking neuron, is unknown. So far, there exist no direct electrophysiological recordings of Hu, however its existence can be concluded from inhibitory postsynaptic potentials (ipsp) in CH (Haag and Borst, 2001). The purely hypothetical neuron Vi2 is assumed to mediate the observed inhibition of VS10 by VS1. Figure taken and modified from Borst and Weber (2011).

1984) which are heterolateral neurons projecting with their axon to the contralateral lobula plate. In contrast to the CH and HS cells, H1-H4 fire full-blown action potentials and respond to motion in their preferred direction by an increased frequency of action-potentials. The response properties and connectivity of H1 and H2 are well characterized. Both neurons preferentially respond to back-to-front motion. They form excitatory synapses with the contralateral HS (Horstmann et al., 2000; Farrow et al., 2006) and CH cells (Hausen, 1984; Haag and Borst, 2001) and are inhibited by the ipsilateral CH cells (Haag and Borst, 2001).

The group of vertically tuned cells comprises, among others, a population of ten so-called vertical system (VS) cells (Hengstenberg et al., 1982). The dendrites of the VS cells are sequentially positioned within the lobula plate, where VS1 has the most lateral and VS10 the most medial dendrite (see Figure 1.11A). Detailed compartmental models of the VS cells are depicted in Figure 1.6. All VS cells preferentially respond to downward motion and are inhibited by upward motion. They encode the motion direction by a graded shift of the membrane potential. According to the retinotopic arrangement of the lobula plate, their receptive fields are sequentially arranged, thus nearly covering half of the visual space. VS1 has a frontal receptive field, whereas VS10 responds to caudal motion (Krapp et al., 1998).

The connectivity of the VS cells has been revealed by intracellular double recordings (Haag et al., 2004): Each VS cell is electrically coupled to its neighbors via axo-axonal gap junctions (see Figure 1.9). Moreover, this chain-like network exhibits a mutual end-to-end inhibition. Current injections into VS1 lead to a hyperpolarization of the proximal VS cells (VS7-VS10). Contrarily, a current injection into VS10 resulted in an inhibition of VS1 (Haag et al., 2004). The circuitry underlying the inhibition of VS1 by the proximal VS cells was revealed in Haag and Borst (2007). VS7-VS10 are electrically coupled to the dendrite of Vi, a heterolateral, spiking tangential cell. Vi's dendrite is inhibitorily coupled to VS1. The neuron mediating the inhibition in the opposite direction is still unknown.

Lateral interactions between tangential cells are not restricted to pairs of neurons that belong to the same group. E.g. the proximal VS cells which belong to the vertical group of neurons, are electrically coupled to dCH, a representative of the horizontal neurons (Haag and Borst, 2007). Another interaction between the horizontal and vertical system is the electrical coupling between H1 and V1 (Haag and Borst, 2003), a further heterolateral, spiking neuron (see Figure 1.8), which is connected via electrical synapses to VS1-VS3 (Kurtz et al., 2001; Haag and Borst, 2008). Further interactions among the tangential cells are depicted in Figure 1.9.

### 1.2.6 Receptive Fields of the Lobula Plate Tangential Cells

The lobula plate tangential cells are sensitive to visual motion. A rough characterization of their direction tuning is given by their preferred and null direction as exemplarily shown for the HSE cell in Figure 1.7. An approach which allows describing the receptive field

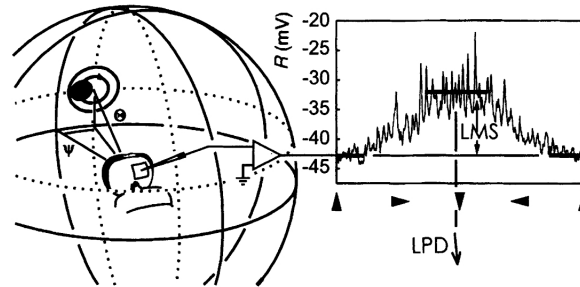


**Figure 1.10: Determining the Spatial Receptive Fields of the Tangential Cells.** (Left) A black dot moves with constant speed along a circular path. (Right) The local preferred direction (LPD) and sensitivity for a particular location is inferred from the neural response after correcting for the neural response delay. The local preferred direction corresponds to the maximum response, the sensitivity is defined as the difference between maximum and minimum response. Figure taken from Krapp and Hengstenberg (1996).

properties of the tangential cells in much more detail was applied in Krapp and Hengstenberg (1996); Krapp et al. (1998, 2001). For this purpose, a small rotating dot was shown at various positions of the visual field, while recording the response of a tangential cell (see Figure 1.10). After correcting for the response delay, the local preferred direction and sensitivity could be determined from the neural response, and were represented as the direction and length of a vector. Repeating this procedure for several locations yields a vector field describing the arrangement of local motion sensitivities. Strikingly, these receptive fields strongly resemble optic-flow fields as induced by certain self-motions. Figure 1.11C shows the receptive fields of VS4, VS7, and VS8 which all exhibit curly vector fields as induced by specific rotations of the fly. The rotation axes inducing the flow fields best matching the receptive fields are depicted in Figure 1.11B. The strong resemblance of the receptive fields with the optic-flow patterns gave rise to the hypothesis that the tangential cells act as matched filters (Franz and Krapp, 2000; Franz et al., 2004): The actual self-motion of the fly is encoded by the cell whose receptive field best matches the resulting optic-flow field and therefore responds most strongly.

The receptive fields determined by the rotating dot stimulus are derived from local stimulation. Whether the receptive field estimated using a local stimulus correctly predicts the preferred rotation axis during global stimulation was tested in Wertz et al. (2009).

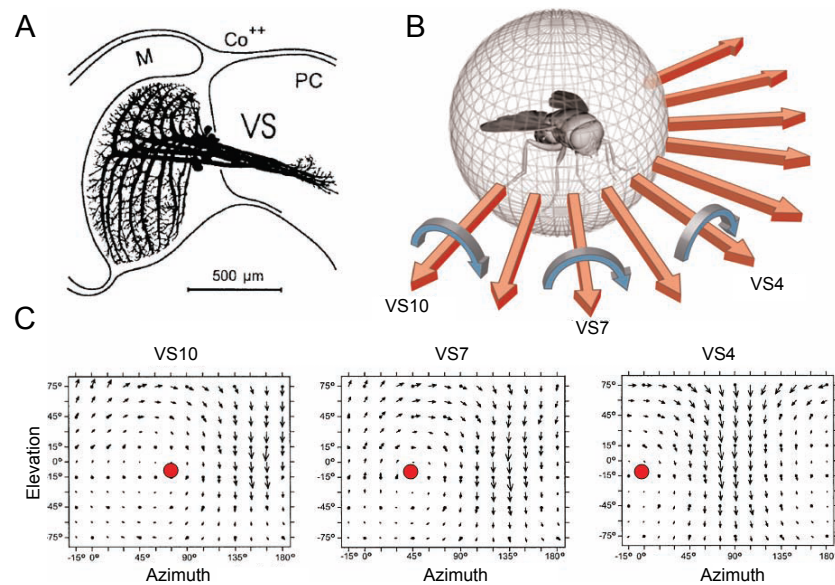


**Figure 1.11: The Tangential Cells Act as Matched Filters.** (A) Structure of the VS cells obtained from cobalt staining (M - Medulla, PC - Protocerebrum). (B) Schematic fly with various rotation axes. (C) Spatial receptive fields of VS10, VS7 and VS4. The rotation axes of the best fitting rotational flow fields are indicated by red dots. Figure taken from (Borst and Haag, 2007). (A) modified from (Hengstenberg et al., 1982), (B) modified from (Zbikowski, 2005), and (C) taken from (Krapp et al., 1998).)

For global stimulation, rotations about various body axes within a rectangular room were presented to fixed flies, while the activity of VS cells was recorded. It could be shown that the rotation axis predicted from the receptive field indeed matches the preferred axis for global stimulation.

The mechanisms underlying the complex receptive fields of the tangential cells have been intensively studied for the VS cells (Haag et al., 2004; Farrow et al., 2005; Elyada et al., 2009; Borst and Weber, 2011). Photo-ablations of single VS cells narrowed the tuning width of neighboring cells (Farrow et al., 2005), demonstrating that the broadening of the receptive fields relies on the electrical synapses between these neurons. Modeling and experimental studies revealed that the specific connectivity of the VS cells allows for a robust representation of the fly's rotation axis (Cuntz et al., 2007; Weber et al., 2008; Elyada et al., 2009).

Due to the curly structure of their receptive fields, the VS cells are not only sensitive to vertical downward-motion, but also exhibit regions where they respond to horizontal or upward motion. The connectivity of the VS cells probably underlies these complex receptive fields. This hypothesis was tested in a simulation study based on a network model

including all known tangential cells and their connectivity (Borst and Weber, 2011). Figure 1.12A depicts the receptive field of a simulated VS10 cell strongly resembling a rotational flow field. To test to what extent the receptive field depends on the connectivity of VS10, it was re-calculated after disconnecting all tangential cells in the stimulated network. When disconnected, VS10 is only sensitive to downward motion within a small stripe (Figure 1.12A). The remaining vertical motion sensitivity arises from pre-synaptic, vertically tuned motion detectors integrated by the dendrite. To test whether dCH, which is electrically coupled to VS10, is responsible for the horizontal sensitivity, it was voltage-clamped. The resulting receptive field of VS10 indeed shows a reduced horizontal sensitivity (Figure 1.12C). By voltage clamping VS1 in the network stimulation, it could be demonstrated that the inhibition of VS10 by VS1 underlies VS10's upward sensitivity. The resulting receptive field still shows sensitivity to horizontal motion, however all upward oriented components vanished (Figure 1.12D).

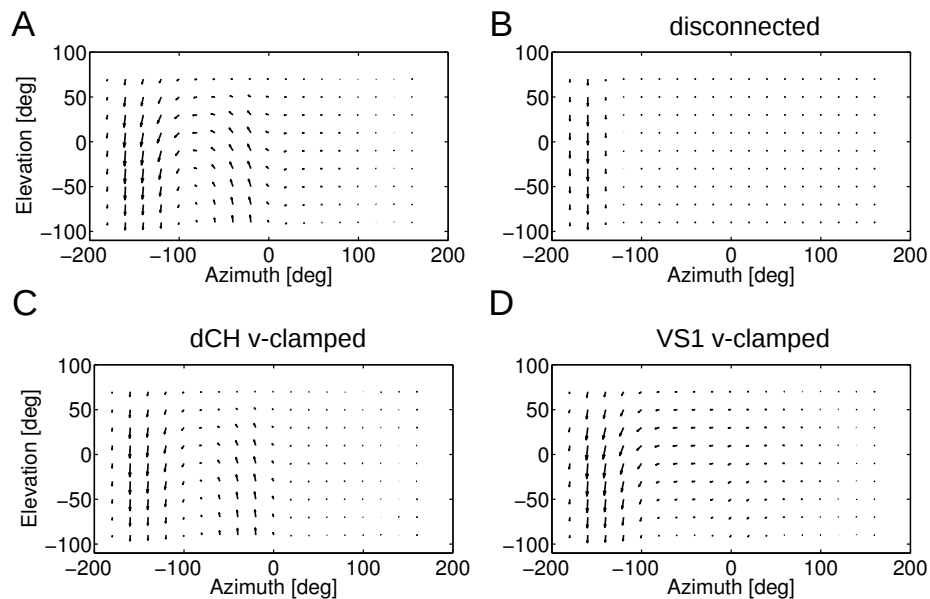


**Figure 1.12: The Receptive Field Structure of VS10 Arises from its Connectivity.** (A) Receptive field of a simulated VS10 cell. In the simulation, the receptive field was determined by the same method as applied in (Wertz et al., 2009). (B) Receptive field of VS10 with all connections between the cells removed. (C) Receptive field of VS10 after voltage-clamping dCH. (D) Receptive field of VS10 after voltage-clamping VS1. Figure modified from Borst and Weber (2011).

### 1.2.7 Processing of Dynamic Motion Stimuli by H1

The spatial receptive fields describe the preferred optic-flow patterns of the lobula plate tangential cells. However, they completely neglect any dynamic properties of the tangential cells. Moreover, they provide no information on how the processing by the tangential cells is affected when changing properties of the stimulus. Such issues have been addressed in experiments with the heterolateral, spiking neuron H1 (Haag and Borst, 1997; Borst, 2003; Fairhall et al., 2001; Brenner et al., 2000; Borst et al., 2005; Safran et al., 2007). In these studies, H1 was stimulated by a global grating moving horizontally according to a Gaussian-noise velocity profile. The presented velocity profiles were typically generated by low-pass filtering a white-noise time series (specifying for each time point the velocity value). These studies then tested how the stimulus processing by H1 varies, when changing the statistics of the velocity profile. To this end, LN-models transforming the velocity to the recorded firing rate were fitted. Changes in the statistics have strong effects on both the stimulus filter of H1, describing its dynamics and on the nonlinearity mapping the filtered stimulus on the firing rate (Safran et al., 2007; Borst, 2003; Borst et al., 2005; Brenner et al., 2000; Fairhall et al., 2001).

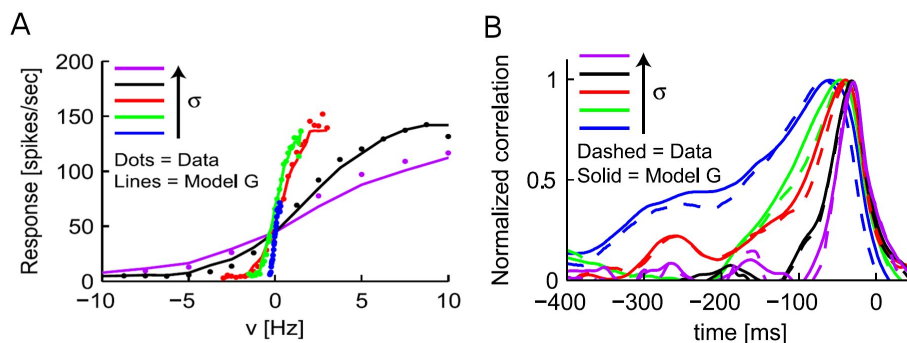


**Figure 1.13: The LN-model of H1.** (A) Increasing the standard deviation  $\sigma$  of the presented velocity profile reduces the steepness of the nonlinearity. The measured data is depicted by the dots. The solid lines show predictions by an array of Reichardt detectors. (B) The width of the stimulus filter decreases with increasing  $\sigma$ . The solid lines depict the predicted filters, the dashed lines show the filters measured for the data. Figure modified from Safran et al. (2007).

As demonstrated in Brenner et al. (2000); Fairhall et al. (2001), when increasing the standard deviation of the velocity waveform, the steepness of the nonlinearity (i.e., the gain of H1) is reduced. Hence, although the range of presented velocity amplitudes is increased, the range of elicited firing rates is still unchanged. This phenomenon is demonstrated

in Figure 1.13A showing the nonlinearities of H1 for five different velocity profiles with increasing standard deviation. This finding suggests the presence of a gain control mechanism which matches the dynamic range of the neural response to the stimulus, thereby maximizing information transmission (Brenner et al., 2000).

The mechanism underlying the observed gain control mechanism was studied in (Borst et al., 2005; Safran et al., 2007). The changes in the gain could be attributed to the intrinsic nonlinearity of the local motion detectors integrated on H1's dendrite. The local motion processing was modeled by Reichardt detectors, an algorithmic model for motion detection presented in more detail in the following section.

Changes in the standard deviation of the velocity waveform do not only effect the nonlinearity in LN-model, but also the stimulus filter. This is illustrated in Figure 1.13B. With increasing standard deviation of the presented velocity, the width of the stimulus filter is reduced. This finding could be also accounted for by the Reichardt detector.

## 1.3 The Reichardt Detector

### 1.3.1 The Structure of the Reichardt Detector

The Reichardt detector estimates motion by correlating the luminance signals at two spatially separated locations, why it is also referred to as correlation-type motion detector (Reichardt, 1961). The basic working principle of the Reichardt detector is illustrated in Figure 1.14. An object passes two input channels sampling brightness changes at two neighboring, but spatially distinct locations. Since the object is moving from left to right, it arrives first at the left input channel, inducing a change in its activity (Figure 1.14A). After some time interval  $\Delta t$  the object activates the second input channel (Figure 1.14B). The time interval depends on the object velocity and the distance between the input channels, i.e. the sampling base of the motion detector. To account for this time interval, the left input signal is delayed by a low-pass filter. The signal of the left channel and the non-delayed input signal of the right channel then arrive at the multiplication state. If the delay induced by the low-pass filter ideally matches the time interval  $\Delta t$ , the multiplication yields the maximal response.

The motion detector depicted in Figure 1.14 is sensitive to left-to-right motion corresponding to its preferred direction. To inhibit its activity by motion in the opposite direction, the activity of a second, mirrored detector with right-to-left motion as preferred direction is subtracted. The resulting motion detector is excited by left-to-right motion (preferred direction) and inhibited by right-to-left motion (null direction) and represents the Reichardt

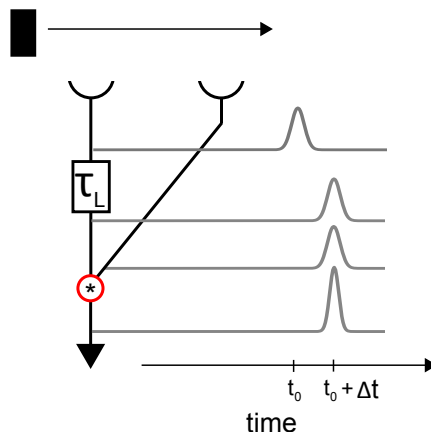


**Figure 1.14: Working Principle of the Reichardt Detector.** An object passes two input channels or photoreceptors. Since it moves from left to right, it first activates the left input channel at time point  $t_0$ . The upper gray curve illustrates the resulting input signal at the left input channel. This signal is then delayed by a low-pass filter with time-constant  $\tau_L$ , as illustrated by the second gray curve. After some time interval  $\Delta t$  the object arrives at the second input channel. If the left input signal is ideally delayed by  $\Delta t$  s, the input signals of both photoreceptors arrive at the same time point at the multiplication stage (asterisk). The right input signal is illustrated by the third gray curve. Multiplication of both signals then yields the maximal response indicated by the gray curve at the bottom.

detector in its most parsimonious form shown in Figure 1.15 A.

A more advanced version of the Reichardt detector is shown in Figure 1.15B: In this model, an additional high-pass filter is inserted in the cross-arms of the detector. With the high-pass filters the Reichardt detector better reproduces responses to a velocity pulse induced by a abrupt displacement of the presented visual pattern (Egelhaaf and Borst, 1989; Borst et al., 2003). Moreover, changes in the high-pass filter constant have been postulated to account for adaptive changes of the detector's impulse response (Borst et al., 2003).

### 1.3.2 Evidence for the Reichardt Detector

The response properties of the Reichardt detector have been mainly studied for sine gratings. Due to the simplicity of this stimulus, the response elicited by a moving sine grating can be analytically derived. All fundamental characteristics of the Reichardt detector could be experimentally verified (Borst and Egelhaaf, 1990; Egelhaaf et al., 1989; Borst et al., 2010). A first characteristic of the Reichardt detector is that it does not behave as an ideal speedometer, where the response depends linearly on the velocity. Instead, the response first increases with increasing velocity, before reaching an optimum and then starts decreasing. Second, the velocity tuning depends on the wavelength of the sine grating: the

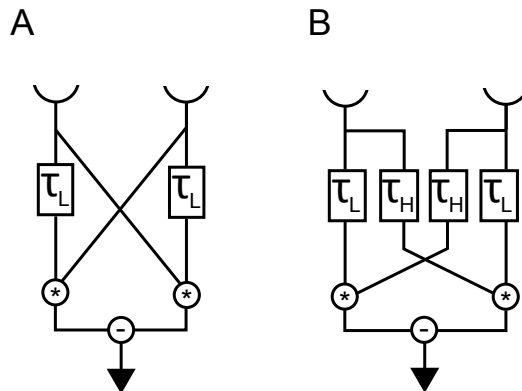


**Figure 1.15: The Reichardt Detector.** (A) Minimal Reichardt detector. In each subunit the input signal is delayed by the first-order low-pass filter with time-constant  $\tau_L$  and multiplied with the unfiltered signal from the neighboring photoreceptor. (B) Reichardt detector with an additional high-pass filter inserted in the cross-arms of the detector. The time-constant of the first-order high-pass filters is denoted by  $\tau_H$ .

larger the wavelength, the higher the velocity at which the response maximum is reached. Since the response optimum increases linearly with the wavelength, it is determined by the ratio of the wavelength and the velocity, referred to as temporal frequency. As function of the temporal frequency, the velocity tuning curves peak at same frequency, independent of the pattern wavelength.

These predictions by the Reichardt detector could be verified in electrophysiological experiments in blowflies (Haag et al., 2004) and fruit flies (Joesch et al., 2008; Schnell et al., 2010). In dependence of the temporal frequency, the velocity tuning curves of the lobula plate tangential cells indeed coincide for different wavelengths, reaching their maximum at about 1 Hz.

A further characteristic feature of the Reichardt detector is that its response oscillates at the temporal frequency of the presented stimulus. Only when summing the responses of a whole array of Reichardt detectors, the oscillations induced by single detectors are smoothed out through spatial integration. As predicted, the membrane potential of the lobula plate tangential cells exhibited oscillations, when presenting a sufficiently small stimulus such that spatial integration cannot take place (Egelhaaf et al., 1989). Similarly, it could be demonstrated using Calcium imaging that, within small dendritic branches, the measured signals are strongly modulated (Single and Borst, 1998).

### 1.3.3 Biophysical Implementation of the Reichardt Detector

#### The Subtraction Stage

How the different algorithmical elements of the Reichardt detector are implemented within the circuitry of the visual system is still largely unclear. So far, there exists only strong evidence for the physiological implementation of the subtraction in the Reichardt detector. The motion-sensitivity of the tangential cells arises from the integration of the outputs of pre-synaptic motion-sensitive neurons, probably T4 and T5 cells. There is strong evidence that the pre-synaptic neurons integrated by a tangential cell have opposite preferred directions (Brotz and Borst, 1996; Single et al., 1997). In analogy to the Reichardt detector, these inputs represent the two mirror-symmetrical subunits of the detector which are physiologically subtracted via excitatory and inhibitory synapses.

Assuming that the dendrite of a tangential cell integrates the synaptic outputs of a whole array of Reichardt detectors allows for the following predictions: Injecting a positive current into the dendrite should lower the driving force of the excitatory synapses. Consequently, the response amplitude to motion in the preferred should be reduced. Similarly, an injection of negative current will reduce the inhibitory driving force yielding a reduced response to motion in the null direction. Both predictions could be verified in blow flies (Borst et al., 1995, 2010) and *Drosophila* (Joesch et al., 2008).

Besides the subtraction in the Reichardt model, this push-pull input organization also implements an automatic gain control mechanism compensating for the size of a sine grating: Increasing the size of the pattern, an increasing number of pre-synaptic motion detectors is activated leading to a reduction of the cell's input resistance. Consequently, the impact of an inflowing current onto the cell's membrane potential is reduced. Therefore, the response of a tangential cell saturates with increasing patterns size (Borst et al., 1995; Single et al., 1997).

#### Separate Off/On-Pathways

A recent study analyzed the internal structure of the fly's motion detector (Eichner et al., 2011): Based on the observation that the brightness signals from the photoreceptors are split into its on and off-parts (Joesch et al., 2010), the authors compared two alternative models. The first model, the four-quadrant detector, consists of four parallel detectors each processing one of the four possible combinations of on- and off-signals (see Figure 1.16B). In the on-detector, the two on-components of the brightness signal from the two photoreceptors of the detector are correlated to compute motion. Analogously, off-components are

correlated in the off-detector. The correlation of an on- or off-component from the first photoreceptor and an off- or on-signal from the second photoreceptor takes place in the on-off or off-on detector. The second model comprises only two parallel detectors correlating brightness components of the same sign, whereas signals of different polarity do not interact (see Figure 1.16C).

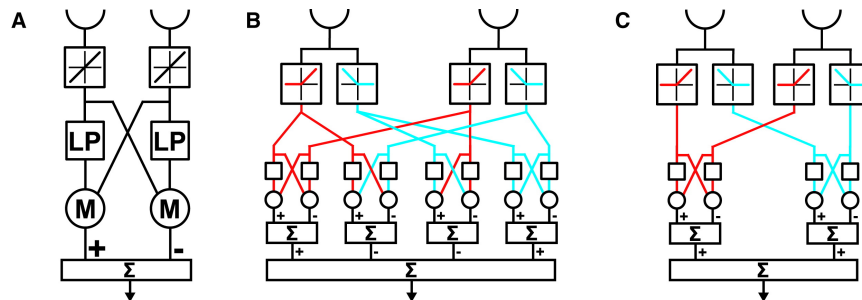


**Figure 1.16: Different Implementations of the Reichardt Detector.** (A) Original Reichardt detector (B) The four-quadrant detector. This detector is mathematically equivalent to the original Reichardt detector in (A). The brightness signals from the photoreceptors are split into its on- and off-components through a half-wave rectification. The four possible combinations of on- and off-signals are then processed in four different detectors. (C) The two-quadrant detector. In this detector only input components of the same sign are correlated, whereas on- and off-signal components do not interact. Figure taken from Eichner et al. (2011).

To test which of the two proposed detector models best reproduces the structure of the fly motion detector, apparent motion stimuli were presented. By presenting two short brightness pulses which were displayed in sequence at two neighboring locations, it was possible to exclude the four-quadrant detector. Hence, the fly motion detector is in agreement with a two-quadrant detector, where on- and off-signals are processed in separate pathways that do not interact.

## 1.4 Thesis Projects

This thesis describes in detail the methods and results of three projects discussed as different sections in the third chapter (Results 3):

1. Spatio-Temporal Response Properties of the Tangential Cells
2. Self-Motion Encoding by the Tangential Cells
3. The Functional Role of an Inter-Hemispheric Projection

Parts of the thesis are based on previous publications. The findings of the first section of the Results chapter were published in (Weber et al., 2010). The third section of the Results follows a still unpublished manuscript. Parts of the first (Introduction 1) and the second chapter (Materials and Methods 2) were previously published in (Borst and Weber, 2011). Since my main contribution to the latter paper were parts of the applied methods, its major findings were not summarized as an own section in the Results.

# Chapter 2

## Materials and Methods

### 2.1 Visual Stimulation

The visual stimuli used for the experiments presented in Sections 3.1 and 3.3 were displayed on a custom-built light-emitting (LED) arena (see Figure 2.1A). For presentation of stimuli discussed in Section 3.2, a stimulus device consisting of three LCD-monitors was used (see Figure 2.1B).

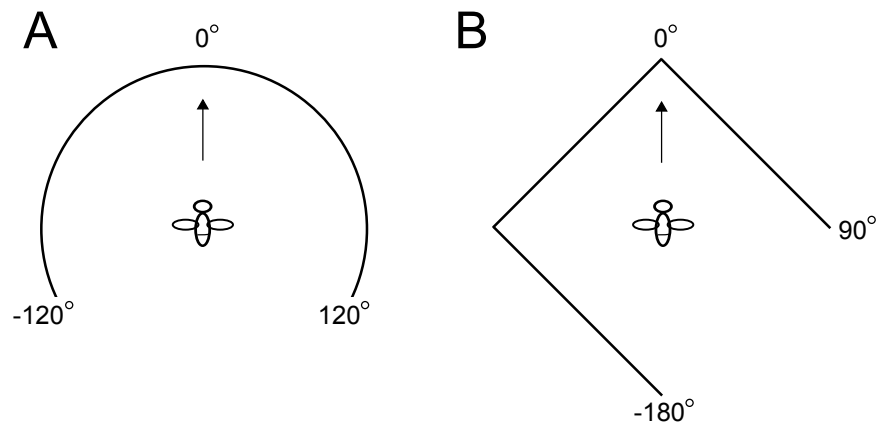


**Figure 2.1: Schematic top view of the stimulus devices.** (A) LED-arena. The arena is cylinder-shaped. The fly was positioned in the center of the cylinder facing the center point ( $0^\circ, 0^\circ$ ). Along the azimuth, the arena ranges from  $-120^\circ$  to  $120^\circ$ . The arrow indicates the viewing direction of the fly. (B) LCD-monitor setup. Three 120Hz LCD-monitors were positioned on three edges of a square. The fly faced the node connecting the edges of the middle and right screen. The stimulated visual space ranged from  $-180^\circ$  to  $90^\circ$  along the azimuth. Any distortions along the horizontal or vertical due to the inhomogeneous distances of the fly to the monitor surfaces were accounted for by the stimulus generation.

### LED-Arena

The LED-arena is cylinder-shaped and allows for 16 different intensity values at a refresh rate of 200 Hz or 250 Hz. The arena is assembled from  $30 \times 8$  TA08-81GWA dot matrix displays (Kingbright, Walnut, CA), each harboring  $8 \times 8$  individual green (568-nm) LEDs. The arena covers  $242^\circ$  and  $96^\circ$  of the horizontal and vertical visual field, with an angular resolution of at least  $1^\circ$ . Since the arena is not curved along the elevation direction, the presented stimuli were distorted along the vertical to mimic their shape on a sphere. In the graphical representations of the receptive fields, the left border of the arena corresponds to an azimuth of  $-121^\circ$ , whereas  $-48^\circ$  denotes the lower border, such that the point  $(0^\circ, 0^\circ)$  lies in the middle of the arena surface. Flies were placed in the center of the cylinder, with their eyes facing the center point  $(0^\circ, 0^\circ)$ . All stimuli presented on the LED-arena were programmed in MATLAB ([www.mathworks.com](http://www.mathworks.com)).

### LCD-Monitor Setup

The LCD-monitor setup is assembled from three LCD-monitors (SyncMaster 2233RZ, Samsung) which were placed along three edges of a square. The fly faced the node connecting the middle and right monitor (see Figure 2.1B). The stimulated visual space ranged from  $-180^\circ$  to  $90^\circ$  along the azimuth. Along the vertical, the stimulated visual space had a minimal extension of  $58^\circ$  and a maximal extension of  $76^\circ$ . Stimuli were presented at 120 Hz. All three monitors were synchronized by a graphics card (3D Vision Surround, Nvidia). To record the exact frame rate a photo-diode was placed on a small square on one of the monitors, whose color switched for each frame between light gray and black. The timing of each frame was derived from the recorded oscillating signal. All presented stimuli were programmed using the open-source game engine panda3D ([www.panda3d.org](http://www.panda3d.org)).

## 2.2 Preparation and Recording

The experiments were carried out in two different fly species: For the receptive field and self-motion processing studies, presented in Sections 3.1 and 3.2, recordings were performed in *Calliphora vicina*. The fly species *Lucilia sericata* was used for the lateral interaction study discussed in Section 3.3. All experiments were carried out in 3 to 15 days-old male or female flies. In both species the spiking responses of lobula plate tangential cells were recorded. Flies were fixed with wax and their heads were aligned using the pseudo-pupils in the frontal region of both eyes. To introduce an electrode into the brain, the head capsule was opened and fat tissue and air sacks were removed. The neural activity was recorded

extracellularly with a tungsten electrode with an input resistance of  $1 \text{ } \Omega M$ , which was inserted into the lobula plate. For simultaneous recordings of two tangential cells, each neuron was recorded with a single electrode. The recorded signals were then band-pass filtered, amplified, and sampled at 10 kHz. For spike detection, two different approaches were applied: For excellent signal-to-noise ratios ( $> 3$ ), spikes were detected using a simple threshold algorithm. If the signal-to-noise ratio was worse, I first isolated all potential waveforms whose negative peak exceeded a sensitive threshold. To reduce dimensionality, the waveforms were projected by principal component analysis onto the first three eigenvectors. Then, a Gaussian mixture model was fitted to separate waveforms corresponding to spikes from noise induced waveforms (Bishop, 2008).

## 2.3 Self-Motion Induced Optic-Flow

### 2.3.1 Mathematical Description of Optic-Flow

A fly whose eye is modeled as a sphere is flying around in an environment. For simplicity, the sphere is centered at the origin  $\mathbf{0}$  of the Cartesian coordinate system and its radius has length 1.  $\mathbf{Q}_i$  denotes the position of a point somewhere in the surrounding environment. This point is projected onto the point  $\mathbf{d}_i$  on the surface of the sphere with  $\mathbf{d}_i = \mathbf{Q}_i \mu_i$ , where  $\mu_i = 1/||\mathbf{Q}_i||$  denotes the nearness of the fly to the point  $\mathbf{Q}_i$ . The vector  $\mathbf{d}_i$  describes the viewing direction where  $\mathbf{Q}_i$  is located. When the fly moves, the point at position  $\mathbf{Q}_i$  is displaced with respect to the sphere which, in turn, also changes  $\mathbf{d}_i$ , the projection of  $\mathbf{Q}_i$  onto the sphere.

According to Chasles' theorem, a movement of the fly can be unambiguously described by a translation along a vector  $\mathbf{T}$  and a rotation about an axis  $\mathbf{R}$  through the center of the sphere. Moreover, a self-motion of the fly can be simulated through a translation and rotation in the respective opposite direction.

If the sphere translates forward for an infinitesimal time  $\Delta t$ , the environment moves backward in the same direction. The displacement of  $\mathbf{Q}_i$  (with respect to the sphere center) due to the translation is given by

$$\Delta \mathbf{Q}_i = -\mathbf{T} \Delta t$$

Accordingly, if the fly rotates clockwise around  $\mathbf{R}$ , this corresponds to a counter-clockwise rotation of the environment causing the displacement

$$\Delta \mathbf{Q}_i = -(\mathbf{R} \times \mathbf{Q}_i) \Delta t$$

Combining these equations describes the displacement of  $\mathbf{Q}_i$  due to an arbitrary motion of the fly. However, a displacement of  $\mathbf{Q}_i$  during  $\Delta t$  changes the projection of  $\mathbf{Q}_i$  onto the surface of the eye by some  $\Delta \mathbf{d}_i$ . For a motion in the radial direction, i.e. in the direction of  $\mathbf{Q}_i$ , the projection point of  $\mathbf{Q}_i$  does not change, i.e.  $\Delta \mathbf{d}_i = 0$ . Therefore  $(\mathbf{T} \cdot \mathbf{Q}_i)\mathbf{Q}_i$  (the projection of  $\mathbf{T}$  onto  $\mathbf{d}_i$ ) has to be subtracted from the translation yielding the expression:

$$\Delta \mathbf{d}_i = -\mu_i(\mathbf{T} - (\mathbf{T} \cdot \mathbf{d}_i) \mathbf{d}_i + \mathbf{R} \times \mathbf{d}_i)\Delta t$$

where I used  $\mathbf{d}_i = \mathbf{Q}_i/\mu_i$ . If  $\Delta t \rightarrow 0$ , the last equation becomes

$$\mathbf{p}_i = \frac{d}{dt}\mathbf{d}_i = \lim_{\Delta t \rightarrow 0} \frac{\Delta \mathbf{d}_i}{\Delta t} = \underbrace{-\mu_i(\mathbf{T} - (\mathbf{T} \cdot \mathbf{d}_i)\mathbf{d}_i)}_{\text{translation}} - \underbrace{\mathbf{R} \times \mathbf{d}_i}_{\text{rotation}} \quad (2.1)$$

$\mathbf{p}_i$  describes the optic-flow induced by a rotation about  $\mathbf{R}$  and a translation along  $\mathbf{T}$ . Note that the operation  $\mathbf{T} - (\mathbf{T} \cdot \mathbf{d}_i)\mathbf{d}_i$  orthogonalized  $\mathbf{T}$  with respect to  $\mathbf{d}_i$ . Since the cross-product  $\mathbf{R} \times \mathbf{d}_i$  is also orthogonal to  $\mathbf{d}_i$ , the optic-flow  $\mathbf{p}_i$  is orthogonal to  $\mathbf{d}_i$ . Therefore, although  $\mathbf{p}_i$  is a three-dimensional vector, it can be unambiguously defined by only two dimensions tangent to  $\mathbf{d}_i$ . Hence, through multiplication by a  $2 \times 3$  matrix  $\mathbf{B}$ ,  $\mathbf{p}_i$  can be projected onto a two-dimensional vector. A convenient choice for  $\mathbf{B}$  is the matrix

$$\mathbf{B} = \begin{bmatrix} -\sin \theta & \cos \phi & 0 \\ -\sin \theta \cos \theta & -\sin \theta \sin \phi & \cos \theta \end{bmatrix}.$$

The matrix  $\mathbf{B}$  is orthonormal, i.e.  $\mathbf{B}\mathbf{B}^\top = \mathbf{1}$ . Its rows can be interpreted as a local coordinate system positioned at  $(\phi, \theta)$  on the sphere with its axes pointing in the direction of the longitude and latitude. Instead by the sub index  $i$ , we refer in the following to a location on the unit sphere through the azimuth and elevation angle  $\phi$  and  $\theta$ . (Here, I follow the convention that the north pole of the sphere corresponds to  $\pi/2$ .) The values for the azimuth and elevation angle lie in the range  $-\pi \leq \phi \leq \pi$  and  $-\pi/2 \leq \theta \leq \pi/2$ . The optic-flow at position  $(\phi, \theta)$  through a rotation and translation about  $\mathbf{R}$  and along  $\mathbf{T}$  can then be expressed as

$$\mathbf{F}(\mathbf{R}, \mathbf{T}, \phi, \theta) = \mathbf{B} \mathbf{p}(\mathbf{R}, \mathbf{T}, \phi, \theta).$$

The flow-field new expressed by the two-dimensional vector  $\mathbf{F}(\phi, \theta)$  can be decomposed in its translational and rotational component, i.e.  $\mathbf{F}(\mathbf{R}, \mathbf{T}, \phi, \theta) = \mathbf{F}(\mathbf{R}, \mathbf{0}, \phi, \theta) + \mathbf{F}(\mathbf{0}, \mathbf{T}, \phi, \theta)$  with

$$\mathbf{F}(\mathbf{R}, \mathbf{0}, \theta, \phi) = v_{rot} \begin{pmatrix} \cos \theta \sin \theta_{rot} - \sin \phi \sin \theta \cos \theta_{rot} \sin \phi_{rot} - \cos \phi \sin \theta \cos \theta_{rot} \cos \phi_{rot} \\ \cos \theta_{rot} (\sin \phi \cos \phi_{rot} - \cos \phi \sin \phi_{rot}) \end{pmatrix}$$

and

$$\mathbf{F}(\mathbf{0}, \mathbf{T}, \theta, \phi) = \mu v_{tra} \begin{pmatrix} \cos \theta_{tra} (\sin \phi \cos \phi_{tra} - \cos \phi \sin \phi_{tra}) \\ -\cos \theta \sin \theta_{tra} + \sin \phi \sin \theta \cos \theta_{tra} \sin \phi_{tra} + \cos \phi \sin \theta \cos \theta_{tra} \cos \phi_{tra} \end{pmatrix}$$

Here I expressed  $\mathbf{R}$  and  $\mathbf{T}$  in spherical coordinates, i.e.

$$\mathbf{R} = v_{rot} [\cos \phi_{rot} \cos \theta_{rot}, \sin \phi_{rot} \cos \theta_{rot}, \sin \theta_{rot}]^T$$

and

$$\mathbf{T} = v_{tra} [\cos \phi_{tra} \cos \theta_{tra}, \sin \phi_{tra} \cos \theta_{tra}, \sin \theta_{tra}]^T.$$

As an optic-flow pattern, the receptive field of a motion-sensitive neuron is described by a vector field attributing to each point  $(\phi, \theta)$  on the unit sphere a vector. Intuitively, this vector, denoted by  $\mathbf{H}(\phi, \theta)$ , describes the neuron's sensitivity to horizontal and vertical motion at location  $(\phi, \theta)$ . The receptive field  $\mathbf{H}(\phi, \theta)$  can be decomposed into two scalar fields,  $H_{az}(\phi, \theta)$  and  $H_{el}(\phi, \theta)$ , specifying the horizontal and vertical component of the vector  $\mathbf{H}(\phi, \theta)$ .

### 2.3.2 Comparison of Rotation and Translation

Rotations and translations are originally defined in different units. The rotation velocity is typically specified by the number of rotations per second or the angular width rotated in a second. Contrarily, the translation velocity is defined in distance per second. To make rotations and translations comparable, the translation axes  $\mathbf{T}(t)$  were normalized by the distance of a particular receptive field on the unit sphere (modeling the fly's eye) to the surrounding environment. The receptive field is given by the matrices  $H_{az}(\phi, \theta)$  and  $H_{el}(\phi, \theta)$  describing the preferred motion vector at location  $(\phi, \theta)$ . The motion sensitivity at location  $(\phi, \theta)$  is defined by

$$S(\phi, \theta) = \|\mathbf{H}(\phi, \theta)\| = (H_{az}(\phi, \theta)^2 + H_{el}(\phi, \theta)^2)^{-1/2} \quad (2.2)$$

The distance of a particular receptive field is defined as the scalar product of the distances between the fly and the surrounding environment,  $D(\phi, \theta, t)$ , and the receptive field sensitivity,

$$D_H(t) = \int_{\phi} \int_{\theta} D(\phi_i, \theta_j, t) S(\phi_i, \theta_j) \cos \theta d\phi d\theta. \quad (2.3)$$

Dividing  $\mathbf{T}(t)$  with units  $m/s$  by  $D_H(t)$  with units  $m$  gives a normalized translation vector  $\mathbf{T}_n(t)$  with units  $1/s$ . Consequently,  $\mathbf{T}_n(t)$  and  $\mathbf{R}(t)$  can be directly compared.

### 2.3.3 Optic-Flow Norm

To guarantee that the strength translational and rotational optic-flow perceived by a specific receptive field is comparable, I defined an optic-flow norm. The motion sensitivity of the receptive field at location  $(\phi, \theta)$  is again defined by  $S(\phi, \theta)$ . The optic-flow pattern induced by a translation along  $\mathbf{T}(t)$  and rotation about  $\mathbf{R}(t)$  is again denoted by  $\mathbf{p}(\mathbf{T}, \mathbf{R}, \phi, \theta, t)$  (see Equation 2.1). The norm of the optic-flow at time  $t$  is then defined by

$$\int_{\phi} \int_{\theta} S(\phi, \theta) \|\mathbf{p}(\mathbf{T}(t), \mathbf{R}(t), \phi, \theta, t)\| \cos \theta d\phi d\theta. \quad (2.4)$$

## 2.4 Visual Stimuli

### 2.4.1 Brownian Motion Stimulus

The Brownian motion stimulus consists of  $n$  dots moving randomly across the stimulated visual space. Each dot is represented by a 2D Gaussian with a standard deviation of  $1.5^\circ$ . The luminance intensities ranged from the second lowest intensity value for regions not covered by a Gaussian dot to the highest intensity for the center of a Gaussian. The motion of each point follows the formula for Brownian motion. The azimuth and elevation location of point  $k$  at time  $t_{i+1}$  are denoted by  $\phi_k(t_{i+1})$  and  $\theta_k(t_{i+1})$  and are calculated from the previous time point  $t_i$  by

$$\phi_k(t_{i+1}) = \phi_k(t_i) + \sigma N(0, \sigma) \sqrt{dt}, \quad (2.5)$$

and

$$\theta_k(t_{i+1}) = \theta_k(t_i) + \sigma N(0, \sigma) \sqrt{dt}, \quad (2.6)$$

where  $N(0, \sigma)$  denotes a mean zero Gaussian with standard deviation  $\sigma$ . The time step  $dt = 5ms$  is determined by the refresh rate (200 Hz) of the LED-arena. The time series of azimuth and elevation positions of point  $k$ ,  $\phi_k$  and  $\theta_k$ , were then fed through a 50-th order low-pass FIR digital filter with a cutoff frequency,  $f_c$  of 20 Hz. Thus, the stimulus is controlled by three parameters: the number of points,  $n$ , the standard deviation of the Gaussian,  $\sigma$ , and the cut-off frequency,  $f_c$ . We compared two stimulus conditions: A sparse motion stimulus with 6 dots and a dense motion stimulus where 120 dots were presented. The stimuli were presented to the fly as two dimensional luminance frames displayed at a refresh rate of 200 Hz. In its original format, each stimulus is specified at position  $(\phi_i, \theta_j)$  and time point  $t_k$  by the luminance value  $S(\phi_i, \theta_j, t_k)$ . Since the lobula plate tangential cells are primarily sensitive to motion and not luminance, we transformed the stimuli from

the luminance to the visual motion space. Parameterizing the luminance value  $S(\phi_i, \theta_j, t_k)$  in terms of velocity, yields two values value  $V_{az}(\phi_i, \theta_j, t_k)$  and  $V_{el}(\phi_i, \theta_j, t_k)$  specifying the horizontal and vertical speed at location  $(\phi_i, \theta_j)$ . To reduce dimensionality, the motion space is discretized to an rectangular  $6 \times 14$  grid. The six elevation angles of grid square centers ranged from  $\theta_1 = -41$  to  $\theta_6 = 41$  deg and were inter-spaced by an angle of  $\Delta\theta = 16.3$  deg. The azimuth angles of the centers ranged from  $\phi_1 = -112^\circ$  to  $\phi_{14} = 112^\circ$  deg, and were thus separated by  $\Delta\phi = 17.3^\circ$ . To parameterize the stimulus, velocity was defined as being proportional to the positional change of a dot within two successive luminance frames. I summed all azimuth and elevation speeds of dots within the grid square given by  $\phi_i - \frac{\Delta\phi}{2} < \phi_i + \frac{\Delta\phi}{2}$  and  $\theta_i - \frac{\Delta\theta}{2} < \theta_i + \frac{\Delta\theta}{2}$  to specify  $V_{az}(\phi_i, \theta_j, t_k)$  and  $V_{el}(\phi_i, \theta_j, t_k)$ . In total I recorded from ten H1, nine Vi, five V1, four V2, and six H2 cells in *Calliphora vicina* during presentation of the Brownian motion stimulus.

### 2.4.2 Local White-Noise Stimulus

For the local white-noise stimulus, a small circular horizontally or vertically oriented sine grating was presented at various positions. The wavelength and diameter of each circular sine was set to  $15^\circ$ . The sine grating moved then horizontally or vertically according to a white-noise velocity profile. The phase of the sine was again generated by a Brownian walk. More precisely, the phase angle  $\psi_{az}$  of a horizontally oriented sine grating at position  $(\phi_i, \theta_j)$  and time point  $t_{i+1}$  is given by

$$\psi_{az}(\phi_i, \theta_j, t_{i+1}) = \psi_{az}(\phi_i, \theta_j, t_i) + N(0, \sigma)\sqrt{dt}, \quad (2.7)$$

where  $N(0, \sigma)$  denotes Gaussian white noise with mean zero and a standard deviation of  $\sigma = 12^\circ/s$ . The time series of phases,  $\psi_{az}$ , was then low-pass filtered using a 50-th order low-pass FIR digital filter with a cutoff frequency,  $f_c$ , of 80 Hz. The phase angles of the vertically oriented sine gratings,  $\psi_{el}$ , were computed analogously.

To estimate temporal filters mapping the velocity of a specific local grating onto the corresponding firing rate, the stimulus is parameterized in the following way: The stimulus velocity is proportional to the phase change of a sine grating within two successive luminance frames. The horizontal speed value  $V_{az}(\phi_i, \theta_j, t_k)$  is only non-zero, if, at time point  $t_k$ , a horizontally oriented sine-grating is presented at position  $(\phi_i, \theta_j)$ . The corresponding velocity value is then given by  $V_{az}(\phi_i, \theta_j, t_k) = (\psi_{az}(\phi_i, \theta_j, t_k) - \psi_{az}(\phi_i, \theta_j, t_{k-1}))/dt$ .  $V_{el}(\phi_i, \theta_j, t_k)$  is calculated analogously.

The stimuli were presented on the LED-arena at a refresh rate of 200 Hz. The local sine gratings were presented at all square of a  $6 \times 8$  grid. The six elevation angles of the grid

square centers ranged from  $\theta_1 = -41^\circ$  to  $\theta_6 = 41^\circ$  and were inter-spaced by an angle of  $\Delta\theta = 16.3^\circ$ . The azimuth angles of the centers ranged from  $\phi_1 = -112^\circ$  to  $\phi_8 = 9^\circ$ , and were separated by  $\Delta\phi = 17.3^\circ$ . In total, five H1 and five Vi cells from *Calliphora vicina* were recorded, while presenting the local-white noise stimulus.

### 2.4.3 White-Noise Self-Motion Stimulus

The white-noise self-motion stimulus was generated by randomly moving a virtual fly modeled as small sphere within a rectangular room. The ceiling, floor, and walls of the room can be tapered with arbitrary textures or images. The lower-left corner of the room corresponds to the origin of the chosen Cartesian coordinate system. In all simulations, the lengths of all edges were set to 1 m. At each time the self-motion of the virtual fly is defined by a rotation axis  $\mathbf{R}(t)$  and a translation axis  $\mathbf{T}(t)$  defining the fly's rotation and translation at time point  $t$ . Note that  $\|\mathbf{R}(t)\|$  specifies the rotation velocity given in rotations/second, whereas  $\|\mathbf{T}(t)\|$  describes the translation velocity in m/s.

The x-, y-, and z-components of the rotation and translation axes were specified by three independent Gaussian white-noise profiles with a standard deviation of  $158^\circ/s$  and  $1.4m/s$  which were then fed through a 50-th order low-pass FIR filter with a cutoff frequency of  $\tau = 30$  Hz. The position of the fly at time point  $t_{i+1}$ ,  $\mathbf{P}(t_{i+1})$ , was calculated according to the formula for Brownian motion by

$$\mathbf{P}(t_{i+1}) = \mathbf{P}(t_i) + \mathbf{T}(t_i)\sqrt{dt} + \mathbf{Z}. \quad (2.8)$$

$\mathbf{Z}$  specifies a repulsion term which prevents that the fly collides with the walls of the room. The repulsion for the x-component,  $Z_x(t)$  is given by

$$Z_x(t) = \frac{g}{(L - P_x(t))^n} - \frac{g}{(P_x(t))^n}, \quad (2.9)$$

where  $L$  denotes the length of the room. The first term describes the repulsion from the front wall, the second term corresponds to the repulsion from the back wall. The parameter  $n$  specifies the range of the repulsion. For large  $n$  the repulsion has only a short range. For all presented stimuli I set  $n = 5$ . The parameter  $g$  defines the overall strength of the repulsion and was set to  $1e - 4$ . The repulsion components  $Z_y(t)$  and  $Z_z(t)$  are defined analogously.

The orientation of the fly at time  $t_i$  is specified by the rotation matrix  $\mathbf{M}(t_i)$ . Multiplication of the initial fly's orientation by  $\mathbf{M}$  yields then the actual orientation at time point  $t_i$ . The rotation matrix  $\mathbf{M}(t_{i+1})$  is recursively defined by

$$\mathbf{M}(t_{i+1}) = \mathbf{M}(t_i)\mathbf{C}(\mathbf{R}(t_i)/\|\mathbf{R}(t_i)\|, \theta), \quad (2.10)$$

where  $\mathbf{C}(\mathbf{A}, \alpha)$  denotes the rotation axis for a rotation of the angle  $\alpha$  about the vector  $\mathbf{A}$ . The angle  $\theta$  is given by  $\|\mathbf{R}(t_i)\|2\pi dt$  with units  $1/s$ .

Given the position and orientation of the virtual fly at each time point, the surrounding room was projected onto the fly's eye (modeled as sphere). The resulting images were then displayed as movie on the stimulus device. All white-noise self-motion stimuli were displayed on the LCD-monitor setup at a refresh rate of 120 Hz. For the experiments presented in Section 3.2, the rectangular room was tapered with eleven different images shown in Figure 3.9. For each image, we presented a presented three different conditions: (1) Only rotations, (2) only translations, (3) rotations and translations, where the rotational and translational profile from the two previous conditions were summed. Each condition was presented for 15 s and repeated as often as possible. In total, I recorded two H1, two Vi, and two V2 cells (with their dendrites located in the left lobula plate) in *Calliphora vicina* while presenting this stimulus.

#### 2.4.4 Random Rotation Stimulus

For the double recordings of the tangential cells Vi and H1 presented in Section 3.3, a simplified version of the self-motion stimulus was developed: First, only rotations were presented, and, second, the stimulus was further simplified by replacing the rectangular room by a sphere, such that all distances between the fly's eye and the surface of the surrounding sphere are homogeneous.

The virtual fly was placed in the center of a large black sphere painted with a regular grid of white dots and rotated at each time point  $t_i$  about a randomly changing rotation axis  $\mathbf{R}(t_i)$ . The time series of x-, y-, and z-components of the rotation axes were low-pass filtered using a 50th-order low-pass FIR digital filter with a cutoff frequency of 37.5 Hz. The orthogonal coordinate systems was such arranged that Vi's preferred rotation axis aligns with the x-axis, whereas H1's preferred axis is given by a linear combination of the x- and z-axis. The preferred axes of both cells are orthogonal to the y-axis. I compared two stimulus conditions: For weak stimulation the sphere was painted with a  $9 \times 5$  grid of dots, whereas for strong stimulation with a  $30 \times 15$  grid. The dots were represented as two-dimensional Gaussians with as standard deviation of  $1.5^\circ$ . For weak and strong stimulation I compared three conditions: (1, Uncorrelated condition) For training the generalized linear models, I generated two independent random rotation stimuli, and displayed the first stimulus only on the left side of the LED-arena, and the second one only on the right side. Consequently,

the stimuli on the left and right side of visual space are uncorrelated. (2, Correlated condition) For testing the GLMs, I presented the same random rotation stimulus on the left and right side of visual space. (3, Unilateral stimulation) To test H1's impact on Vi, the random rotation stimulus on the right side was replaced by a small sine grating with a wavelength of  $20^\circ$  moving in H1's null direction (front-to-back) at a temporal frequency of 1.5 Hz. The grating ranged from  $-7.5^\circ$  to  $7.5^\circ$  along the elevation and from  $50^\circ$  to  $100^\circ$  deg along the azimuth. Each stimulus condition lasted for 30 s. All conditions were repeatedly presented during one recording. To blank the binocular overlap region in the frontal part of the visual space a homogeneously illuminated mask was positioned such that it spanned the entire elevation of the LED-arena and ranged from  $-30$  to  $30^\circ$  along the azimuth. The luminance intensity of the mask was such adjusted that the mean luminance of all stimuli (integrated over the whole LED-arena) was comparable. The random rotation stimulus was presented, while simultaneously recording from the tangential cells Vi and H1 ( $n=8$ ) in *Lucilia sericata*.

## 2.5 Modeling and Data Analysis

### 2.5.1 Modeling an Array of Reichardt Detectors

The response properties of the fly tangential cells can be well described by assuming that they integrate the synaptic outputs of Reichardt detectors (Borst et al., 1995; Lindemann et al., 2005; Haag et al., 1999). I simulated the responses of the pre-synaptic elementary motion detectors to the presented stimuli using an array of Reichardt-detectors with a sampling base of  $2.5^\circ$ .

A visual stimulus presented on the stimulus device can be described as a temporal series of two-dimensional luminance matrices. Generally, the luminance value presented at time point  $t_k$  at location  $(\phi_i, \theta_j)$  is referred to as  $S(\phi_i, \theta_j, t_k)$ .

In the Reichardt model, the luminance signals at two horizontally or vertically neighboring locations are correlated to compute a motion prediction. For a horizontally tuned motion detector, the luminance signals  $S_{az}(\phi_i, \theta_j)$  and  $S_{az}(\phi_{i+1}, \theta_j)$ , at locations  $(\phi_i, \theta_j)$  and  $(\phi_{i+1}, \theta_j)$ , were fed through a low-pass and high-pass filter and subsequently multiplied,

$$G_{az}^{exc}(\phi_i, \theta_j, t) = (S_{az}(\phi_i, \theta_j, t) * LP(t))(S_{az}(\phi_{i+1}, \theta_j, t) * HP(t)) \quad (2.11)$$

with '\*' denoting the convolution operator.  $LP(t)$  denotes a first-order low-pass filter with time constant  $\tau_{LP}$  (Borst, 2003). The time constant of the first-order high-pass filter  $HP(t)$

is denoted by  $\tau_{HP}$ . A second multiplication is performed in a mirror symmetrical way,

$$G_{az}^{inh}(\phi_i, \theta_j, t) = (S_{az}(\phi_i, \theta_j, t) * HP(t))(S_{az}(\phi_{i+1}, \theta_j, t) * LP(t)) \quad (2.12)$$

The subtraction

$$V_{az}(\phi_i, \theta_j, t) = G_{az}^{exc}(\phi_i, \theta_j, t) - G_{az}^{inh}(\phi_i, \theta_j, t) \quad (2.13)$$

yields an estimate for horizontal motion at location  $(\phi_i, \theta_j)$ . Physiologically, the subtraction in Equation 2.13 is implemented via an excitatory and inhibitory synapse, both projecting onto the tangential cell's dendrite (see Section 1.3.3). The corresponding synaptic conductances are given by  $G_{az}^{exc}(\phi_i, \theta_j, t)$  and  $G_{az}^{inh}(\phi_i, \theta_j, t)$ . To ensure that all synaptic conductances are positive, negative values for  $G_{az}^{exc}(\phi_i, \theta_j, t)$  were interpreted as (positive) inhibitory conductances and vice versa. The vertical motion prediction  $V_{el}(\phi_i, \theta_j, t)$  was computed analogously by correlating the luminance signals  $S_{el}(\phi_i, \theta_j, t)$  and  $S_{el}(\phi_i, \theta_{j+1}, t)$ . For various combinations of the low- and high-pass time-constants, I evaluated the predictive power of LN-models mapping the motion predictions by the Reichardt detector array onto the recorded firing rates. Optimal performance values were reached for a low-pass filter time-constant of 8 ms and a high-pass filter constant of 800 ms. These values lie within the range of time-constants as found in (Lindemann et al., 2005).

## 2.5.2 Estimation of the Dynamic Receptive Field

The LN-model approach was adapted for optic-flow encoding neurons. The linear component of the LN-model of a motion-sensitive neuron can be represented as a time-varying vector field referred to as dynamic receptive field (DRF). To predict the neural response, the velocity profiles  $V_{az}(\phi_i, \theta_j, t)$  and  $V_{el}(\phi_i, \theta_j, t)$  of each location  $(\phi_i, \theta_j)$  are first linearly filtered with the kernels  $H_{az}(\phi_i, \theta_j, t)$  and  $H_{el}(\phi_i, \theta_j, t)$  and then summed. Time was discretized according to the frame rate of the LED-arena. Assuming that the DRF has a finite temporal extent of duration  $Kdt$ , the convolution of the parameterized stimulus with the receptive field can be expressed as

$$\begin{aligned} \hat{r}(t_l) = r_0 + & \sum_{k=1}^K \sum_{i=1}^{n_{az}} \sum_{j=1}^{n_{el}} V_{az}(\phi_i, \theta_j, t_{l-k+1}) H_{az}(\phi_i, \theta_j, t_l) \\ & + \sum_{k=1}^K \sum_{i=1}^{n_{az}} \sum_{j=1}^{n_{el}} V_{el}(\phi_i, \theta_j, t_{l-k+1}) H_{el}(\phi_i, \theta_j, t_l) \end{aligned} \quad (2.14)$$

where  $n_{az}$  and  $n_{el}$  determine the resolution of the discretized visual space along the azimuth and elevation. The scalar parameter  $r_0$  denotes a constant offset. The hat on top of  $r(t_l)$

distinguishes the estimated response,  $\hat{r}(t_l)$ , from the measured response,  $r(t_l)$ . In the following, the notation  $\mathbf{X}_c^k$  refers to a two-dimensional  $n_{az} \times n_{el}$  matrix with  $X_c(\phi_i, \theta_j, t_k)$  as entry in its  $i$ -th row and  $j$ -th column. To find a linear filter optimally mapping the transformed stimulus onto the recorded neural response, I first formulated a constrained linear system of equations. For this purpose, I transformed the  $K$  matrices  $V_{az}^k$  and  $V_{el}^k$  preceding time point  $t_l$  through re-indexing into a vector: I concatenated the columns of the matrices  $\mathbf{V}_{az}^k$  and  $\mathbf{V}_{el}^k$  to two vectors which were then fused to a single stimulus vector  $\mathbf{v}^l$ . Applying the same re-indexing to the kernel matrices  $\mathbf{H}_{az}^k$  and  $\mathbf{H}_{el}^k$  yields a single vector  $\mathbf{h}$  that allows to rewrite equation 2.14 as  $\hat{r}(t_l) = r_0 + (\mathbf{v}^l)^T \mathbf{h}$ . Considering all time points  $t_l$  from  $l = K, \dots, M$  and combining all corresponding estimations for  $\hat{r}(t_l)$  in a single vector  $\hat{\mathbf{r}}$  yields

$$\hat{\mathbf{r}} = \mathbf{V}\mathbf{h} \quad (2.15)$$

where the  $i$ -th row of the matrix  $\mathbf{V}$  equals  $(\mathbf{v}^i)^T$ . Since, without loss of generality, the measured response and the stimulus was centered such that  $1/M \sum_i r_i = 0$  and  $1/M \sum_i V_{ij} = 0$  for each column  $j$ , the parameter  $r_0$  can be omitted. The parameters of the DRF are given by the vector  $\mathbf{h}$  minimizing the following error function,

$$Err(\mathbf{h}) = \frac{1}{2} \|\mathbf{r} - \mathbf{V}\mathbf{h}\|^2 + \frac{\lambda}{2} \mathbf{h}^T \mathbf{h} \quad (2.16)$$

The second term forces the vector  $\mathbf{h}$  to be small and is often called power constraint. The estimate  $\mathbf{h}$  can be written as a linear combination of the eigenvectors of the auto-correlation matrix  $\mathbf{V}^T \mathbf{V}$ . Increasing  $\lambda$  decreases the contribution of poorly sampled stimulus directions to the final estimate of  $\mathbf{h}$ . Thus, if appropriately chosen, this constraint prevents an overfit of the model parameters. Setting the derivative of  $Err$  with respect to  $\mathbf{h}$  to zero and rearranging gives the optimal solution which can be expressed as

$$\mathbf{h} = (\mathbf{V}^T \mathbf{V} + \lambda \mathbf{I})^{-1} \mathbf{V}^T \mathbf{r}, \quad (2.17)$$

where  $\mathbf{I}$  denotes the identity matrix. The vector  $\mathbf{h}$  is known as the regularized least-squares solution of equation 2.16 (Bishop, 2008).

### 2.5.3 Space-Time Separation of the Dynamic Receptive Field

Singular value decomposition was used to separate the DRF given by  $H_{az}(\phi_i, \theta_j, t_k)$  and  $H_{el}(\phi_i, \theta_j, t_k)$  into a spatial and temporal component. First, I constructed a matrix  $\mathbf{F}$  in the following way: The elements of  $H_{az}(\phi_i, \theta_j, t_k)$  and  $H_{el}(\phi_i, \theta_j, t_k)$  describing the  $k$ -th kernel frame were rearranged and appended to form the  $k$ -th column vector of the matrix

**F**. Thus, each column of **F** corresponds to a time point, whereas each row refers to the specific location of an azimuth or elevation weight. Singular value decomposition of the matrix **F** yields pairs of normalized spatial and temporal components, each weighted by a singular value. To decompose the DRF, I set all singular values, except the largest one, to zero. To normalize the resulting space-time separated receptive field, the largest singular value was set to 1.

### 2.5.4 Estimation of the Static Nonlinearity

The shape of the static nonlinearity of an LN-model can be estimated from a calibration plot, where the measured responses  $r_i$  are plotted against the predicted responses  $\hat{r}_i$  (Dayan and Abbott, 2001; Chichilnisky, 2001). The functional shape of the nonlinearity was determined by first sorting the prediction values in ascending order and dividing them into groups containing equal number of points. I then calculated for each group the mean response and mean prediction value. Finally, the actual nonlinearity was estimated through fitting a sigmoidal function to the resulting points. The sigmoidal function has three free parameters  $(s, \mu, \sigma)$  and is given by  $f_{sig}(x) = s / (1 + \exp(\frac{\mu-x}{\sigma}))$ . To compare the nonlinearities for different stimulus conditions the corresponding linear filters were first normalized to have unit variance. The gain  $\alpha$  and selectivity  $\theta$  of a neuron were determined by fitting a half-wave rectifier to the calibration plot:

$$f(x) = \begin{cases} \alpha(x - \theta) & x \geq \theta \\ 0 & x \leq \theta \end{cases}$$

### 2.5.5 Biophysically Extended LN-Model

In the experiments with the Brownian motion stimulus, I found that the gain and selectivity of the fly tangential cells are strongly modulated by the density of presented dots. To account for the gain and selectivity modulation, the LN-model was extended by including explicit biophysical elements.

The resulting biophysical model comprises four stages: First, the luminance stimuli are fed through a two-dimensional array of Reichardt detectors describing the conductances of excitatory and inhibitory synapses of local motion detectors projecting onto the tangential cell. The conductances are then temporally filtered using the filter  $b(t)$  and weighted by the synaptic weight matrices  $\mathbf{W}_{az}$  and  $\mathbf{W}_{el}$  (for horizontally and vertically tuned motion detectors), before being integrated within the tangential cell dendrite. The dendritic integration transforms the conductances to a current which is finally mapped onto the firing

rate through the current-discharge curve  $f$ .

To model the dendritic integration taking place in the dendrite of the tangential cells, the investigated neurons were simplified into a finite cable with the passive dendrite at one end and the spike initiation zone (SIZ) on the opposite end. Dendrite and SIZ are separated by the electrotonic distance  $L$ . The total excitatory and inhibitory conductance (given by the weighted sum of conductances of all excitatory and inhibitory synapses of the motion detectors) integrated by the finite cable are denoted by  $g_{exc}$  and  $g_{inh}$ . Using Equations 2.11 and 2.12, they can be written as

$$g_{exc}(t_k) = \frac{1}{n_w} \sum_{s \in az, el} \sum_i \sum_j (G_s^{exc}(\phi_i, \theta_j, t_k) W_s(\phi_i, \theta_j)) * b(t_k) \quad (2.18)$$

and analogously for  $g_{inh}(t_k)$ .  $W_s(\phi_i, \theta_j)$  specifies the synaptic strength of the horizontally or vertically tuned motion detectors at location  $(\phi_i, \theta_j)$ . The norm of the synaptic weight matrix  $\mathbf{W}_s$ , or total synaptic strength, is defined as

$$n_w = |\mathbf{W}_s| = \left( \sum_{s \in az, el} \sum_i \sum_j W_s(\phi_i, \theta_j)^2 \right)^{1/2}.$$

The normalized filter  $b(t_k)$  was added to account e.g. for delays in the motion processing system. Assuming that the neuron integrates over  $K$  time steps, the convolutions in Equation 2.18 can be expressed as a further discrete sum. Note that the presented stimuli were fed through a Reichardt detector array consisting of rightward and upward tuned Reichardt detectors. If, however, for a particular neuron, the detector at position  $(\phi_i, \theta_j)$  is leftwards or downwards tuned,  $G_s^{inh}(\phi_i, \theta_j, t_k)$  has to be substituted by  $G_s^{exc}(\phi_i, \theta_j, t_k)$  and vice versa. Assuming that the spiking mechanism acts as a voltage clamp (Koch et al., 1995), the current flowing to the SIZ at steady-state is

$$I_{siz} = -g_\infty V_s + 2g_\infty e^{-L} \frac{n_w (g_{exc}(E_{exc} - V_s e^{-L}) + g_{inh}(E_{inh} - V_s e^{-L})) + g_\infty V_s e^{-L}}{n_w (g_{exc} + g_{inh})(1 - e^{-2L}) + g_\infty (1 + e^{-2L})} \quad (2.19)$$

with  $g_\infty$  as input conductance for an infinite cable (Holt and Koch, 1997).  $V_s$  denotes the time-averaged voltage.  $E_{exc}$  and  $E_{inh}$  refer to the excitatory and inhibitory reverse potentials. Since the lobula plate tangential cells exhibit very small passive membrane time-constants (Borst and Haag, 1996), it was assumed that the current flowing in response to a dynamic visual stimulus can be approximated by Equation 2.19 as well. If  $L$  is sufficiently large, Equation 2.19 can be approximated using the following functional expression

$$I_{siz}(t_k) = z + \frac{A(g_{exc}(t_k) - g_{inh}(t_k))}{g_{exc}(t_k) + g_{inh}(t_k) + c} + \frac{Dg_{exc}(t_k)}{g_{exc}(t_k) + g_{inh}(t_k) + c} \quad (2.20)$$

where the parameters  $A$ ,  $c$ ,  $D$  and  $z$  are independent of  $g_{exc}$  or  $g_{inh}$ .

Compared with the linear dynamic receptive field,  $W_s$  corresponds to the spatial component, while  $b(t_k)$  is analogous to the temporal filter. Analogously to the full dynamic receptive field,  $W_s$  and  $b(t_k)$  can be interpreted as the most significant dimensions of the matrices  $P_s(\phi_i, \theta_j, t_k) \approx W_s(\phi_i, \theta_j, t_k)b(t_k)$  with  $s \in \{az, el\}$ . The parameters  $A, c, D$ , and  $z$  can be expressed in terms of physiological entities as:

$$A = 2 \frac{g_\infty e^{-L}}{1 - e^{-2L}} |E_{inh}| \quad (2.21)$$

$$c = \frac{g_\infty (1 + e^{-2L})}{(1 - e^{-2L}) n_w} \quad (2.22)$$

$$D = 2(E_{exc} - |E_{inh}|) \frac{g_\infty e^{-L}}{1 - e^{-2L}} \quad (2.23)$$

$$z = -g_\infty V_s \quad (2.24)$$

Consequently, the parameter combinations used for Figure 6 yield:

$$\frac{A}{c} = 2 \frac{e^{-L} |E_{inh}| n_w}{1 + e^{-2L}} \quad (2.25)$$

$$\frac{D}{A} + 1 = \frac{E_{exc}}{|E_{inh}|} \quad (2.26)$$

The current  $I_{siz}$  is finally mapped by the current-discharge curve  $f$  onto a continuous firing rate, i.e.  $r(t) = f(I_{siz}(t))$ . To optimize  $I_{siz}$ , the the following error function was minimized,

$$Err(A, c, D, z, \mathbf{P}_{az}, \mathbf{P}_{el}) = \frac{1}{2} \sum_{i=1}^N (r_i - I_{siz}(t_i))^2 \quad (2.27)$$

with  $r(t_i) = r_i$  denoting the recorded firing rate at time point  $t_i$ . The error function was optimized using conjugate gradient descent. To minimize  $Err$ , the following procedure was used: In a first run of the applied algorithm, I optimized for  $A, c$ , and  $P_s(\phi_i, \theta_j, t_k)$  without constraints on the rank and length of  $\mathbf{P}_s$ . From the obtained matrices  $\mathbf{P}_s$ , I then extracted an estimate for  $\mathbf{W}_s$  and  $\mathbf{b}$  through singular value decomposition of  $\mathbf{P}_s$ . The values for  $W_s$  and  $\mathbf{b}$  were then used as start vectors for a second optimization where  $\mathbf{W}_s$  and  $\mathbf{b}$  were refined. Given the resulting estimates for  $\mathbf{W}_s$  and  $\mathbf{b}$ , I re-optimized in two further runs  $A$  and  $c$  and finally  $D$  and  $z$ . In the end,  $f$  was estimated by comparing the prediction given by  $I_{siz}$  with the recorded firing rate as described above (see Methods 2.5.4). The biophysical

model was estimated simultaneously for both conditions of the Brownian motion stimulus (see Methods 2.4.1). Due to computational limitations, I used a firing rate bin size of 10 ms for H1 and Vi and of 20 ms for H2, V1 and V2. The predictive power of the estimated model was then evaluated using cross-validation (see Methods 2.5.8). For comparison, I determined the predictive power of a model equivalent to the biophysical model without the dendritic integration stage.

### 2.5.6 Estimation of Self-Motion Filters

An LN-model was applied to predict the firing rate for a given self-motion profile specified by the translation and rotation axes  $\mathbf{R}(t)$  and  $\mathbf{T}(t)$ . In the following the x-, y-, and z-component of  $\mathbf{R}(t)$  are referred to by  $R_x(t)$ ,  $R_y(t)$ , and  $R_z(t)$  and analogously for  $\mathbf{T}(t)$ . To predict the neural firing rate at time  $t_k$ ,  $r(t_k)$ , I filtered the three components of the rotation and translation profile with a linear filter. Assuming that the linear filter has a temporal extent of duration  $Kdt$ , the estimate  $\hat{r}(t_k)$  is given by

$$\begin{aligned} \hat{r}(t_i) = & \sum_{k=1}^K \sum_{s \in x,y,z} R_s(t_{i-k+1}) f_s^R(t_k) \\ & + \sum_{k=1}^K \sum_{s \in x,y,z} T_s(t_{i-k+1}) f_s^T(t_k) \end{aligned} \quad (2.28)$$

where  $f_s^R(t)$  denotes the linear filter for one of the three rotational components and analogously for  $f_s^T(t)$ . To find the optimal self-motion filters, I defined a linear system of equations. To do so, I first appended all filters  $\mathbf{f}_s^R$  and  $\mathbf{f}_s^T$  to a single vector  $\mathbf{f}$ . Similarly, the  $K$  rotation and translation axes were concatenated to a single vector  $\mathbf{w}^k$ . Combining all estimates  $\hat{r}(t_k)$  in a single vector  $\hat{\mathbf{r}}$  then gives

$$\hat{\mathbf{r}} = \mathbf{W}\mathbf{f} \quad (2.29)$$

where the k-th row of the matrix  $\mathbf{W}$  equals  $(\mathbf{w}^k)^T$ . The optimal filter  $\mathbf{f}$  minimizes the error function

$$Err(\mathbf{f}) = \frac{1}{2} \|\mathbf{f} - \mathbf{W}\mathbf{f}\|^2 + \frac{\lambda}{2} \mathbf{f}^T \mathbf{f} \quad (2.30)$$

Analogous to Equation 2.17 the optimal solution can be found by

$$\mathbf{f} = (\mathbf{W}^T \mathbf{W} + \lambda \mathbf{I})^{-1} \mathbf{W}^T \hat{\mathbf{r}}. \quad (2.31)$$

### 2.5.7 Generative Spiking Model

The encoding model used to predict the spike trains of the lobula plate tangential cells comprises two stages: (1) First, the luminance stimuli are fed through a two-dimensional array of Reichardt detectors. The outputs of the Reichardt detector array are projected on the spatial receptive fields of Vi or H1 yielding a one-dimensional signal. (2) Second, this signal is used as input for a generalized linear model (GLM) modeling the tangential cells' spiking.

#### Input Signal Estimation

To reduce the dimensionality of the presented stimulus, I fed all luminance stimuli through a two-dimensional array of Reichardt detectors (see Methods 2.5.1). The estimate of the horizontal or vertical motion at location  $(\phi_i, \theta_j)$  is denoted as  $V_{az}(\phi_i, \theta_j, t)$  and  $V_{el}(\phi_i, \theta_j, t)$ . To estimate the input to a tangential cell, the output of the Reichardt detector array is projected onto the spatial receptive field of the corresponding cell yielding a one-dimensional time signal used as input signal for the GLM. The input signal at time  $t_k$  is denoted by  $x_k$  and is given by

$$x(t_k) = \sum_{i,j} H_{az}(\phi_i, \theta_j) V_{az}(\phi_i, \theta_j, t_k) + H_{el}(\phi_i, \theta_j) V_{el}(\phi_i, \theta_j, t_k),$$

where  $H_{az}(\phi_i, \theta_j)$  and  $H_{el}(\phi_i, \theta_j)$  denote the spatial receptive field of the tangential cell.

#### Generalized Linear Model

A generalized linear model was applied to describe a neuron's spiking activity in dependence of the presented stimuli, their preceding activity, and the response of another neuron (Okatan et al., 2005; Paninski et al., 2007; Pillow et al., 2008). Time was discretized such that each time bin lasts for  $dt = 1$  ms. The response  $r_i$  at time point  $t_i$  can take two possible states:  $r_i = 0$ , i.e. no spike, or  $r_i = 1$ , i.e. at least one spike. Hence, the likelihood for  $t_i$  follows a Bernoulli distribution, i.e.

$$L(r_i|p_i) = p_i^{r_i} (1 - p_i)^{1-r_i}, \quad (2.32)$$

where  $p_i$  describes the probability to observe (at least) one spike at  $t_i$ . The actual number of spikes fired at  $t_i$  follows a Poisson distribution. Thus, the spiking probability  $p_i$  is given by

$$p_i = Poiss(r_i > 0|\lambda_i) = 1 - \exp(-\lambda_i dt). \quad (2.33)$$

The instantaneous firing rate  $\lambda_i$  depends on the input signal  $\mathbf{x}_i$  preceding  $t_i$ , the neuron's response up to time point  $t_i$ , and the spiking history of additional neurons. These dependences are expressed via linear filters,

$$\lambda_i = f(\mathbf{k} \cdot \mathbf{x}_i + \mathbf{h} \cdot \mathbf{r}_{i-1} + \mathbf{c} \cdot \mathbf{s}_{i-1} + \mu), \quad (2.34)$$

where  $\mathbf{k}$  is the stimulus filter (i.e. linear receptive field). The vector  $\mathbf{h}$  denotes the post-spike filter describing the impact of preceding spikes on the firing rate and  $\mathbf{c}$  is the coupling filter quantifying the impact of the second neuron on the firing rate. The parameter  $\mu$  is a constant offset to match the neuron's firing rate. Assuming that  $\mathbf{k}$  comprises  $m$  elements,  $\mathbf{k} \cdot \mathbf{x}_i$  is a short-hand notation for  $\sum_{j=1}^m k_j x_{i-j+1}$ . The vector  $\mathbf{s}$  denotes the spike train of a second neuron. Note that Equation 2.34 can be simply extended to an arbitrary number of additional neurons. I set the invertible function  $f$  to  $f = \exp(\cdot)$ . The likelihood of the entire spike train is the product of independent observations at all time points,

$$L(\mathbf{r}|\mathbf{x}, \theta) = \prod_{i=1}^n p_i^{r_i} (1 - p_i)^{1-r_i} = \prod_{i=1}^n (1 - \exp(-\lambda_i dt))^{r_i} \exp(-\lambda_i dt)^{1-r_i} \quad (2.35)$$

With  $\mathbf{r} = [r_1, \dots, r_n]$  and  $\mathbf{x} = [x_1, \dots, x_n]$ . All hidden variables are summarized by  $\theta$ , i.e.  $\theta = \{\mathbf{k}, \mathbf{h}, \mathbf{c}, \mu\}$ . The log likelihood of the entire spike train is then given by

$$\log L(\mathbf{r}|\mathbf{x}, \theta) = \sum_{i=1}^n r_i \log(1 - \exp(-\lambda_i dt)) - \sum_{i=1}^n (1 - r_i) \lambda_i dt \quad (2.36)$$

The optimal model parameters are found by maximizing the log likelihood with respect to  $\theta$  yielding the maximum posteriori estimate for  $\theta$ . To avoid over-fitting, I added a regularizing term  $p$  penalizing the size of all parameters according to the L1-norm, i.e.

$$p = -\alpha \left( \sum_i |k_i| + \sum_i |h_i| + \sum_i |c_i| \right)$$

(Gerwinn et al., 2010). The parameter  $\alpha$  was chosen by means of cross-validation on the unknown test set. The penalized log likelihood was maximized using a nonlinear gradient-descent algorithm.

## Evaluation

To evaluate the spike train prediction of the GLM estimated for the training data set (uncorrelated condition), we calculated the log-likelihood on the test data set (correlated condition). If  $\log L_{hom}$  denotes the log-likelihood of the spike train under a homogeneous Poisson process, the prediction quality measured in bits/spike is given by

$$\log L_{spike}(\mathbf{r}|\mathbf{x}, \theta) = (\log L(\mathbf{r}|\mathbf{x}, \theta) - \log L_{hom}(\mathbf{r})) / \sum_i r_i.$$

### Bias Correction

The spike trains predicted by a GLM directly estimated from the data underestimates the amount of information carried by the spikes about the stimulus. This is likely due to an underestimate of the amplitude  $A_k$  of the stimulus filter  $\mathbf{k}$ . The input signal  $\mathbf{x}$  to the GLM is only an estimate of the actual unknown input  $\mathbf{y}$  provided by pre-synaptic elements to the modeled neuron. The input  $\mathbf{x}$  can then be expressed as  $\mathbf{x} = \mathbf{y} + (\mathbf{x} - \mathbf{y}) = \mathbf{y} + \eta$ , i.e.  $\mathbf{x}$  equals the actual signal plus added noise. Simulations showed that with increasing noise added to the actual input, the stimulus filter amplitude  $A_k$  is underestimated. To account for this bias on the filter amplitude, I increased  $A_k$  while reducing the constant offset  $\mu$  to match the mean firing rate. To do so, I first varied the amplitude and offset and calculated the likelihood for all resulting models. For each value of  $A_k$  I then determined the value of  $\mu$  which preserved the mean firing rate. Next, two errors were calculated in dependence of  $A_k$  to adjust the filter amplitude: (1) An encoding error,  $Err_{enc}$ , quantifying for a given  $A_k$  the percentage by which the log likelihood deviates from the log likelihood of the unmodified GLM. (2) A decoding error,  $Err_{dcd}$ , quantifying the percentage by which the information carried by the spikes of the GLM for  $A_k$  deviates from the information encoded by the recorded spikes. For  $A_k$ , I chose then the value which minimized the sum of both errors.

For the experiments presented in Section 3.3, the corrected stimulus filter amplitude was estimated separately for Vi and H1 as well as for weak and strong stimulation. For Vi,  $A_k$  was set to 1.15 (weak) and 1.2 (strong). For H1,  $A_k$  was found to be 1.35 (weak) and 1.15 (strong).

### 2.5.8 Evaluation of Firing-Rate Models

To evaluate a neural model which predicts the firing rate of a neuron in response to a given stimulus, a cross-validation approach was performed: I split the data into five equally sized subsets, four of which were assembled to form the training set, whereas the remaining one was used as test set. In total, there were thus four different training sets on each of which I estimated the model and finally evaluated it on the corresponding test set. The average performance of the model on the test sets quantifies the model's ability to predict the correct response. The quality of a filter can be measured by the mean square error between estimated and measured response,  $\sigma_e^2 = \langle \frac{1}{M} \sum_i (\mathbf{r}_i - \hat{r}_i)^2 \rangle$ . (The angular brackets  $\langle \cdot \rangle$  denote averaging over trials.)

A frequently applied measure for the performance of a model estimated using linear

regression is the so-called coefficient of determination,  $r^2$ . Given the response power  $\sigma_r^2 = \langle \frac{1}{M} \sum_i r_i^2 \rangle$ ,  $r^2$  can be calculated by

$$r^2 = 1 - \sigma_e^2 / \sigma_r^2. \quad (2.37)$$

Intuitively, the coefficient of determination is the proportion of variability in a data set that is accounted for by the linear model. It varies between 0 and 1, where 1 describes the case where the predicted and recorded response equal each other.

However, since the response normally includes non-stimulus related noise, a value of 1 for  $r^2$  is quite unrealistic. To account for the noise in the recorded signal, an alternative measure was proposed to evaluate the model performance (Sahani and Linden, 2003): Assuming that the recorded response is additively composed of a stimulus-related signal and non-stimulus related noise, the lowest value  $\sigma_e^2$  can reach is the residual noise component. The latter can be estimated by

$$\sigma_\eta^2 = \frac{n}{n-1} \left[ \left\langle \frac{1}{M} \sum_i r_i^2 \right\rangle - \frac{1}{M} \sum_i \langle r_i \rangle^2 \right], \quad (2.38)$$

where  $n$  is the number of trials. Given the response power  $\sigma_r^2 = \langle \frac{1}{M} \sum_i r_i^2 \rangle$ , the relative success of the linear model is given by

$$\beta = \frac{\sigma_r^2 - \sigma_e^2}{\sigma_r^2 - \sigma_\eta^2}, \quad (2.39)$$

which is 1 when the mean square error  $\sigma_e^2$  equals the signal noise. In case of over-fitting, where the model fits noise,  $\beta$  becomes larger than 1. Generally,  $\beta$  can be interpreted as the percentage of the stimulus-related response power,  $(\sigma_r^2 - \sigma_\eta^2)$ , that can be explained by the given model.

I calculated the predictive power of a given model on the training and on the test sets. The relative success on the training set,  $\beta_{train}$ , gives an upper bound for the predictive power of a model. On the other hand, the relative success on the unknown test set,  $\beta_{test}$  sets a lower bound for the model quality.

The introduction of a regularizer generally lowers the success of a given model on the training set. Intuitively, a regularizer allows to decrease the extent to which the predictions  $\hat{\mathbf{r}}$  vary when training the model on different data sets and, thus, makes the model less sensitive to a particular data set. Therefore, if correctly chosen, the regularizer prevents the model from over-fitting. Constraint parameters were chosen such that they maximize  $\beta_{test}$ .

### 2.5.9 Linear Decoding

For stimulus reconstruction and the information estimates in Sections 3.2 and 3.3, I used linear decoding (Dayan and Abbott, 2001; Rieke et al., 1999). In both sections the stimulus was a white-noise rotation or translation profile parameterized by the time-varying, three-dimensional rotation axis  $\mathbf{R}(t)$  or the translation axis  $\mathbf{T}(t)$  (see Methods 2.4.3 and 2.4.4). I tested how well the x-, y- or z-component of  $\mathbf{R}(t)$  or  $\mathbf{T}(t)$  can be reconstructed given a (recorded or simulated) spike train  $\mathbf{r}$ . In the following,  $\mathbf{v}$  denotes either the x, y, or z-component of  $\mathbf{R}(t)$  or  $\mathbf{T}(t)$ . To obtain a linear estimate of  $\mathbf{v}$ , the spike train  $\mathbf{r}$  is filtered with a linear kernel  $\mathbf{g}$ ,

$$\hat{v}_i = \sum_i \mathbf{r}_i \cdot \mathbf{g}.$$

The optimal kernel  $\mathbf{g}$  was determined by minimizing the mean squared error between the actual and the estimated stimulus,  $1/n \sum_i (v_i - \hat{v}_i)^2$ . I minimized this error term using Bayesian linear regression (Bishop, 2008). The reconstruction quality was evaluated by means of a five-fold cross-validation on single trials. Comparison of the power spectrum of the stimulus  $P_v(f)$  and the power spectrum of the estimate,  $P_{\hat{v}}(f)$ , gives a lower bound of the information,  $I_{LB}$ , transmitted by the spike train (Borst and Theunissen, 1999; Rieke et al., 1999), i.e.

$$I_{LB} = \int_0^\infty \log_2(P_v(f)/P_{\hat{v}}(f)) df. \quad (2.40)$$

$I_{LB}$  measures the information in bits/s. Dividing  $I_{LB}$  by the mean firing rate gives an information estimate in bits/spike referred to as  $I_{spike}$ .

### 2.5.10 Self-Motion Tuning Maps

Self-motion tuning maps are two-dimensional tuning curves representing the rotation or translation tuning of a given tangential cell. They were calculated for the white-noise self-motion stimuli (see Methods 2.4.3 and 2.4.4). To reduce the dimensionality of the rotation profile  $\mathbf{R}(t)$  and translation profile  $\mathbf{T}(t)$  to two dimensions, rotation and translation axes were represented in spherical coordinates by their azimuth and elevation angle. Note that by this representation the length of the rotation or translation axes (i.e. the rotation or translation velocity) is neglected. To account for the neurons' response delay, I convolved the rotation or translation profile,  $\mathbf{R}(t)$  or  $\mathbf{T}(t)$ , with the optimal linear filter mapping  $\mathbf{R}(t)$  onto the recorded firing rate. I then calculated for each rotation or translation axis the mean firing rate which was color-coded on a sinusoidal projection of a sphere yielding a two-dimensional tuning map  $T(\phi, \theta)$ . The azimuth tuning  $T_\theta(\phi)$  is calculated by averaging over

all elevation angles:  $T_\theta(\phi) = 1/\pi \int_{-\pi/2}^{\pi/2} T(\phi, \theta) \cos(\theta) d\theta$ . The elevation tuning is computed analogously by  $T_\phi(\theta) = 1/(2\pi) \int_{-\pi}^{\pi} T(\phi, \theta) \cos(\theta) d\phi$ .

# Chapter 3

## Results

### 3.1 The Spatio-Temporal Response Properties of the Tangential Cells

Previously, the spatial and temporal response properties of the lobula plate tangential cells have been characterized separately. The spatial receptive fields have been determined by presenting local stimuli (Krapp and Hengstenberg, 1996; Krapp et al., 2001) (see Introduction 1.2.6). These experiments allowed calculating the preferred motion direction of tangential cells at various positions in visual field. The resulting static receptive fields describe the spatial arrangement of local motion sensitivities, but disregard the dynamics of the neural response. On the other hand, purely temporal aspects of motion processing have been studied in experiments where the tangential cell H1 was stimulated with global gratings moving according to a white-noise velocity profile (see Introduction 1.2.7). Temporal filters mapping the stimulus velocity onto the neural response gave insight into the dynamic features of H1, however neglecting the spatial dimension of the receptive field.

I developed two stimuli which allow studying both the spatial and temporal properties of the tangential cells simultaneously in a combined approach. The first stimulus represents a global white-noise motion stimulus comprising several dots moving randomly on the stimulus screen and is referred to as Brownian motion stimulus. To describe the motion-processing by the neurons, I fitted an LN-model adopted for optic-flow processing neurons. Varying the number of moving dots also allows for studying to what extent the response properties of the tangential cells depend on the motion density.

The second approach applied to estimate the dynamic receptive fields is a purely local method. The recorded cells are locally stimulated by presenting a small sine grating moving

horizontally or vertically according to a white-noise profile. This so-called local white-noise stimulus allows estimating how the reliability, by which motion stimuli are encoded, differs depending on the location in visual space.

### 3.1.1 Processing of Sparse and Dense Motion

#### Dynamic Receptive Fields of Optic-Flow Processing Neurons

To address both the spatial and dynamic features of the tangential cells, I first presented a global white-noise stimulus to the fly, while recording the neural response (firing rate) of the tangential cells H1, H2, V1, V2 and Vi. More specifically, the stimulus comprised several dots, each of which performed a random walk within the stimulated visual space, guaranteeing that the stimulus is spatially uncorrelated. Consequently, at each time point, several positions were simultaneously stimulated. To study the impact of the stimulus strength on the cells' properties, I varied the number of motion cues in each recording: During sparse motion only 6 dots were shown, while the dense motion stimulus comprised 120 dots. Both stimulus conditions are displayed in Figures 3.1A and B along with example responses of a single H1 neuron.

Among the recorded cell types, the tangential cells H1 and Vi exhibited the highest mean firing rates during sparse and dense motion presentation (Figure 3.1C). Generally, an increase in the motion density resulted in significantly higher mean firing rates, with an almost twofold increase for the H1 neuron. To evaluate the response reliability to repeated presentations of the same stimulus, I measured the signal-to-noise ratio for firing rates binned in 5ms. Among all cells, H1 responded most reliably, both during sparse and dense motion (Figure 3.1). Both H1 and Vi exhibited a significant increase of the response reliability during dense motion. The remaining cells shows a similar trend, though not significant.

To characterize both the spatial and temporal properties of large-field optic-flow processing neurons, I adopted the linear-nonlinear (LN) model (see Figure 3.2A). The first stage of the LN-model consists of a set of linear filters, processing horizontal or vertical motion at each spatial location, which thereby capture both the temporal and spatial properties of the studied neuron. The output of the linear stage is then summed and fed through a static nonlinearity. This nonlinearity can be interpreted as the neural input-output relation that transforms the filtered local dot velocities to the firing rate. For the Brownian motion stimulus, the velocity of a dot was defined as its positional change within two successive frames times the frame rate. The linear stage of the LN-model attributes to

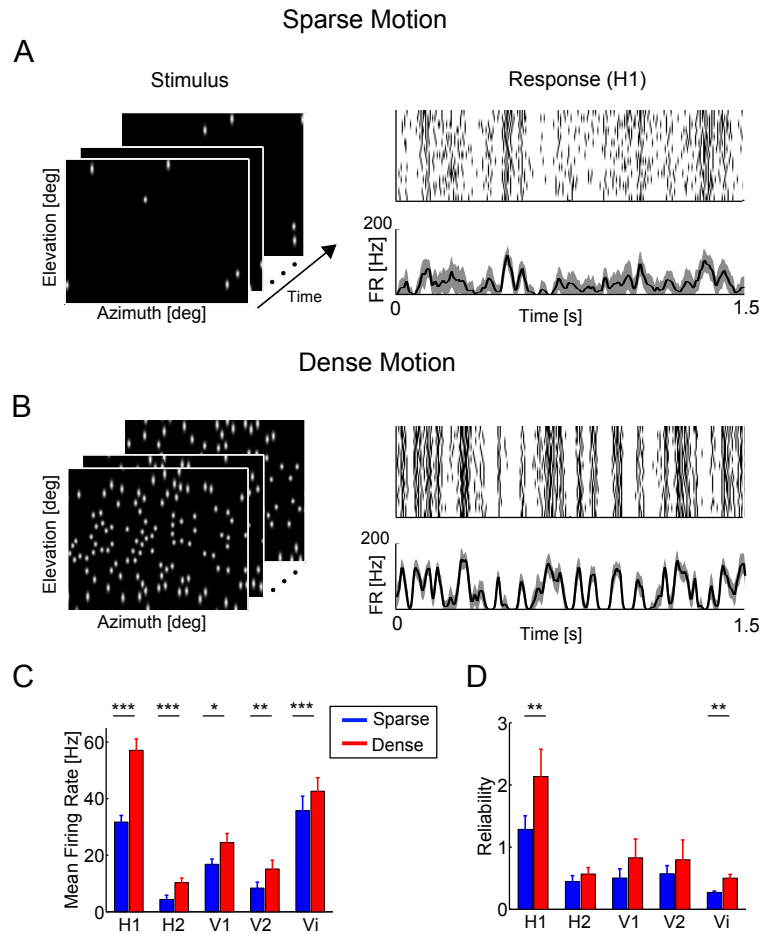
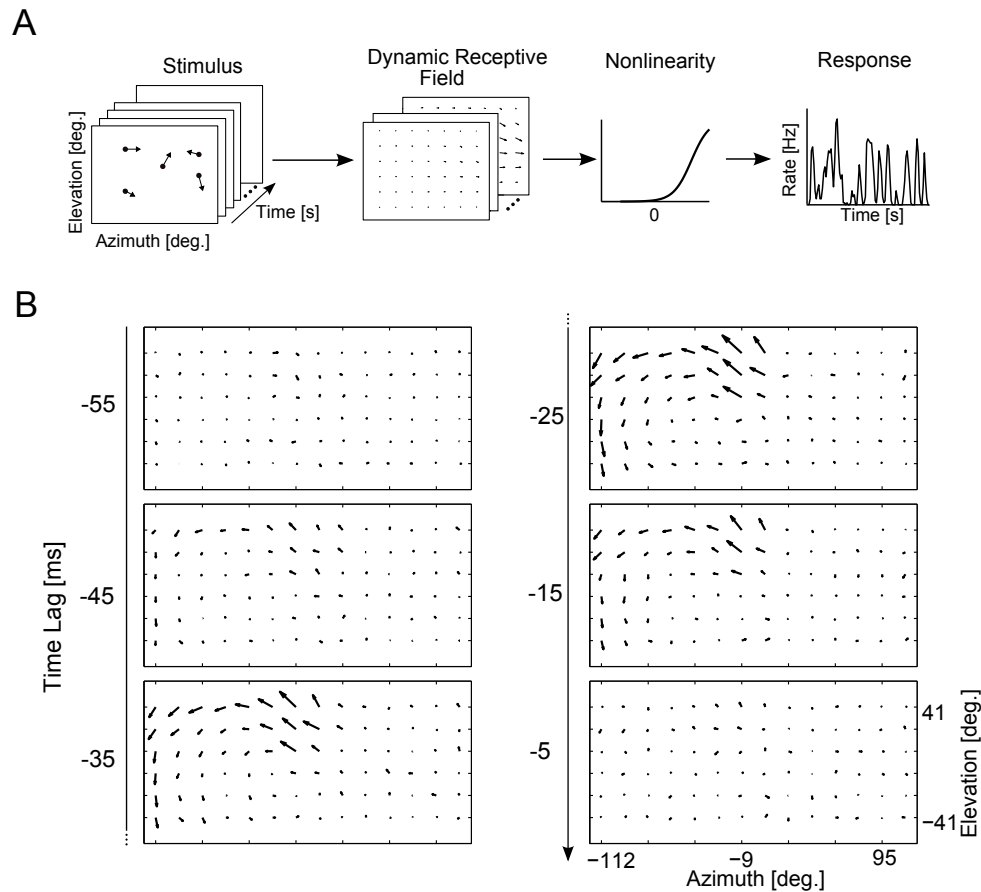


**Figure 3.1: Tangential Cell Responses to the Brownian Motion Stimulus.** (A-B) Frames of the Brownian motion stimulus along with responses of the H1 neuron. The Brownian motion stimulus comprises several dots that randomly move across the stimulated visual space and cover  $242^\circ$  in azimuth and  $96^\circ$  in elevation direction. The fly faced the center point ( $0^\circ, 0^\circ$ ). In the sparse motion stimulus condition, 6 dots were shown (A), compared to 120 dots in the dense motion condition (B). Sparse motion elicits weaker and less reliable responses. The repeated spike responses are represented in a raster plot (top) and in a trial-averaged peri-stimulus time histogram (PSTH); the gray shading depicts the standard deviation of the PSTH. (C) Mean firing rates of the five recorded neurons. Presentation of the dense motion condition (Dense, red) elicited higher firing rates than sparse motion (Sparse, blue). Error bars denote the S.E.M. Significant differences (based on a paired t-test) are indicated by asterisks (\* $p < 0.05$ , \*\* $p < 0.01$ , \*\*\* $p < 0.001$ ). (D) Reliability of responses to sparse and dense motion. An increase of the density of the presented motion cues results in an increase of the reliability. Reliability was calculated as the signal-to-noise ratio for firing rates binned in 5ms. Error bars represent the S.E.M. (\*\* $p < 0.01$ ).

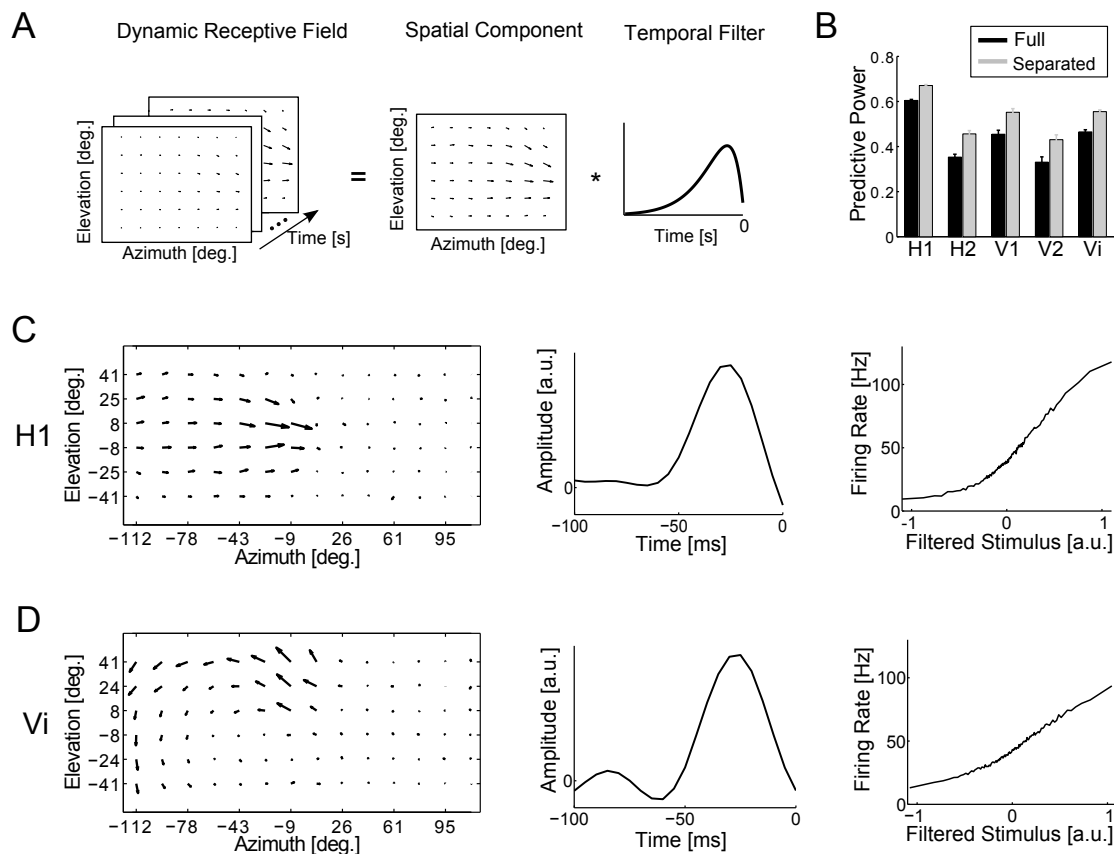
each position two components weighting the local horizontal and vertical velocity. These two components can be represented as a two-dimensional vector. Intuitively, the direction of this vector indicates the local preferred direction, and the vector length the cell's local motion sensitivity. Considering all positions in visual space finally yields a vector field, describing the preferred motion pattern of the cell. However, since the linear stage also comprises a temporal component, it becomes a time-varying vector field (see Figure 3.2A) which is referred to as dynamic receptive field (DRF). In its discrete form, the DRF consists of a temporal series of vector fields. To estimate the DRF of the investigated neurons, least-squares techniques were applied which account for the high stimulus dimensionality (Bishop, 2008) (see Methods 2.5.2).

Figure 3.2B depicts the DRF of the Vi neuron, estimated for sparse motion. Starting from 45 ms preceding the predicted response bin, Vi exhibits an increasing sensitivity to a rotational optic-flow which then vanishes in the last frame. The vector fields from -45 to -15 ms strongly resemble the optic-flow pattern as induced by a self-rotation around a rotation axis pointing toward an azimuth and elevation angle of about  $-43^\circ$  and  $-8^\circ$ , respectively. Inspection of the DRF suggests that, instead of a whole series of vector fields, a single spatial and temporal component might be sufficient to fully capture the spatio-temporal properties of Vi: A single vector field or static receptive field indicating the preferred optic-flow pattern and a temporal filter modulating this spatial component in time. In this case, the DRF is formally described by the product of a single spatial and temporal component (Figure 3.3A), i.e. it is space-time separable. This would imply that the dynamic processing properties are independent of the location in the receptive field and that the vector orientations, i.e. the local preferred directions, do not change over time.

To test whether the DRFs of the tangential cells are indeed space-time separable, I first determined for each studied cell the components of the LN-model and then compared the performance of the unmodified full DRF to the product of its most significant spatial and temporal component (see Methods 2.5.3). The quality of a given DRF was quantified by the predictive power, defined as the percentage of the stimulus-related response captured by the model (Sahani and Linden, 2003). Figure 3.3B shows the predictive power values for the sparse motion stimulus. For all five cells, separating the DRF into a single spatial and temporal component even increased the performance of the model. The same result was also found for dense motion (data not shown). Hence, a spatial receptive field and a temporal filter are sufficient to describe the linear component of the LN-model. Figures 3.3C and 3.3D show the spatial and temporal components of a single H1 and Vi cell. In general, H1 is mainly sensitive to back-to-front motion in the left visual hemisphere



**Figure 3.2: Dynamic Receptive Field of Vi.** (A) Diagram of the linear-nonlinear (LN) model adopted to optic-flow processing neurons. The LN-model was estimated on a parameterized version of the stimuli specifying for each time point and dot a horizontal and vertical velocity value. First, the (velocity) stimulus is passed through a spatio-temporal linear filter, represented as a time-varying vector field (Dynamic Receptive Field, DRF). The output of the DRF is finally mapped by a static nonlinearity onto the firing rate. (B) Dynamic receptive field (DRF) of the Vi neuron. The DRF was estimated for a firing rate binned in 5 ms. The DRF exhibits from -45 ms on an increasing sensitivity to a rotational optic-flow pattern, vanishing at -5 ms. (For visibility, only every second kernel frame is shown). The time lags indicate the time relative to the response bin to be predicted.



**Figure 3.3: Space-Time Separated Dynamic Receptive Fields of an H1 and Vi Neuron for Sparse Motion.** (A) A single spatial and temporal component was separated from the linear DRF, and then approximated the DRF as a product of these components. (B) Predictive power values for the sparse motion condition. For all neurons, the predictive power of the space-time separated DRF (Separated) is higher than for the full DRF (Full). (C-D) Components of the linear-nonlinear (LN) model for a single H1 and Vi cell estimated for sparse motion. (Left) Spatial component of the H1 and Vi cell. (Middle) Temporal components of H1 and Vi. (Right) Static nonlinearities for H1 and Vi.

(negative azimuth angles). However, the response strength depends on the location and is strongest in frontal regions around the equator (Figure 3.3C left). The spatial component of H1 is similar to the static receptive field (spatial map of local preferred directions) as determined in a previous study (Krapp et al., 2001). The spatial component of Vi (Figure 3.3D left) is similar to the vector fields at -45 to -25 ms of the DRF presented in Figure 3.2B. The temporal components of H1 and Vi both peak at -25 ms (Figures 3.3C and 3.3D middle), and then decay to zero for increasing negative time points. The output of the DRF is transformed by a static nonlinearity (input-output relation) to the firing rate (see Figure 3.2A). H1 exhibits a sigmoidal nonlinearity with a decreasing slope for small and large input values (Figure 3.3C right). In contrast, the input-output relation of Vi is rather linear (Figure 3.3D right).

### The Input-Output Relation of the Tangential Cells Depends on Motion Density

To study whether the receptive fields of the tangential cells depend on stimulus strength controlled by the density of the motion cues, I systematically compared the responses of each cell type to both sparse and dense Brownian motion stimuli. To test for changes in the spatial components of H1, I calculated the mean motion sensitivity as a function of the azimuth angle for both stimulus conditions. As shown in Figure 3.4A (left), the tuning of the mean motion sensitivity is slightly sharper for dense motion when compared to sparse motion. To quantify the effect of the motion density on the spatial component of Vi, the motion sensitivities were averaged along a circular path that was centered on the midpoint of the rotational flow field of Vi (see inset Figure 3.4B left). Vi's motion sensitivity is only weakly modulated by the number of motion cues. Similarly, the spatial components of the remaining tangential cells are only slightly affected by changes in the motion density (data not shown).

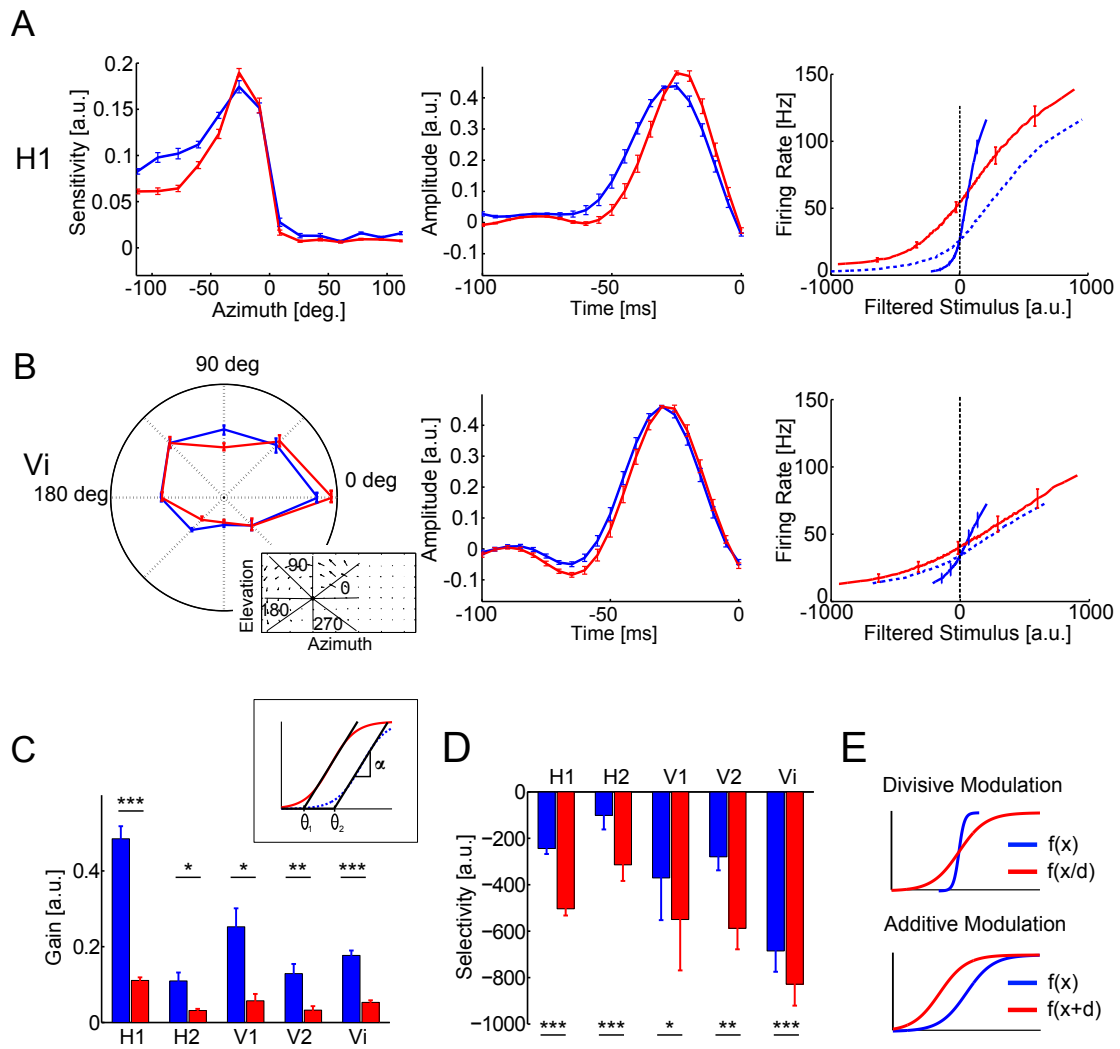
Figure 3.4A (middle) depicts the temporal components of the H1 neuron for both stimulus conditions, when averaged over all H1 recordings. During dense stimulation, H1 integrates over a slightly shorter stimulus history. Similarly, the temporal components of Vi (Figure 3.4B middle) and the tangential cells H2, V1 and V2 are only weakly modulated by the motion density (data not shown). The finding that the linear component of the LN-models is only weakly affected by the motion density implies that a DRF estimated for dense motion should also perform well for predicting the neural response to sparse motion. Indeed, I found that exchanging the spatial and/or temporal component determined for sparse motion with the respective component(s) for dense motion reduces the predictive power of H1 and Vi only slightly (data not shown). Figures 3.4A and 3.4B (right) show

the static nonlinearities of the LN-models for H1 and Vi averaged over all recordings for both stimulus conditions. Compared to the spatial and temporal components, the static nonlinearities exhibit pronounced changes: For dense motion, the slope of these nonlinearities decreases strongly. Since the reduction of the slope is equivalent to a smaller neural gain, the larger input range during dense motion (along the x-axis) is mapped onto a response interval (along the y-axis) comparable to that for sparse motion. For the other cells, the gain was likewise significantly reduced for stimuli with higher motion density.

To quantify these changes, I fitted for each neuron a half-wave rectifier to the static nonlinearity (see inset Figure 3.4C and Methods 2.5.4). The gain of each cell was then quantified as the slope of the half-wave rectifier. For all cells, the gain was significantly reduced by a factor of 3.3-4.4 when presenting the dense instead of the sparse motion stimulus (Figure

---

**Figure 3.4 (following page): Changes in the Input-Output Relation Due to an Increase of the Motion Density.** (A) Comparison of the spatial (left) and temporal components (middle) and the static nonlinearities (right) for sparse and dense motion of H1. (Left) Sensitivity tuning of H1 for sparse (Sparse, blue) and dense motion (Dense, red). The mean motion sensitivity was calculated for each azimuth angle. The resulting tuning curves were averaged over all H1 recordings ( $n=10$ ). The motion sensitivity at a particular position is defined as the length of the corresponding vector in the spatial component. Error bars denote the S.E.M. (Middle) Averaged temporal components for sparse (blue) and dense motion (red) of H1. (Right) Static nonlinearities of H1 averaged over all recordings (error bars: S.E.M). An increase of the motion density resulted in a decrease of the slope (gain) of the nonlinearity, also called a divisive modulation of the nonlinearity. The blue dashed line shows the nonlinearity for sparse motion when re-scaled by a factor of 4.6. Compared with the re-scaled nonlinearity for sparse motion, the nonlinearity for dense motion (red) is shifted to the left, also called an additive modulation of the nonlinearity. (B) (Left) Spatial sensitivity tuning of Vi for sparse (blue) and dense motion (red). For Vi, we calculated the mean sensitivity for eight sectors of a circle centered at the point  $(-43^\circ, -8^\circ)$  (see inset for illustration). (Middle) Averaged temporal components for Vi. (Right) Averaged static nonlinearities for Vi. The rescaled nonlinearity (blue dashed line) for sparse motion was scaled by a factor of 3.2. (C-D) The neural gain and selectivity during sparse and dense motion for all recorded fly tangential cells. The gain and selectivity for each recording and stimulus condition were determined by fitting a half-wave rectifier to the corresponding static nonlinearity. The gain is defined as the slope  $\alpha$  (see inset). The neural selectivity for dense motion is given by the offset  $\theta_1$ . For sparse motion, we defined the offset  $\theta_2$  of the re-scaled nonlinearity (blue dashed line) as the selectivity. The relative offset  $\theta_2 - \theta_1$  corresponds to the additive shift of the nonlinearity induced by the increase of the motion density. (E) Scheme illustrating the modulations of the static nonlinearity induced by the increase of the motion density. (Top) A divisive modulation of the nonlinearity  $f(x)$  (red) rescales its shape yielding the blue curve. Formally this rescaling can be expressed as  $f(x/d)$  for  $d>1$ . (Bottom) A leftwards shift of  $f(x)$  (resulting in the blue curve) is formally given by  $f(x+d)$  for  $d>0$ .



3.4C). Further investigation shows that the gain change with motion density is mostly divisive, i.e. it can be explained by rescaling or stretching the x-axis: If  $f(x)$  describes the nonlinearity for sparse motion, a divisive modulation of the input-output relation by the increased motion density can be expressed as  $f(x/d)$  (see Figure 3.4E, Divisive Modulation). Figures 3.4A and 3.4B (right) show rescaled versions of the nonlinearities of H1 and Vi for sparse motion (blue dashed lines). These rescaled nonlinearities for sparse motion are similarly shaped as the original nonlinearities for dense motion, yet they do not overlap precisely. Especially for H1, the nonlinearity for dense motion is shifted to the left. Such an additive modulation of the input-output relation can be expressed as  $f(x+d)$  (see Figure 3.4E, Additive Modulation). The shift of the nonlinearity lowers the selectivity of the neuron so that even weaker stimuli, e.g., those that only poorly match the receptive field, are sufficient to elicit a response. We quantified this neural selectivity as the offset of the fitted half-wave rectifier (see inset Figure 3.4C and Methods 2.5.4). For comparability, the selectivity for sparse motion is defined as the offset of the rescaled nonlinearity (blue dashed lines in Figures 3.4A and 3.4B, right). All cells showed a significant reduction of their selectivity (Figure 3.4D). The selectivity of H1 and V2 was decreased by a factor of 2.1, whereas Vi only showed a reduction of its selectivity by a factor of 1.2.

### A Biophysical Model for Gain and Selectivity Control

To unravel the biophysical mechanisms that could underlie the observed divisive and additive modulation of the static nonlinearities, the LN-model was extended to incorporate explicit biophysical elements. To develop this biophysical model, the fly tangential cells were described as finite cables integrating the synaptic inputs provided by pre-synaptic, retinotopically arranged elementary motion detectors (see Methods 2.5.1). These local motion-sensitive elements are well described by the Reichardt model (Reichardt, 1961). A single Reichardt detector comprises two subunits whose outputs are finally subtracted from each other. In each subunit, the incoming luminance signal is delayed through low-pass filtering and multiplied with the high-pass filtered signal of the second subunit. Experimental studies demonstrated that the subtraction is biophysically implemented via an excitatory and inhibitory synapse connecting each subunit to the dendrite of a tangential cell (Single et al., 1997).

For the biophysical model I simulated the motion processing of the local motion detectors presynaptic to the tangential cells by feeding the presented luminance stimuli through a two-dimensional array of horizontally and vertically oriented Reichardt detectors (RDs in Figure 3.5A). The processing by the Reichardt detector array can be viewed as an

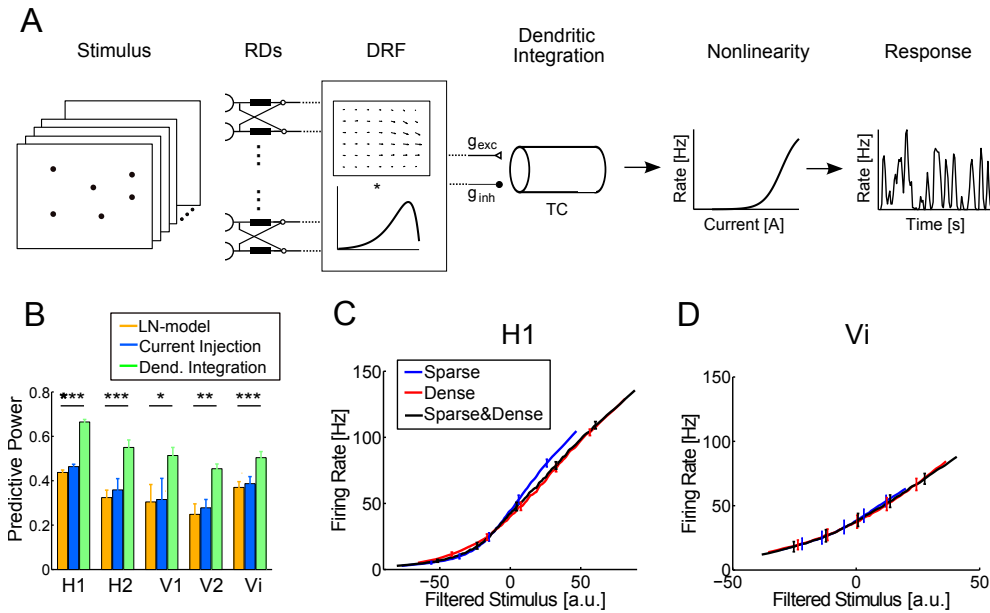


**Figure 3.5: Biophysical Model for Optic-Flow Processing Neurons.** (A) Schematic diagram illustrating the biophysical model. First, the (luminance) stimulus is fed through a two-dimensional array of Reichardt detectors (RDs). The output signals of the Reichardt detector subunits are filtered with a space-time separated dynamic receptive field (DRF), thereby yielding a total excitatory and inhibitory conductance  $g_{exc}$  and  $g_{inh}$ . Dendritic integration of the excitatory and inhibitory inputs in a tangential cell (TC) modeled as finite cable results in a current which is finally transformed to the firing rate (Response) through a current-discharge curve (Nonlinearity). (B) The nonlinear dendritic integration enhances the predictive power. The performance of the biophysical model (Dendritic Integration, green) is compared to the LN-model (LN, orange) and an alternative model where the dendritic integration was replaced by a weighted linear summation of the Reichardt detector outputs (Current Injection, blue). All models were trained on the whole data set comprising both dense and sparse motion. For each neuron the performance increase of the biophysical model is significant (\* $p < 0.05$ , \*\* $p < 0.01$ , \*\*\* $p < 0.001$ ). The significance of the performance increase was tested by comparing the predictive power of the control model (Current Injection) with the biophysical model (Dendritic Integration). Error bars represent the S.E.M. (C-D) Static nonlinearities of the biophysical model for H1 (C) and Vi (D). For both neurons, the nonlinearity estimated for both stimulus conditions (black) is shown together with nonlinearities determined separately for sparse and dense motion (blue and red). The close overlap of the nonlinearities indicates that the nonlinear dendritic integration indeed compensates for the divisive and additive modulation of the nonlinearity.

alternative approach for estimating the local velocities of the moving dots, which, for the LN-model, were determined by explicitly attributing to each dot a velocity vector (given by the dot's displacement within two successive frames). However, the Reichardt detector array additionally allows us to incorporate the conductances of the excitatory and inhibitory synapses between the pre-synaptic motion elements and the tangential cells.

The output signals of the Reichardt detectors are filtered using a space-time separated dynamic receptive field (DRF in Figure 3.5A). The horizontal and vertical vector elements of the spatial component are interpreted as the strengths (weights) of the synapses between horizontally or vertically tuned Reichardt detectors and the tangential cell's dendrite. The temporal component accounts for delays in the motion processing system and might additionally improve the prediction of the Reichardt detectors through linear filtering. Convolution of the excitatory and inhibitory Reichardt detector outputs with the dynamic receptive field yields a prediction of the total excitatory and inhibitory conductance input,  $g_{exc}$  and  $g_{inh}$ , into the tangential cell's dendrite. These conductance inputs are then integrated within the dendrite of the tangential cell (modeled as finite cable) and thereby transformed into a prediction of the inflowing current (Dendritic Integration in Figure 3.5A). Here, I considered current instead of voltage, since theoretical studies have demonstrated that the current flowing from the dendrite to the spike initiation zone can be studied separately from the spiking mechanism (Bernander et al., 1994; Koch et al., 1995). With this additional nonlinear stage, the biophysical model explicitly accounts for the nonlinearity imposed by the dendritic integration of synaptic inputs. Finally, the current estimate is transformed into a firing rate by a static nonlinearity, which, for the biophysical model corresponds to a current-discharge curve (Nonlinearity in Figure 3.5A). As for the classical LN-model the parameters for the spatial and temporal components, the dendritic integration in the finite cable, and the nonlinearity were directly derived from the recorded responses through minimization of an error function (see Methods 2.5.5).

To derive a formal expression for the current flowing in response to a visual stimulus, it was assumed that the studied neurons can be described as finite cables: The excitatory and inhibitory subunits of the Reichardt detectors project to one end of the cable, while the spike initiation zone is positioned at the other end. Moreover, I assumed that the passive dendrite is separated from the spike initiation zone by a large electrotonic distance. Since the tangential cells exhibit small time-constants in the range of a few milli-seconds (Borst and Haag, 1996), only the steady-state current was considered.

The motion prediction by the Reichardt detector array is given by the difference of the total excitatory and inhibitory conductance,  $g_{exc}$  and  $g_{inh}$ : If the Reichardt detector array prediction was provided as current injections to the dendrite, the inflowing current would

be proportional to the motion prediction  $x = g_{exc} - g_{inh}$ . However through dendritic integration,  $x$  is nonlinearly transformed to the current  $I_{siz}$  flowing to the spike initiation zone. This current can be approximated by

$$I_{siz}(x) = z + \frac{Ax}{\underbrace{g_{exc} + g_{inh} + c}_{I_{bal}}} + \frac{Dg_{exc}}{\underbrace{g_{exc} + g_{inh} + c}_{I_{diff}}} \quad (3.1)$$

( $A$ ,  $c$ ,  $D$  and  $z$  are parameters independent of synaptic conductances). The first term,  $I_{bal}$ , denotes the current if the driving forces for excitatory and inhibitory currents are balanced; The second term,  $I_{diff}$ , denotes the additional excess current flowing if the driving forces are unbalanced; the parameter  $D$  is proportional to the difference of the driving forces. The current flowing to the spike initiation zone is then transformed into a firing rate by the current-discharge curve  $f(I_{siz})$  (Nonlinearity in Figure 3.5A).

### Dendritic Modulation of Gain and Selectivity Improves Predictions and Generalization

Figure 3.5B demonstrates that the nonlinear dendritic integration of synaptic inputs indeed enhances the quality of the model predictions. The predictive power of the biophysical model was compared with the LN-model (green and orange bars in Figure 3.5B). Here, the parameters for both models were estimated (in contrast to Figure 3.3 and 3.4) for the whole data set, i.e., for both sparse and dense motion stimuli. Since the LN-model cannot correct for changes of gain and selectivity by the motion density, its predictive power dropped significantly compared to its performance on either sparse or dense motion stimuli (see Figure 3.3B). The biophysical model with the dendritic integration mechanism significantly raised the predictive power for all cells. Thus, one biophysical model can predict the neural response to both sparse and dense motion as well as two LN-models needed to compensate for changes in the gain and selectivity due to the stimulus condition. The biophysical model is therefore more general than the LN-model.

In order to show that the performance increase is due to the dendritic integration stage, rather than pre-processing of the stimuli by the Reichardt detector array, I constructed an alternative model where the dendritic integration stage is replaced by a linear weighted sum of the Reichardt detector array outputs. Biophysically, this linear summation is equivalent to providing the synaptic outputs of the local motion detectors as current injections to the tangential cell's dendrite. The resulting model only shows a slight increase in performance when compared to the LN-model (blue bars in Figure 3.5B). Hence, the pre-processing of stimuli by the Reichardt detector array by itself does not correct for the divisive and

additive modulation of the input-output relation. This finding is in contrast to the results of experiments where H1 was stimulated with a grating moving horizontally according to a white-noise velocity profile. An increase of the amplitude of the velocity fluctuations reduced the gain of the input-output relation (Fairhall et al., 2001). For this type of stimuli, the changes in the gain could be attributed to the intrinsic nonlinearity of the Reichardt detector (Borst et al., 2005) (see Introduction 1.2.7).

Figures 3.5C and 3.5D show the current-discharge curves of the biophysical model for sparse motion, dense motion, and when both stimulus conditions are treated jointly. The strong overlap of these nonlinearities for all cells demonstrates that the biophysical model accounts for the changes of the nonlinearities by the motion density as observed for the LN-model (compare Figure 3.4A-B right). Hence, the modulations of the gain and selectivity can be attributed to a fundamental biophysical nonlinearity, the dendritic integration of synaptic inputs.

To explain how the biophysical model compensates for changes in the gain and selectivity of the studied neurons, I again refer to Equation 3.1. Since each Reichardt detector processes motion only within a small region of the visual field, a higher motion density leads to the activation of more motion detectors and their output synapses. This, in turn, results in increased total conductances  $g_{exc}$  and  $g_{inh}$ . An increased motion density, therefore, has a stronger divisive effect on the balanced current,  $I_{bal}$ : The motion prediction,  $x = g_{exc} - g_{inh}$ , of the Reichardt detector array is divided by a larger term  $(g_{exc} + g_{inh} + c)$  corresponding to a divisive rescaling of  $x$ . Hence, the gain (slope) of the input-output relation mapping local velocities onto the firing rate is reduced. In contrast, the positive excess current  $I_{diff}$  is enhanced through an increased motion density. This term can be interpreted as a depolarizing current lowering the spiking threshold, and thus induces a leftwards shift of the nonlinearity mapping  $x$  onto the firing rate. The size of the shift depends on  $D$ , i.e. the larger the excitatory compared to the inhibitory driving force, the more pronounced the leftwards shift. Hence, I hypothesize that an increase of the membrane conductance underlies a reduction of the gain, while the additive modulation of the input-output relation relies on the unbalanced driving forces for the excitatory and inhibitory currents. For both requirements there exists strong experimental evidence: During presentation of a grating moving in the preferred or anti-preferred direction the input resistance of a fly tangential cell drops considerably (Borst et al., 1995). Moreover, motion noise (incoherently moving dots) was also shown to increase the membrane conductance (Grewe et al., 2006). Evidence for a stronger excitatory driving force was provided in (Egelhaaf et al., 1989).

Finally, I asked which parameters in the biophysical model might underlie properties of the tangential cells such as mean firing rate, reliability, gain, and shifts in their selectivity

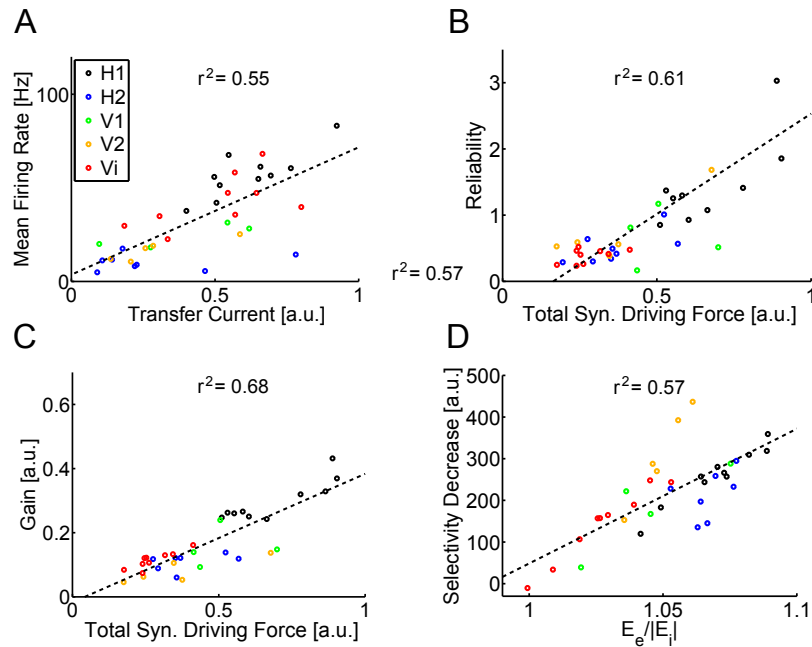


**Figure 3.6: Correlation between Tangential Cell Properties and Parameters for the Biophysical Model.** (A) Correlation between the transfer current (corresponding to the parameter  $A$  in Equation 1) and all 35 tangential cell recordings. The  $r^2$ -coefficient equals 0.55. The transfer current is proportional to the product of the input conductance and the size of the inhibitory driving force  $|E_{inh}|$  (see Equation 2.21). (B) Correlation between the measured reliabilities and the total synaptic driving force given by  $A/c$  (see Equation 2.25,  $r^2 = 0.61$ ). (C) Correlation between the neural gains and total synaptic driving force ( $r^2 = 0.68$ ). (D) The decrease of the neural selectivity induced by the increase of the motion density most strongly correlates with the ratio of the excitatory and inhibitory driving force,  $E_{exc}/|E_{inh}|$  (see Equation 2.26,  $r^2 = 0.57$ ).

due to changes in the motion density. For this purpose, I correlated all parameters of the biophysical model with the measured properties of all 35 recorded neurons. I explicitly searched for parameters which correlate most strongly with the corresponding cell property. I found that the parameter  $A$  in Equation 3.1 most strongly correlates with the mean firing rate of the neurons (Figure 3.6A). Physiologically, this parameter is proportional to the product of the input conductance of the finite cable and the size of the inhibitory driving force,  $|E_{inh}|$  (see Equation 2.21). Thus  $A$  determines the amount of current flowing to the spike initiation zone and is therefore referred to as transfer current. Assuming that the reverse potential is approximately constant for all cells, this suggests that the larger the input conductance, the higher the mean firing rate of the cell. The reliability of the recorded cells can be best explained by  $A/c$  which can be interpreted as a measure of the total synaptic driving force (see Equation 2.25). Correlating the reliability with the total

synaptic strength and additionally the transfer current, improves the  $r^2$ -coefficient only by about 2%. Hence, the reliability is primarily determined by the total synaptic driving force and not the input conductance (Figure 3.6B). The gain of the neurons is also best explained by the total synaptic driving force (Figure 3.6C). Again, the input conductance in form of the parameter  $A$  had no additional significant impact on the correlation. As shown in Figure 3.6D, the increase of the neural selectivity through an increase of the motion density correlates most strongly with  $D/A + 1$  describing the ratio of the excitatory and inhibitory driving forces,  $E_{exc}/|E_{inh}|$  (see Equation 2.26). Hence various properties of the tangential cells can be attributed to the parameters of the biophysical model which can be physiologically interpreted.

### 3.1.2 Local Reliability of Motion Processing

The Brownian motion stimulus allowed studying how the gain and selectivity of the fly tangential cells depends on the stimulus strength as controlled by the density of presented dots. Besides the dependence of the receptive fields on the motion density, I also studied the local processing properties of the tangential cells. In particular, I addressed the question, how the reliability, by which a local stimulus is represented, depends on its position in visual space. In principle, the Brownian motion stimulus could be localized by presenting only a single dot. However, to sample with a single dot the whole visual space covered by the LED-arena might take too long. Moreover, to study the local reliability requires the repeated presentation of a specific stimulus at a given position in visual space. To this end, I developed a further stimulus with the aim to investigate the local processing properties of the tangential cells. The so-called local white-noise stimulus can be seen as a local version of previous white-noise motion stimuli used for experiments with H1, where a global sine grating moved horizontally according to a white-noise velocity profile (Borst, 2003; Fairhall et al., 2001). Instead of a global grating, I presented a small grating at various positions moving in vertical and horizontal direction according to a white-noise velocity profile (Figure 3.7A; for more detail see Methods 2.4.2). Previously, it has been shown that presentation of horizontal and vertical motion is sufficient to determine the local preferred direction, since the fly tangential cells exhibit for most locations in their receptive field a sinusoidal direction tuning (Wertz et al., 2009). Hence, the local white-noise stimulus allows not only to estimate the local dynamic processing properties, but also the local preferred direction.

To estimate the dynamic receptive field, the same approach was applied as for the Brownian motion stimulus. I attributed to each time point and stimulated location the currently

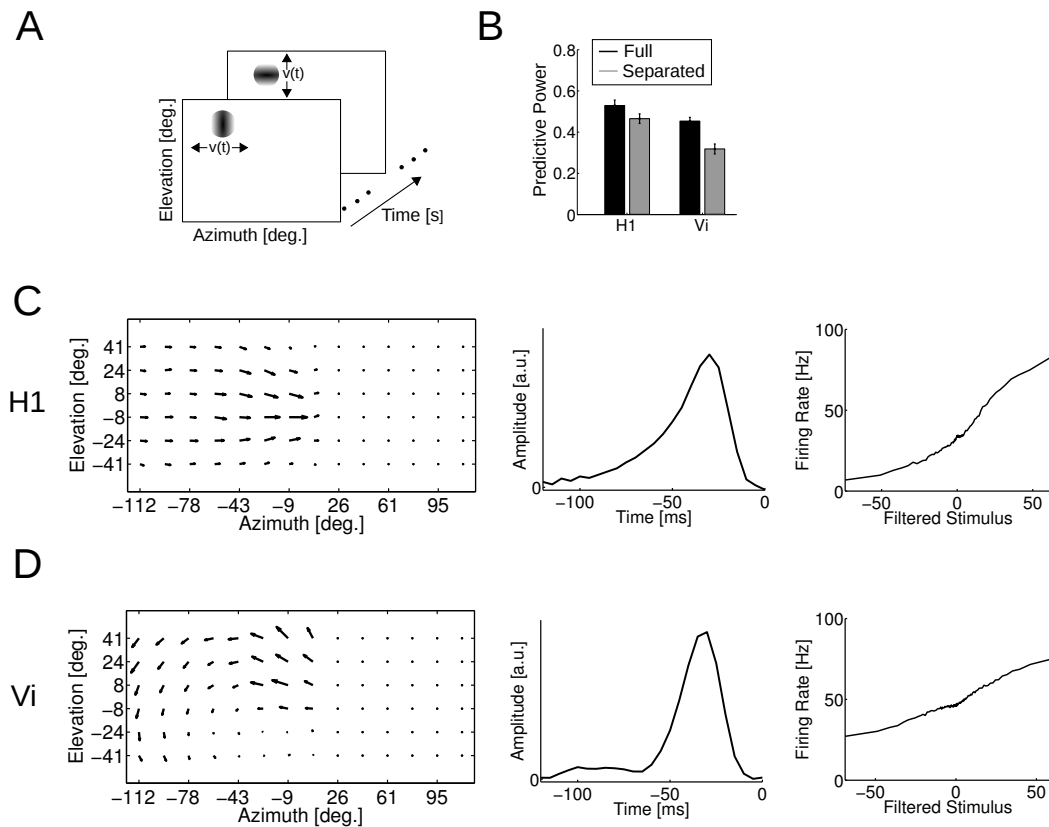


**Figure 3.7: Dynamic Receptive Field of H1 and Vi for Local White-Noise Stimulation.** (A) Scheme illustrating the local white-noise stimulus: A horizontally and then vertically oriented sine grating moves at various positions according to a white-noise velocity waveform specified by  $v(t)$ . (B) Predictive power of the dynamic receptive fields (DRFs) estimated for the local white-noise stimulus. I separated a single spatial and temporal component from the linear DRF, and then approximated the DRF as a product of these components. The resulting space-time separated DRF exhibits for both neurons a higher predictive power than the full DRF. (C,D) Components of the linear-nonlinear (LN) model for a single H1 and Vi cell estimated for the local white-noise stimulus. (Left) Spatial component of H1 and Vi. (Middle) Temporal components of H1 and Vi. (Right) Static nonlinearities for H1 and Vi.

displayed vertical or horizontal velocity value (of the corresponding sine grating) yielding a spatio-temporal stimulus parameterization. Using linear regression, I then calculated a dynamic receptive field optimally mapping the local velocity onto the recorded firing rate. Despite the differences in the stimuli, the dynamic receptive fields of H1 and Vi estimated for the local white-noise stimulus are again space-time separable. Figure 3.7B compares the predictive power of the full and space-time separated dynamic receptive fields. Moreover, the spatial components of H1 and Vi (Figures 3.7C and 3.7D, left) are quite similar to those found for the Brownian motion stimulus (compare Figures 3.3C and 3.3D). The shapes of the nonlinearities for H1 and Vi are also similar to those found for the Brownian motion stimulus (Figures 3.7C and 3.7D, right). The temporal components again peak at -25 ms, however differ in their shapes: H1's filter found for local white-noise stimulus (Figure 3.7C, middle) integrates over a longer stimulus history compared with the filter for the Brownian motion stimulus (Figure 3.3C, middle). In contrast to Brownian motion stimulation, the temporal filter of Vi exhibits no inhibitory phase (Figure 3.7D, middle). In experiments, where H1 was stimulated with global white-noise grating, it has been already demonstrated that the shape of the optimal temporal filter adapts to changes in the stimulus statistics (Fairhall et al., 2001; Safran et al., 2007; Borst, 2003; Borst et al., 2005). Hence, differences in the local statistics of both stimuli might underlie the observed changes in the temporal components.

### Local Reliability of Motion Processing

Since at each time point only one location is stimulated, the local white-noise stimulus allows assessing to what extent the response reliability depends on the stimulus position in visual space. The reliability was calculated for responses to repeated presentation of identical stimuli and was measured as the signal-to-noise ratio for firing rates binned in 5 ms (Borst and Theunissen, 1999). The maximal local reliability of H1 is nearly 3 times higher than for Vi. Moreover, the reliabilities of H1 are distributed over a larger range (reaching from 0.11 to 2.87) than for Vi, where all measured values lie between 0.28 and 0.97. As shown in Figures 3.8A and 3.8B, both neurons represent motion information most reliable in frontal regions at an azimuth of about  $-9^\circ$ . While the reliability distribution of H1 is symmetric with respect to the equator, Vi represents motion, in average, more reliably for positive elevation angles. How reliably motion is encoded at a certain position in space primarily depends on the local response power. This can be shown by correlating the local reliabilities with the local response powers (Figures 3.8C and 3.8D). In average, 97.4% and 86.1% of the variance in the reliabilities of H1 and Vi are explained by the

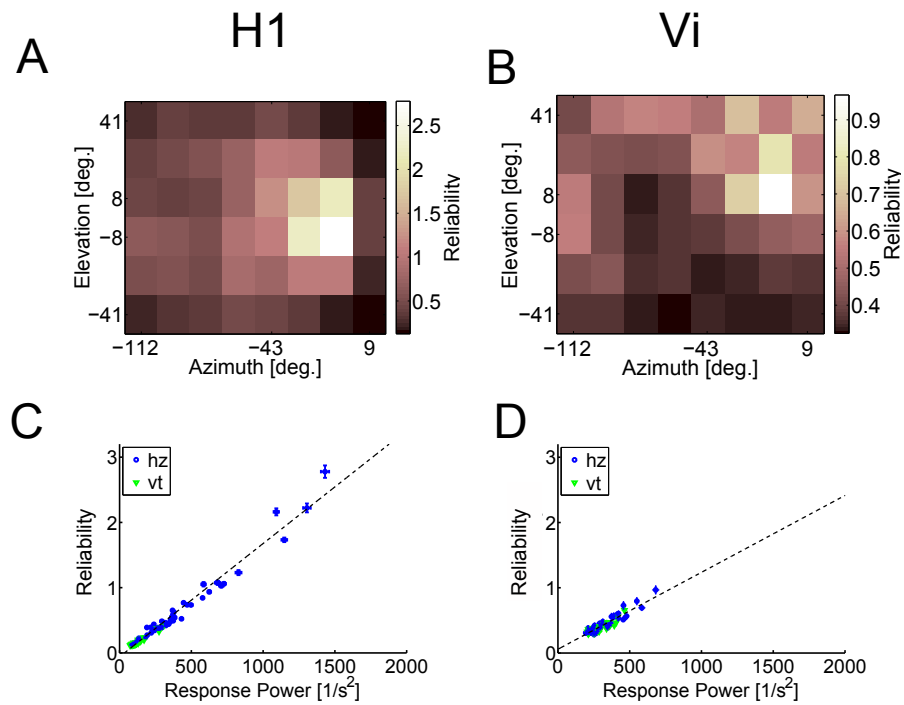


**Figure 3.8: The Reliability of the Tangential Cells Depends on the Location of Stimulation.** (A-B) The local white-noise stimulus allows determining the response reliability as a function of position in visual space. For each stimulated location, I calculated the reliability of the responses to a horizontally and vertically moving sine grating. The larger of the two resulting values was color-coded according to the color bar. Note that for better visibility the color code for Vi and H1 differs. (C-D) Correlation of the response powers and corresponding reliabilities for each location and orientation. In average, 97.4% and 86.1% of the variance in the reliabilities of H1 ( $n=5$ ) and Vi ( $n=6$ ) are explained by the local response powers. Vertical error bars show the S.E.M. of the reliability, horizontal error bars refer to the S.E.M. of the response power.

strength of the neural response.

I presented two different stimuli to characterize the spatio-temporal response properties of large-field motion-sensitive neurons of the fly and constructed LN-models to predict the neural response. In an LN-model, the neuron is modeled by a linear filter, i.e. its receptive field, followed by a static nonlinearity. For an optic-flow processing neuron, the linear filter is described by a time-varying vector field referred to as dynamic receptive field. The dynamic receptive fields of the tangential cells turned out to be space-time separable: they can be decomposed into a spatial component (a static receptive field), multiplied by a single temporal filter, modulating each vector in the same way.

The first stimulus (Brownian motion stimulus) allowed varying the stimulus strength by increasing or decreasing the number of moving dots. Increasing the stimulus strength

has only a weak impact on the spatial or temporal component of the DRF. However, it changes the nonlinearity of the subsequent processing stage: Increasing the motion density reduces the slope of the nonlinearity (gain), while increasing its offset (selectivity). Such modulations of the gain and selectivity cannot be captured by an LN-model and, therefore, prevent its generalization to arbitrary stimuli. To unravel possible mechanisms underlying these changes, I developed a biophysical model: At the first stage, the luminance stimuli are fed through an array of Reichardt detectors modeling the processing of local motion detectors. The outputs of the motion detectors are subsequently passed through a spatial and temporal filter yielding the total excitatory and inhibitory conductance of synapses impinging onto the tangential cell. This linear stage corresponds to the DRF of the LN-model. The following nonlinear stage then integrates the total excitatory and inhibitory conductance resulting in an estimate of the inflowing current. Finally, this current is mapped onto the firing rate by a static nonlinearity. As for the classical LN-model, all unknown parameters of the biophysical model were directly fit to the recorded data. Explicitly modeling the nonlinearity imposed by dendritic integration corrects for the modulations of the gain and selectivity by the motion density. Variations in the gain can be attributed to changes in the membrane conductance, while changes in the selectivity are due to an unbalance of excitatory and inhibitory driving forces on the dendrite. Hence, besides generalizing the LN-model, the new model explicitly implements dendritic integration and thereby offers a physiological explanation of functional phenomena.

The second presented stimulus (local white-noise stimulus) was developed to study the local processing properties. The reliability by which local motion stimuli are encoded strongly differs across the receptive field. For both H1 and Vi, the reliability depends linearly on the local response power.

## 3.2 Self-Motion Encoding by the Tangential Cells

The receptive fields of the lobula plate tangential cells strongly resemble optic-flow patterns as induced by certain self-motions of the animal. This strong similarity of receptive fields and optic-flow patterns lead to the hypothesis that the tangential cells act as matched filters (Franz and Krapp, 2000; Franz et al., 2004), responding strongest for specific maneuvers of the fly. In contrast to optic-flow encoding neurons in area MST of monkeys (Britten, 2008), the receptive fields of the tangential cells mainly resemble rotational optic-flow fields suggesting that these neurons rather encode rotations than translations (Krapp and Hengstenberg, 1996; Krapp et al., 1998; Borst and Weber, 2011). The stimuli presented in the

previous Section 3.1 allowed estimating the receptive fields of the tangential cells. However, the receptive fields alone do not permit to quantify how well the responses of the tangential cells encode a certain self-motion of the fly. Moreover, the previously presented stimuli were designed such as to elicit strong, easily interpretable responses. In contrast, in their natural environment, flies are confronted with strongly varying textures and inhomogeneous contrast distributions as are characteristic for natural images. Since the tangential cells seem to be mainly tuned to rotations (Krapp and Hengstenberg, 1996; Krapp et al., 1998; Borst and Weber, 2011), I studied the encoding of rotations around various body axes in single tangential cells. Moreover, I also tested how strongly the representation of rotations is disturbed by superimposed translations.

### 3.2.1 Responses to the White-Noise Self-Motion Stimulus

To quantify the robustness of the optic-flow encoding by the tangential cells, I developed the so-called white-noise self-motion stimulus (see Methods 2.4.3). A virtual fly was placed in a cube tapered with eleven different images (see Figure 3.9A). At each time point, the fly was moved according to a randomly changing translation and rotation axis fully specifying the animal's self-motion (see Methods 2.3.1). For each time point, the environment was then projected onto the virtual fly's eye (modeled by a small sphere). The resulting series of images was then displayed on the LCD-monitor setup (see Methods 2.1), while recording the firing rate of left H1, V1, or V2 cell.

Three stimulus conditions were compared: In the first condition, only rotations were presented. Secondly, a purely translational self-motion profile was presented. Finally, the rotations and translations of the two previous conditions were simultaneously displayed. Note that the self-motion stimulus is six-dimensional: At each time point the fly's self-motion is described by a three-dimensional rotation and a three-dimensional translation axis.

I verified that for each recorded cell type, the translational and rotational optic-flow was equally strong. To do so, the translation axes were first normalized by the distance of the respective receptive field to the environment such that translations and rotations are expressed in the same units (m/s) (see Methods 2.3.2). Then, for each time point, I calculated the rotational and translational optic-flow strength given the (normalized) translation and rotation axes according to Equation 2.2. The optic-flow strength or norm is computed by convolving the motion sensitivity distribution of a specific cell with the analytically derived optic-flow (see Equation 2.1). The distribution of the resulting rotational and translational optic-flow strengths are shown in Figure 3.9B. Example patches of the firing rates induced

by the same rotational or translational self-motion within the eleven different environments are depicted in Figure 3.9C. The color code of the images follows the sorting of the images in Figure 3.9A.

Especially during rotation, the time course of the firing rates exhibits a very similar shape, however strongly differs in amplitude in dependence of the environment.

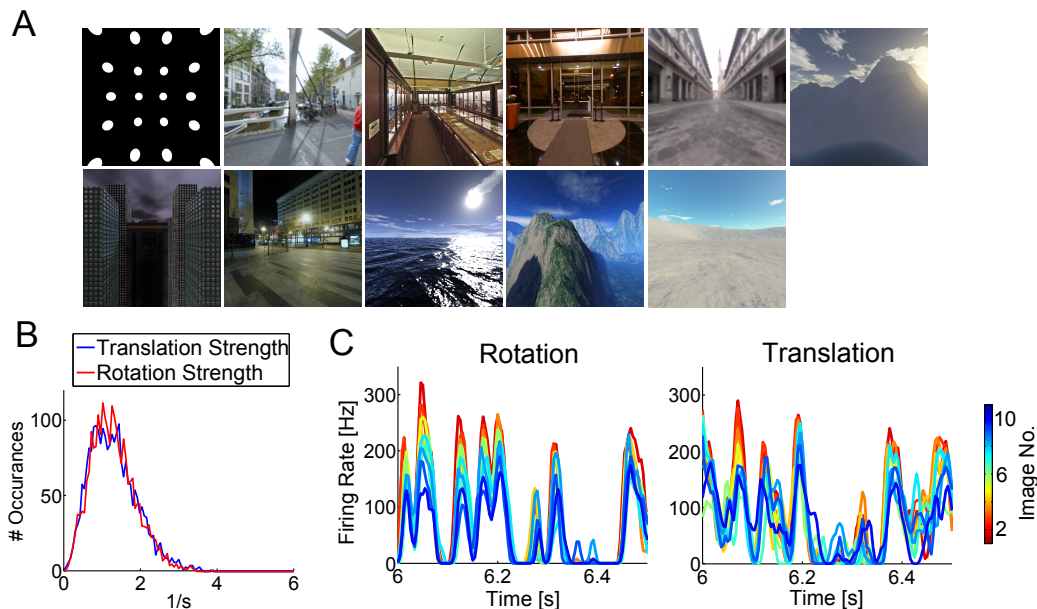


**Figure 3.9: Tangential Cell Responses to the White-Noise Self-Motion Stimulus.** (A) Environments surrounding the virtual fly. Each image shows the tapering of a single cube side. (B) Histogram of rotation and translation strength of the presented stimuli. For each time point the rotation and translation strength was quantified according to the optic-flow norm (see Equation 2.2). (C) Peri-stimulus time histograms (PSTH) of H1 for rotation and translation in all eleven environments. The color code indicates the image number. Images are sorted as in (A).

To characterize the self-motion processing by the tangential cells, I fitted the components of an LN-model which transforms the translational and rotational self-motion profile into a firing rate. Figure 3.10 shows for all environments the three rotation filters of H1 which are convolved with the x-, y-, and z-components of the rotation axes denoted by  $R_x$ ,  $R_y$ , and  $R_z$ . As expected from its receptive field (see Figure 3.3C, left), H1 is mainly sensitive to rotations around the z-axis. The nonlinearities of the LN-models of H1 are depicted in Figure 3.10B. While the normalized rotation filters closely overlap, the nonlinearities significantly differ in their gain. The images in Figure 3.9A were sorted according to H1's gain, quantified by the slope of a half-wave rectifier fitted to the nonlinearity (see Methods 2.5.4).

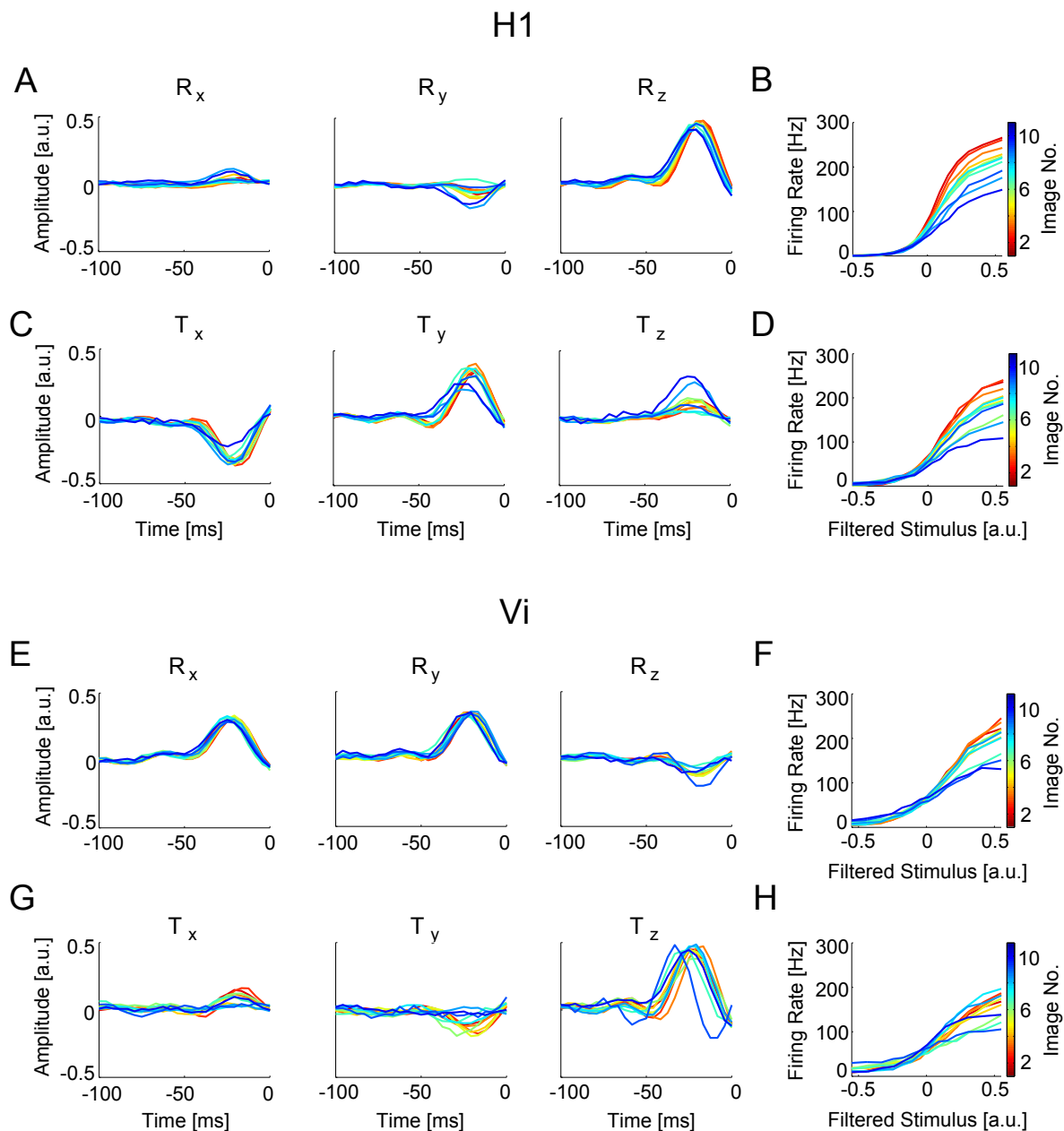


**Figure 3.10: LN-models of H1 and Vi for all Environments.** (A,B) LN-models of H1 for rotation processing in all environments. (A) Linear filters for the x-, y-, and z-component of the rotation profile. The time points on the x-axis indicate the time relative to the response bin to be predicted. (B) Nonlinearities for all environments. Rotation filters and nonlinearities were sorted according to the coloring of the color bar on the right. (C,D) LN-models of H1 for translation processing in all environments. (E,F) LN-models of Vi for rotation processing in all environments. (G,H) LN-models of Vi for translation processing in all environments.

The translational filters of H1 for the x-, y-, and z-component of the translation axes ( $T_x$ ,  $T_y$ , and  $T_z$ ) are shown in Figure 3.10C. Compared to the rotation filters, the translational filters overlap less strongly. As for rotations, the nonlinearities exhibit different gains dependent on the environment (Figure 3.10D).

The rotation and translation filters of Vi are shown in Figure 3.10E and 3.10G. As for H1, the translation filters overlap less than the rotation filters. Especially, the translational z-filters differ in their time course. Similar to H1, the gain of the nonlinearities strongly varies with the presented environment (Figures 3.10F and H). Hence, the tangential cells are sensitive to both rotations and translations, however, the encoding of rotations is more robust across different environments.

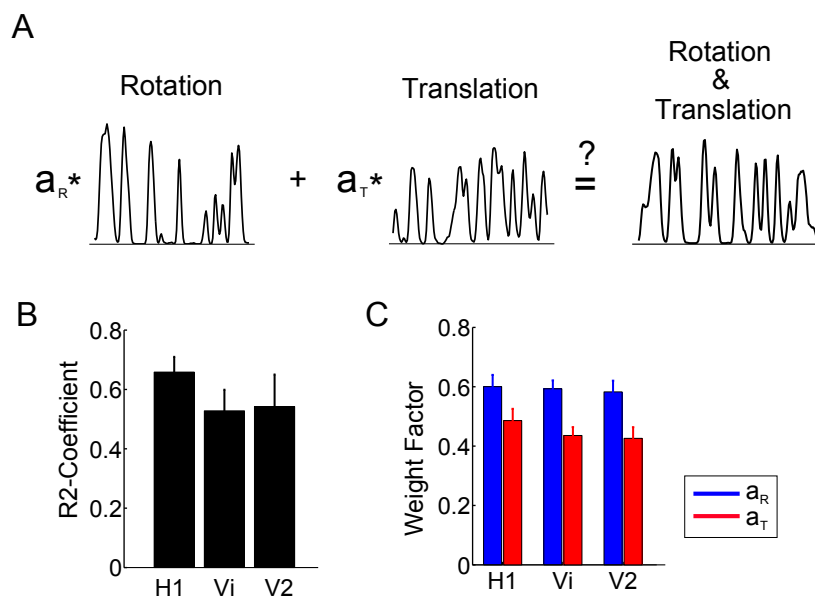


**Figure 3.11: Contribution of Rotation and Translation to the Neural Response.** (A) For each environment, I tested whether the firing rate recorded for simultaneous presentation of rotation and translation (Rotation & Translation) can be approximated as a linear combination of the firing rates recorded for separate presentation of the rotation and translation profile. The weighting factors for the rotational and translational firing rates are denoted by  $a_R$  and  $a_T$ . (B) R2-coefficient quantifying how well the firing rate for Rotation & Translation can be approximated as linear sum of the firing rates recorded separately for rotation and translation. Error bars indicate the standard deviation over all eleven environments. (C) Rotation contributes more to the combined firing rate. For all recorded cells, the weighting factor for the rotational firing rate is larger. Error bars denote the standard deviation.

Since the tangential cells are sensitive to both rotational and translational optic-flow, their responses are ambiguous. From the firing rate of a single cell it cannot be deduced, whether the response was caused by a rotation or translation. In a previous simulation study, it

was hypothesized that the strong resemblance of the receptive field with rotational flow patterns reduces the translation sensitivity of the tangential cells (Borst and Weber, 2011). To quantify whether translations are suppressed in comparison to rotations, I approximated the firing rates during simultaneous presentation of rotation and translation by a linear sum of the firing rates elicited by separate presentation of the same rotation or translation profile (see Figure 3.11A). The quality of the approximation was quantified by the  $r^2$ -coefficient, which was for all three recorded cell types above 0.5 (Figure 3.11C). Figure 3.11C depicts the weighting factors for the rotational and translational firing rates. For all three cell types, the contribution of the rotational rate is significantly larger. This finding suggests that the tangential cells are less sensitive to translations than rotations.

Consequently, their responses should convey more information about rotational compared to translational optic-flow. To quantify the amount of information, I tested, how well each of the self-motion components can be reconstructed from a single-trial response using an optimal linear filter (see Methods 2.5.9). Comparison of the power spectra of the real and estimated stimulus gives a lower bound on the information carried by the spike train quantified in Bits/s (Rieke et al., 1999; Borst and Theunissen, 1999).

To reduce the dimensionality of the stimulus, the three-dimensional rotation and translation profiles were projected onto the preferred rotation and translation axis of the respective cell. Hence, I quantified how well a tangential cell represents rotations or translations around its preferred rotation or along its translation axis.

The blue and red solid lines in Figures 3.12A-C show the information that H1, Vi, and V2 carry about rotations and translations, when presenting only rotational or translational self-motions. In average, each cell type carries more information about rotations than translations. As shown by the dashed lines, the encoding of rotations or translations is strongly impaired, when simultaneously presenting both self-motion profiles. However, the information about rotations is less affected than the representation of translations. This finding again suggests that tangential cells are more sensitive to rotations than translations. During presentation of a single self-motion component, the stimulus representation strongly depends on the environment. Figure 3.12 demonstrates that the information about rotations linearly depends on the neural gain. The gain of a cell for a specific environment was quantified by the slope of a half-wave rectifier fitted to the nonlinearity of the corresponding LN-model.

In summary, I quantified the representation of rotations and translations by the responses of the tangential cells. Thereby, I especially tested the robustness of the representation of rotations and translations in different environments. Through the analysis of LN-models and a linear decoding approach, I found that the tangential cells exhibit a stronger sensi-

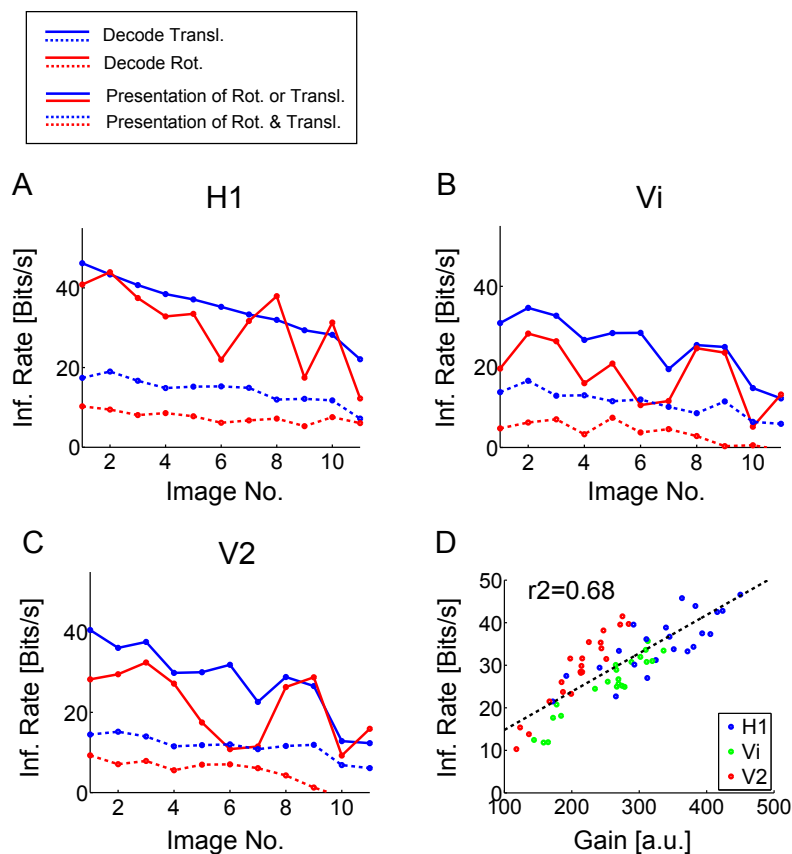


**Figure 3.12: Decoding of Rotational and Translational Self-Motion.** (A-C) Optimal linear decoding was applied to test how well the rotation or translation profile can be reconstructed from the single-trial firing rates. The solid lines show the decoding performance for separate presentation of translation or rotation. For all three cells, rotation (blue) is slightly better represented than translation (red). The dashed lines show the decoding performance of rotation (blue) and translation (red), if rotation and translation are simultaneously presented. The representation of both rotation and translation is significantly reduced. However, the information about rotation is less affected by the simultaneous presentation of translation than vice versa. (D) The information about rotation linearly depends on the neural gain. Each dot represents the gain and information of the H1 (blue), Vi (green), or V2 (red) cell of a single fly in one of the eleven environments. The  $r^2$ -coefficient equals 0.68.

tivity to rotations. Consequently, the responses of the neurons contain more information about rotations than translations.

### 3.3 The Functional Role of an Inter-Hemispheric Projection

The complex receptive fields of the lobula plate tangential cells arise from the integration of signals from pre-synaptic elementary motion detectors and lateral interactions between other tangential cells Borst et al. (2010); Borst and Weber (2011). Due to their receptive fields the tangential cells are tuned to specific self-motions. In the previous sections, I presented approaches which allow mapping the spatio-temporal receptive field properties of a tangential cell and determining the self-motion tuning arising from the receptive field. However, these methods do not unravel how the receptive field and stimulus tuning of a particular cell arises from its underlying connectivity. The receptive field does not account for the different origins of the inputs to a sensory neuron. Consequently, it does not allow describing the impact of a specific lateral connection on stimulus processing. The lateral interaction of a pair of neurons is typically described by correlating their simultaneously recorded responses. However, the resulting cross-correlation does not reveal to what extent the coupling influences the properties of a single neuron. If a neuron e.g. receives an excitatory input from a further cell, this connection might change its firing rate or stimulus tuning. Although this interaction will induce a peak in the cross-correlation, such effects cannot be deduced from purely correlating neural responses. Rather, to quantify the functional impact of lateral inputs on a sensory neuron necessitates a model which explicitly accounts for afferent feedforward inputs and lateral interactions.

To study the impact of a specific lateral interaction, I simultaneously recorded from two heterolateral tangential cells located in the left and right lobula plate: The left Vi and the right H1 neuron. Since both neurons are located in opposite brain hemispheres they receive independent afferent feedforward inputs from their corresponding ipsilateral eye. Moreover, they have different, largely non-overlapping receptive fields. First, I estimated the functional connectivity describing the strength and temporal dynamics of the inter-hemispheric coupling. I then studied to what extent the lateral connectivity improves the optic-flow encoding and tried to unravel the factors that determine the strength of the coupling. To this end, a generative model (generalized linear model, GLM) was fitted to the neural responses which explicitly includes the effects of feedforward input and lateral connectivity (Gerwinn et al., 2010; Okatan et al., 2005; Paninski et al., 2007; Pillow et al.,

2008). Based on the GLM, I estimated the impact of H1 on Vi's rotation tuning and encoding.

### 3.3.1 A Generative Spiking Model for Vi and H1

To investigate the functional role of a lateral interaction between two neurons, I simultaneously recorded from the left Vi cell with its dendrite located in the left lobula plate and the right H1 cell with its dendrite in the right lobula plate. All recordings were performed in the fly *Lucilia sericata*. Figures 3.13A and 3.13B show the spatial receptive fields of Vi and H1 depicted as vector fields. Both cells only exhibit strong responses to motion on their ipsilateral side, except for the small binocular overlap area in the frontal part of the receptive fields (Beersma et al., 1977). Nevertheless, the simultaneously recorded spontaneous activity of Vi and H1 is clearly correlated: Given a spike fired by H1, Vi's firing rate is increased by a factor of about three with a delay of 3 ms (Figure 3.13C). This lag in the response cross-correlation indicates, that H1 projects to Vi. The neural connectivity underlying this correlation as known from previous experiments is depicted in Figure 3.13D: Vi is electrically coupled to the caudal VS cells (VS7-VS10), which are connected via electrical synapses to the CH cell (Haag and Borst, 2007). CH receives excitatory input from the contralateral H1 neuron (Haag and Borst, 2003). The interaction partners of Vi in the contralateral lobula plate are unknown. The indirect, lateral interaction between Vi and H1 is clearly detectable in their cross-correlation, however it is too weak to be visible in the receptive field of Vi. Hence, it is questionable to what extent the lateral input from H1 might affect the stimulus processing in Vi at all.

To study the functional impact of this weak inter-hemispheric interaction between Vi and H1 and to unravel potential factors constraining the strength of the coupling, I presented a random rotation stimulus. This stimulus mimics what a fly would see if it randomly rotated around in a big, black sphere painted with a regular grid of white dots (see Figure 3.14A). To generate the random rotation stimulus, I placed a virtual fly in the center of the large sphere. At each time point, this virtual fly rotated around a steadily changing rotation axis whose x-, y- and z-component are given by independent white-noise profiles (see Figure 3.14A, right). For each time point, the image seen by the virtual fly was projected onto the stimulus device which was faced by a real, fixed fly. The coordinate system was such arranged that the x-axis aligns with Vi's preferred rotation axis, whereas H1's preferred axis is a linear combination of the x- and z-axis. To test whether the stimulus strength influences the interaction between Vi and H1, I compared two stimulus conditions: Strong stimulation where the sphere is painted with a dense grid of dots and weak stimulation with

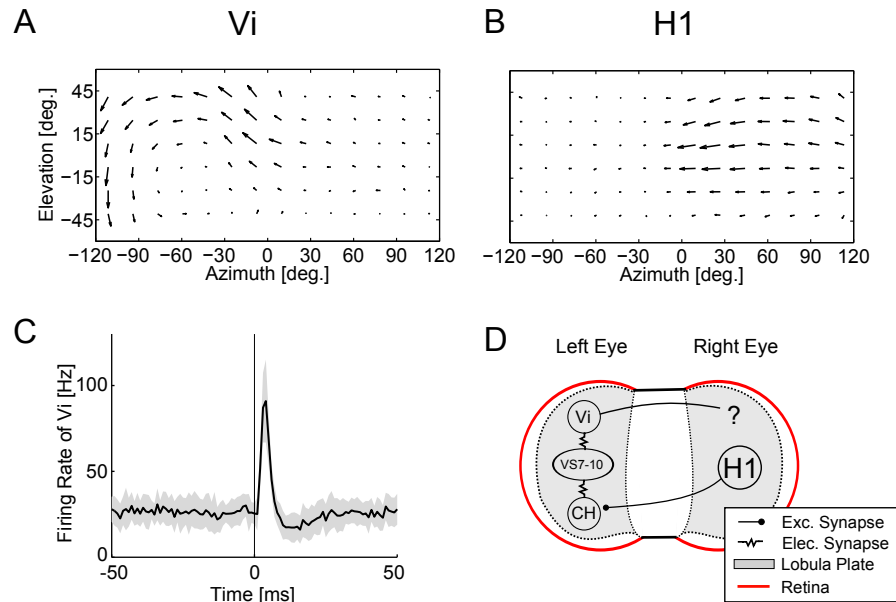


**Figure 3.13: The Responses of the Left Vi and Right H1 Cell Are Correlated.** (A) Spatial receptive fields of a left Vi cell with its dendrite located in the left lobula plate. The direction and length of each arrow indicate the local preferred direction and motion sensitivity. (B) Spatial receptive field of a right H1 cell. (C) Cross-correlation of Vi and H1 for spontaneous activity ( $n=8$  flies). The correlation function depicts the firing rate of Vi relative to the time of a spike fired by H1. The gray shading shows the standard deviation over flies. (D) Physical connectivity of the two heterolateral neurons Vi and H1 as revealed through intracellular double-recordings: The right H1 projects with its axon to the left lobula plate where it is connected to CH via an excitatory, chemical synapse. CH is electrically coupled to VS7-VS10 which form electrical synapses with the left Vi cell (Haag and Borst, 2007). The targets of left Vi in the contralateral lobula plate are still unknown.

a sparse density of dots. To exclude correlations due to shared input from the binocular overlap area, I blanked the frontal region of the stimulus device. Figures 3.14C and 3.14D show both conditions along with example responses of the simultaneously recorded left Vi and right H1 neuron.

The random rotation stimulus allows determining the rotation tuning for both neurons. Given the neural response delay, I calculated for each rotation axis, specified by its azimuth and elevation angle, the mean firing rate. Note that this way, the velocity dependence of the neurons is averaged out. Figure 3.14 shows the resulting two-dimensional tuning maps for Vi and H1 represented as color-coded planar projection of a sphere. As expected from the stimulus arrangement, Vi elicits strongest responses for rotations around the x-axis, whereas H1's preferred rotation axis is clearly shifted towards the z-axis. The tuning maps for Vi and H1 overlap: Rotations around axes located in the frontal region of the southern

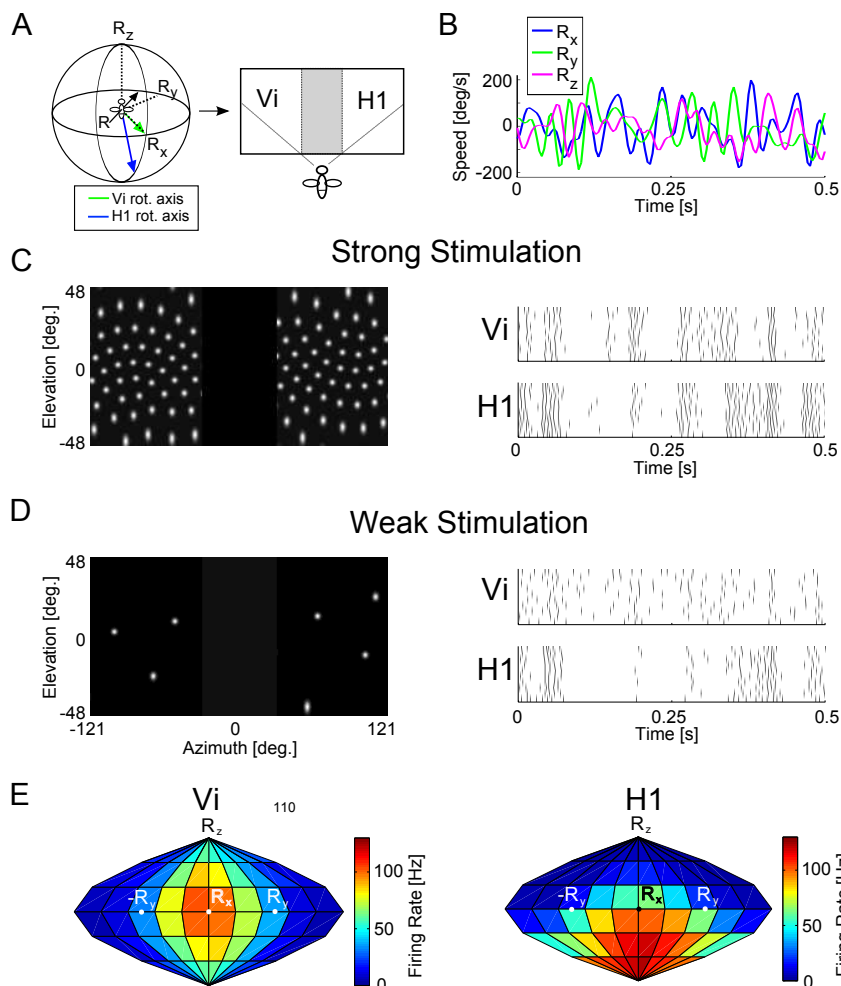


**Figure 3.14: Random Rotation Stimulus.** (A) Scheme illustrating the generation of the random rotation stimulus. (Left) A virtual fly rotates within a large sphere around a steadily changing rotation axis  $\mathbf{R}$ . The coordinate system to describe  $\mathbf{R}$  was such arranged that the x-axis aligns with Vi's preferred rotation axis. H1's preferred axis is a combination of the x- and z-axis. For all time points, I calculated the projection of the sphere onto the virtual fly's eye. The resulting movie was then displayed on the stimulus device which was presented to a (real) fixed fly. (Right) Vi's receptive field is mainly restricted to the left half of the stimulus device, whereas H1 is stimulated via the right half. To avoid correlations induced by overlapping receptive fields, the frontal binocular field was blanked (indicated by the gray shading). The mask ranged from  $-30^\circ$  to  $30^\circ$  along the azimuth. (B) Rotation velocities around the x-, y-, and z-axis as a function of time. At each time point the three-dimensional rotation axis is specified by an x-, y-, and z-component describing the rotation velocity around the x-, y-, and z-axis denoted by  $R_x$ ,  $R_y$ , and  $R_z$ . (C,D) A single frame of the strong and weak stimulus along with responses of a simultaneously recorded left Vi and right H1 cell. The repeated responses to a 0.5 s stimulus segment are represented as raster plots with each black tick representing the appearance of a spike. Spike trains were binned in 1 ms. (E) Rotation tuning of Vi and H1.

hemisphere excite both neurons, i.e. Vi and H1 are stimulus correlated for rotations. This implies that the lateral input from H1 to Vi should shift Vi's tuning towards H1's preferred axis.

To functionally describe the strength and dynamics of the connectivity between Vi and H1, I fitted a generative model which explicitly includes the effects of afferent feedforward input from local motion detectors and potential lateral interactions on a neuron's firing rate. Figure 3.15 shows the generative model, which comprises two stages: At the first stage, the visual stimulus is fed through an array of vertically and horizontally tuned local motion detectors modeled by Reichardt detectors, an established algorithmic model for local motion detection in the fly (Reichardt, 1961; Borst et al., 2010). The outputs of the detector array are projected onto the receptive field of Vi or H1, yielding a one-dimensional time signal. This signal is used as stimulus input for a generalized linear model (GLM) (Gerwinn et al., 2010; Okatan et al., 2005; Paninski et al., 2007; Pillow et al., 2008), the second stage of the applied neuron model (see Methods 2.5.7. In the GLM, Vi's or H1's firing rate is modeled by three linear filters: A stimulus filter describing the impact of the feedforward input on Vi's firing rate, a post-spike filter describing the effect of each spike fired by the neuron on its own firing rate, and a coupling filter capturing the dependency of Vi (H1) on a spike fired by H1 (Vi). To match the neuron's firing rate, an additional constant offset parameter is introduced. The summed filter responses are fed through an exponential nonlinearity yielding the neuron's firing rate. Assuming an exponential function for the neuron's spiking nonlinearity, the exponentiated outputs of the coupling and post-spike filter can be interpreted as multiplying the cell's firing rate. All unknown components of the GLM (drawn in red in Figure 3.15A) were directly fit to the data by maximizing the likelihood of the recorded spike trains under the model. To ensure that the coupling filter describes an existing lateral interaction between Vi and H1 and does not reflect shared noise, common input, or stimulus correlations, I applied the following approach: First, as previously described, I blanked the binocular overlap region and second, the GLMs were trained using uncorrelated random rotation stimuli: I presented on the left and right side of our stimulus device two independent rotation stimuli such that the inputs provided from the left and right eye to the left Vi and the right H1 cell are uncorrelated (see Methods 2.5.7). The GLMs for spontaneous activity, strong and weak stimulation reproduce the observed response correlations with their characteristic sharp peak at 3 ms (see Figures 3.15B-D).

Figure 3.16A shows the stimulus filters estimated for strong and weak stimulation. Note that during weak stimulation for both Vi and H1 the amplitude (gain) is increased by a factor of about 10. Previous studies found that the tangential cells' input conductance

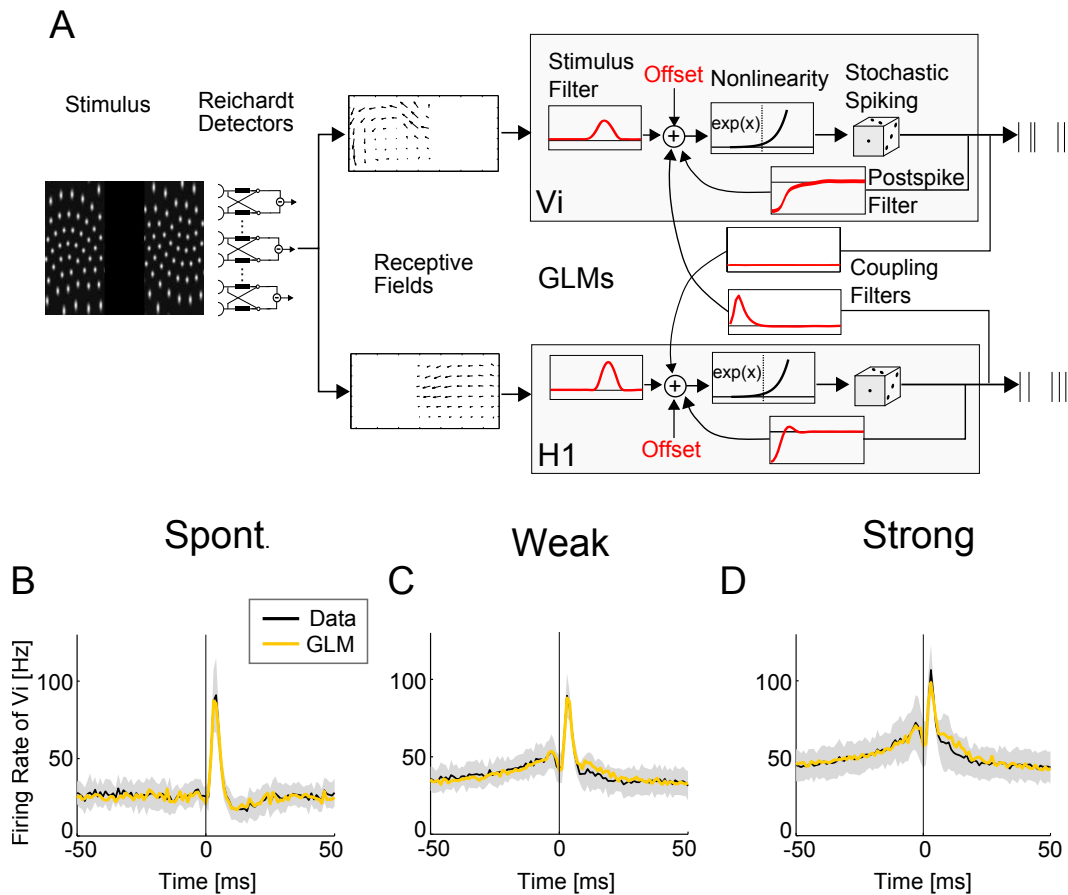


**Figure 3.15: Generative Model for Fly Tangential Cells.** (A) Generative Model for the left  $V_i$  and right  $H1$  cell. The visual stimulus is first fed through a two-dimensional array of Reichardt detectors. The outputs of the motion detectors are then filtered with the spatial receptive field of  $V_i$  or  $H1$  yielding the input signal to a generalized linear model (GLM). The receptive fields were previously determined in a different set of experiments. The weights on the contralateral side were set to zero. The components of the GLM are depicted in the gray shaded area. In the GLM,  $V_i$ 's or  $H1$ 's firing rate is modeled via three linear filters: The stimulus filter describing the impact of the stimulus on the cell's firing rate, a post-spike filter accounting for the spiking dynamics and a coupling filter describing the cell's dependence on a second neuron. The summed filter outputs are fed through an exponential nonlinearity yielding the instantaneous firing rate. (B,C,D) The measured (black) and predicted (orange) cross-correlations between  $V_i$  and  $H1$  (black) for spontaneous activity as well as weak and strong stimulation. Each cross-correlation shows the firing rate of  $V_i$  relative to the time of a spike fired by  $H1$ . The measured and predicted correlations were averaged over all flies ( $n=8$ ). For the data, the standard deviation is depicted as gray shading.

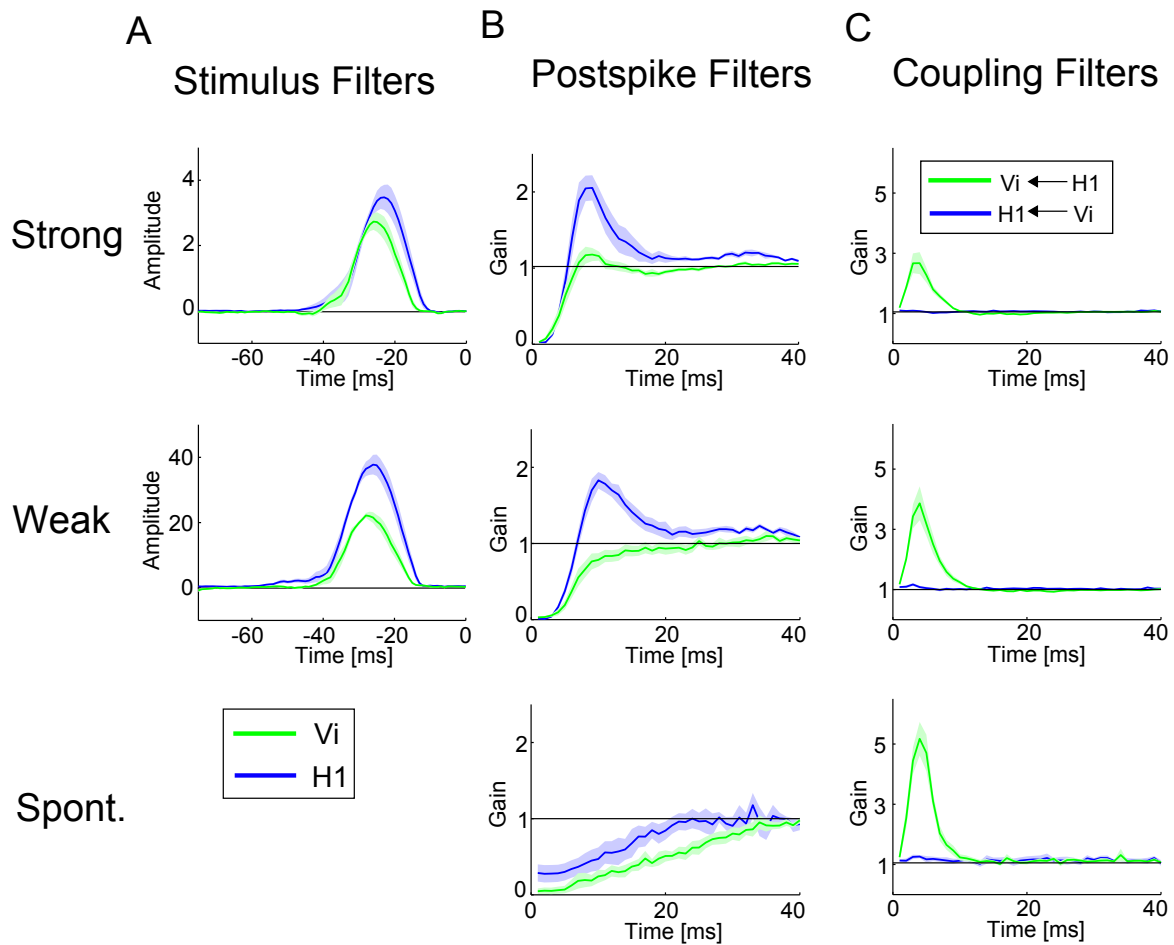


**Figure 3.16: Generalized Linear Model Components.** (A) Stimulus filters of Vi (green) and H1 (blue) for strong and weak stimulation. Note that for weak stimulation the stimulus filter amplitude (gain) is about ten-fold larger than for strong stimulation (different y-axes). The solid lines indicate the average over flies, the green and blue shadings depict the standard deviations for Vi and H1. (B) Post-spike filters for strong and weak stimulation as well as spontaneous activity. The post-spike filters were exponentiated such that the y-axis shows the factor (gain) by which the neuron’s firing rate is multiplied. (C) Coupling filters for all conditions. The coupling filter describing H1’s impact on Vi is shown in green, whereas the filter connecting Vi to H1 is depicted in blue. The coupling filters are exponentiated such that they can be interpreted as multiplying the neuron’s firing rate.

underlies a biophysical gain control mechanism: With increasing stimulus strength the input conductance is enhanced and, consequently, the impact of single pre-synaptic motion detectors on the neuron’s firing rate is reduced (Borst et al., 1995; Weber et al., 2010). The post-spike filters are shown in Figure 3.16B. In this representation, the filters are exponentiated such that they can be interpreted as multiplying the neuron’s firing rate. The filters of both neurons exhibit for all conditions an inhibitory period following a spike. After this refractory period, H1 shows for strong and weak stimulation a facilitatory period increasing the likelihood for spike initiation (see Figure 3.16B).

The coupling filters for strong and weak stimulation as well as spontaneous activity are depicted in Figure 3.16C. For all conditions the filter describing the impact of  $V_i$  onto H1 is always one, i.e.  $V_i$  has no effect on H1. Contrarily, the coupling filter capturing  $V_i$ ’s dependence on H1 clearly peaks at 3 ms, i.e. H1 has an excitatory effect on  $V_i$ : A spike fired by H1 excites  $V_i$  with a delay of 3 ms. The influence of H1 then decays to zero within the next 7 ms. Directly following a spike by H1, the amplitude of  $V_i$ ’s coupling filters are close to one for all stimulus conditions. This strongly indicates that the coupling filters do not reflect common input to  $V_i$  and H1, but an existent physical connection from H1 to  $V_i$ . While the shape of the coupling filters connecting H1 to  $V_i$  is unaffected by the stimulus strength, their amplitude is significantly reduced with increasing stimulation. Hence, the coupling filters strongly suggest a uni-directional coupling from H1 to  $V_i$ , with the coupling strength depending on the stimulus strength.

### 3.3.2 H1 Improves the Optic-Flow Representation in $V_i$

Next, the GLM was used to test to what extent  $V_i$ ’s tuning properties depend on the input from H1. To do so, I first generated spike trains by the GLM for strong and weak stimulation. Since the coupling between H1 and  $V_i$  is only uni-directional and not reciprocal, it was not necessary to simulate the activity of both neurons at once. To predict  $V_i$ ’s spiking, I therefore replaced the GLM for H1 by the corresponding recorded H1 spikes to limit the number of model parameters. Simulating only  $V_i$ , it can be excluded that any predictions on  $V_i$ ’s tuning properties are due to potential biases in H1’s GLM. Based on the simulated spike trains, I then calculated rotation tuning maps for the model  $V_i$  cell as done for the recorded data in Figure 3.14E (left). For simplicity, I then averaged the tuning maps along elevation and azimuth to obtain a one-dimensional azimuth and elevation tuning depicted in Figure 3.17A for strong stimulation (dark red lines) and in Figure 3.17B for weak stimulation (dark blue lines) averaged over the GLMs for all flies. To estimate H1’s impact on  $V_i$ ’s tuning curves, I canceled the coupling filter connecting

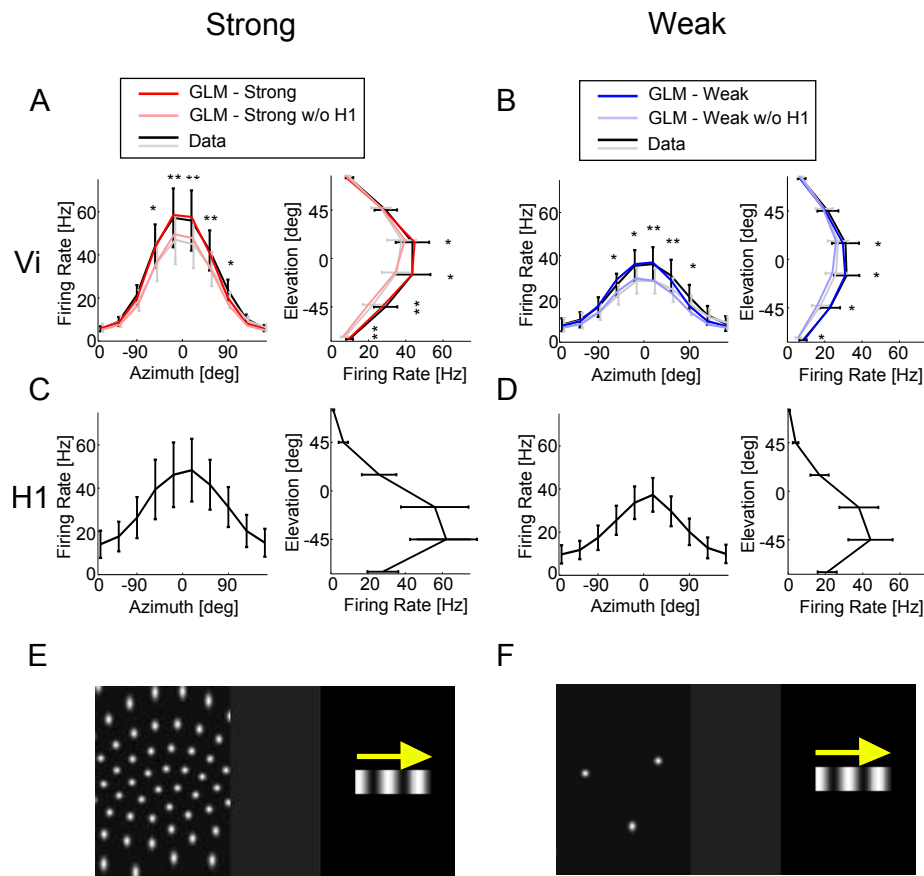


**Figure 3.17: H1 Enhances the Amplitude of Vi's Rotation Tuning.** (A) Averaged azimuth and elevation tuning of Vi for strong stimulation. The tunings predicted by the GLM before and after ablating H1 in the model are depicted in dark and pale red. Without input from H1, the amplitude of the rotation tuning is reduced. The azimuth and elevation tuning were calculated from tuning maps as depicted in Figure 3.14E through averaging along the elevation and azimuth. To estimate the tuning for a single fly, only Vi was simulated by the GLM, whereas for H1 the recorded spikes were used. The averaged tuning curves for the recorded data are shown in black. The gray represent the tunings for unilateral stimulation depicted in (E,F). The errors bars denote the standard deviation over flies ( $n=8$ ). Significant differences in the measured tuning curves (based on a paired t test) are indicated by asterisks ( $*p < 0.01$ ,  $**p < 0.001$ ). (B) Averaged azimuth and elevation tuning of Vi predicted by the GLM for weak stimulation before (dark blue) and after ablating H1 in the model (pale blue). The measured tuning curves are shown in black and gray. (C, D) Measured azimuth and elevation tuning of H1 for strong and weak stimulation (error bars denote the standard deviation). Since H1 is sensitive to rotations around the z-axis its elevation tuning is shifted towards negative elevation angles. (E,F) Unilateral stimulation of Vi. To deplete the input from H1 to Vi during strong and weak stimulation, the right side of the stimulus device (H1's ipsilateral side) was blanked. To further reduce H1's remaining activity a small grating moving in H1's null direction was presented.

H1 to Vi and then re-simulated the spike trains by the GLM. The resulting tuning curves are shown in pale red and pale blue in Figures 3.17A and 3.17B.

Next, I tested whether these predictions by the GLM can be experimentally verified. To this end, the random rotation stimulus was presented only on the left side of visual space, while the complete right half corresponding to H1's ipsilateral side was blanked. To further decrease H1's remaining activity during this unilateral stimulation, I presented a small grating moving in H1's null direction, strongly reducing H1's firing (see Figure 3.18A). To exclude that this small grating excites cells which then inhibit Vi, the activity of Vi was recorded when only presenting this grating. As can be seen in Figure 3.18B the grating only had a weak excitatory, but no inhibitory effect on Vi. Figures 3.17A and 3.17B demonstrate that the model predictions and measured tunings (black and gray) closely overlap for strong and weak stimulation.

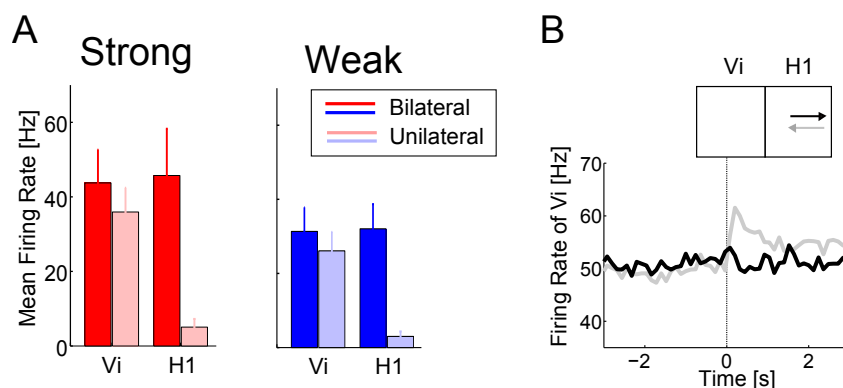


**Figure 3.18: Control Experiments.** (A) Mean firing rates of Vi and H1 during strong and weak stimulation. The results for bilateral stimulation are drawn in dark red and dark blue. Unilateral stimulation decreases Vi's firing rate (pale red and pale blue), whereas H1 is nearly silenced. (B) To inhibit H1 during unilateral stimulation of Vi (see Figures 5E and 5F), we presented a small sine grating on the right half of the stimulation screen. To exclude that this grating inhibits Vi, we recorded Vi's activity, while only presenting the sine grating at the same position as in Figures 5E and 5F. The upper scheme illustrates the stimulus device and indicates by the arrows the motion direction of the grating. To maximally increase Vi's spontaneous activity, the area outside the sine grating was constantly fully illuminated. If the sine grating moved in H1's preferred direction (indicated by the gray arrow), Vi's activity was slightly increased as expected from the uni-directional, excitatory coupling revealed by the GLM (gray solid line). Contrarily, if the grating moved in H1's null direction (black arrow), Vi's firing rate is unaffected (black solid line). Hence, the grating does not inhibit Vi. The grating started moving at time point 0 at a constant temporal frequency of 1.5 Hz ( $n=7$  flies).

Note that presenting no stimulus on the right side might also diminish the influence of further potential interaction partners of Vi from the right lobula plate. Hence, the finding

that the data reproduces the model predictions strongly suggests that for the presented stimuli and the stimulated regions H1 is Vi's main interaction partner from the contralateral lobula plate.

Generally, the input from H1 increases the amplitude of Vi's azimuth and elevation tuning. For comparison, Figures 3.17C and 3.17D show H1's azimuth and elevation tuning for strong and weak stimulation. For both conditions, Vi and H1 exhibit a similar azimuth tuning. Hence, an input from H1 should not shift Vi's azimuth tuning as can be seen for the predicted and measured tuning curves. However, compared to Vi, H1's elevation tuning is shifted towards negative angles, since H1 is also sensitive to rotations around the z-axis. Consequently, an excitation from H1 should shift Vi's elevation tuning. Indeed, the recorded and measured tuning curves show an asymmetric shift due to the input from H1: For elevation angles smaller than  $40^\circ$ , the firing rates for bilateral stimulation are slightly increased (see the asterisks), while for positive angles ( $>40^\circ$ ), the tuning curves closely overlap. However, though significant, this effect is only very small. Hence, although H1 exhibits a different elevation tuning, its input to Vi increases the amplitude of Vi's tuning curves without affecting Vi's rotation preference.

For the model predictions, H1's input to Vi was completely depleted in GLM, whereas in the recordings, H1 still showed a small firing rate of about 5 and 3 Hz (see Figure S2A). To test whether this residual activity might affect the model predictions presented in Figures 3.17A and 3.17B, I simulated Vi given H1's spike trains recorded during unilateral stimulation, instead of depleting the coupling. However, the resulting tuning curves predicted by the GLM are unchanged, strongly suggesting that H1's residual activity has no impact on Vi (data not shown).

To quantify the functional impact of H1 on Vi, I tested how well the self-motion profile is represented by the spikes fired by Vi depending on the input from H1. To measure the stimulus representation by Vi, I tested how well the x-, y-, or z-profile of the random rotation axes can be reconstructed by a linear filter from the recorded (or simulated) spikes of Vi (see Figure 3.19A). Comparison of the power spectra of the stimulus and the reconstruction gives a lower bound on the information carried by the spikes (see Methods 2.5.9). First, I tested whether the spike trains generated by the GLM as directly fit from the data are as informative as the recorded spikes. The x-profile corresponding to Vi's preferred rotation axis was chosen as stimulus. As shown in Figure 3.19B, the GLM under-estimates the information carried by the spikes. This is likely due to the fact that the stimulus input to the GLM is itself only an estimate of the real unknown input to Vi. I found that in case that the real input can only be approximated the amplitude of the stimulus filter will be under-estimated by the GLM (see Figure S3). To compensate for this bias,

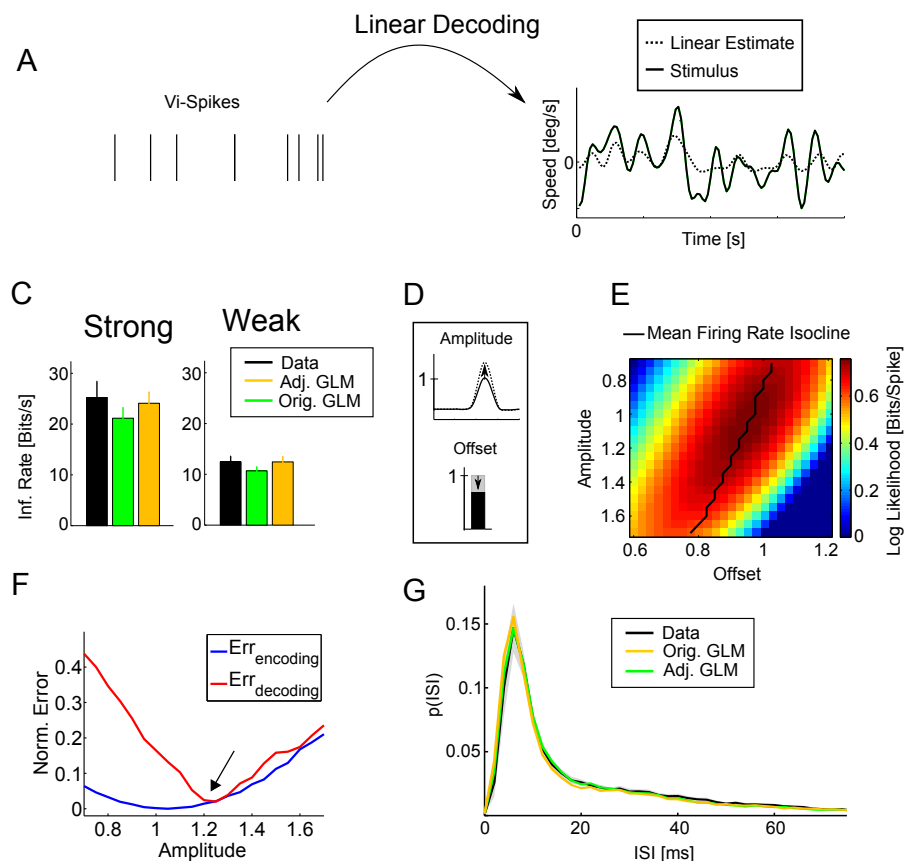


**Figure 3.19: Adjusting the GLM's Stimulus Amplitude.** (A) Optimal Linear Decoding. To quantify the stimulus encoding by Vi, I tested how well the x-, y-, or z-rotation velocity (stimulus) can be reconstructed from the spike trains using a linear filter. (B) The optimal encoding model (Orig. GLM, green) underestimates the information carried by the recorded spikes of Vi (Data, black) about x-rotations. Adjusting the GLM's amplitude allows compensating for this bias (Adj. GLM). (C) Scheme illustrating the adjustment of the GLM. To compensate for the under-estimated decoding performance by the GLM, the amplitude of the stimulus filter was increased. To match the mean firing rate, the offset parameter was reduced. (D) Averaged log-likelihood of Vi (measured in Bits/Spike) for strong stimulation as function of the stimulus filter amplitude and the offset parameter. For both parameters, the factor by which the amplitude or offset of the original GLM was changed is depicted on the x- or y-axis. All models which preserve the measured mean firing rate lie on the black line (Mean Firing Rate Isocline). (E) Encoding and decoding error in dependence of the stimulus filter amplitude (for strong stimulation). The blue curve shows the averaged percentage deviation from the log-likelihood maximum along the mean firing rate isocline in (D). The red curve quantifies the percentage by which the information (measured in Bits/Spike) of the simulated spikes deviates from the information carried by the recorded spikes. As new stimulus filter amplitude, I chose the value that minimizes the sum of both errors (indicated by the arrow). The x-axis depicts again the factor by which the filter amplitude was changed. (F) Comparison of the inter-spike interval distribution of the recorded spikes (black) with the distributions of the spikes predicted by the original (green) and adjusted GLM (orange). The gray shading depicts the S.E.M. for the recorded spikes.

the amplitude of the stimulus filter was slightly increased. To determine how strongly the amplitude has to be changed, I first calculated the log-likelihood of the GLM (for strong or weak stimulation) as a function of the stimulus filter amplitude and the offset parameter to compensate for changes in the mean firing rate (see Figure 3.19C). Since the log-likelihood function is rather flat (Figure 3.19D), I asked whether a model whose likelihood deviates slightly from the maximum might perform better in decoding. To find such a model, I first determined all models which preserve the measured mean firing rate. These models lie on the black line depicted in Figure 3.19D. I then plotted two errors as function of the stimulus filter amplitude along this line: An encoding error measuring the (percentage) deviation from the log-likelihood maximum and a decoding error quantifying how much the decoding performance of the predicted spikes deviates from the information of the recorded spikes. Both error functions are depicted in Figure 3.19E. I chose as new filter amplitude the value minimizing the sum of both errors. As shown in Figure 3.19B (orange), with this correction, the spikes of the resulting GLM are as informative as the recorded ones. Figure 3.19F compares the inter-spike interval distribution of the recorded spikes with the distributions of the spikes predicted by the original and adjusted GLM. Although adjusting the amplitude slightly increased the peak of the interval distribution at 8 ms, all three curves still closely overlap. Hence, the correction only slightly affects the predicted responses. After adjusting the stimulus filter amplitude, the GLM still reproduces the cross-correlation of Vi and H1. The predicted correlations shown in Figures 3.15B-D were calculated using the adjusted GLM.

Finally, I estimated how the stimulus reconstruction by Vi depends on the strength of the coupling between Vi and H1. Vi's spikes carry only information about rotations around its preferred rotation axis corresponding to the x-axis (Figure 3.20A, green). Since H1 carries information about the x-axis (see Figure 3.20A, blue), coupling H1 to Vi should improve Vi's stimulus representation. However, on the time, H1 also provides information about the z-axis, which might impair Vi's encoding of the x-axis and affect its rotation tuning. To test this intuition, the coupling strength between Vi and H1 was varied over a large range of values. In the GLM, the coupling strength was controlled by varying the amplitude of the coupling filter connecting H1 to Vi (see Figure 3.20B).

Figures 3.20C-E show the information carried by Vi about the x-, y-, and z-axis as function of the coupling strength. Here, the coupling strength indicates the factor by which the amplitude of the coupling filter was increased or decreased, i.e. 1 corresponds to the measured strength, whereas for 0 the coupling is ablated. Experimentally, this case was measured using the unilateral stimulus presented in Figures 3.17E and 3.17F. As shown in Figure 3.20C increasing the coupling strength from 0 ('no coupling') to 1 ('coupling as

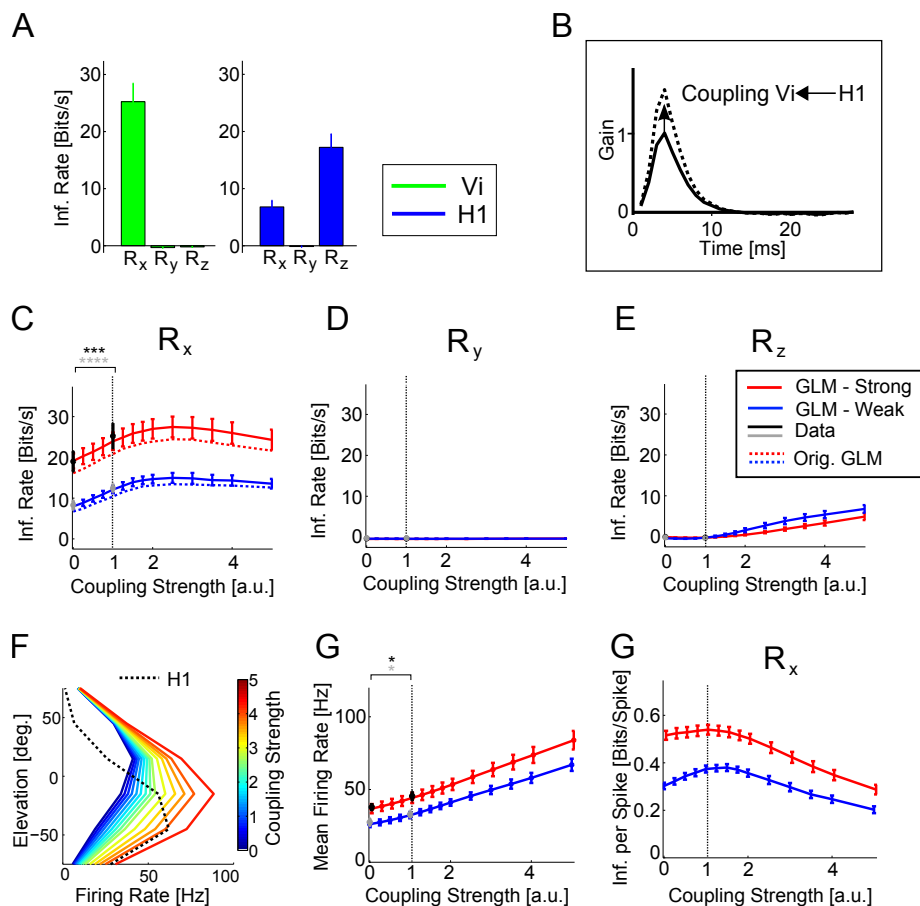


**Figure 3.20: The Coupling Improves Vi's Stimulus Representation.** (A) Averaged information encoded by Vi (green) and H1 (blue) about the x-, y-, and z-rotation velocity for strong (left) and weak stimulation (right). (B) To vary the coupling strength, I changed the amplitude of the (non-exponentiated) coupling filter describing H1's impact on Vi. (C) Information carried by Vi about x-rotations. The averaged information during strong and weak stimulation as estimated by the GLM is shown in blue and red. The x-axis indicates the factor by which the coupling filter amplitude was changed. Hence, 1 corresponds to the measured coupling strength, whereas 0 indicates no coupling. The experimentally measured information rates are depicted in black (strong stimulation) and gray (weak stimulation). The data values for a coupling strength of 0 were measured for unilateral stimulation. Error bars denote S.E.M over all flies ( $n=8$ ). Significant differences between the recorded data (based on a paired t test) are indicated by asterisks ( $***p < 0.0001$ ,  $****p < 0.00001$ ). (D) Information carried by Vi about the y-rotation velocity  $R_y$ . (E) Information carried by Vi about the z-rotation velocity  $R_z$ . (F) Predicted elevation tuning of Vi in dependence of the coupling strength. Only for large coupling strengths Vi's tuning is clearly shifted towards H1's elevation tuning (dotted black line). (G) Mean firing rates of Vi in dependence of the coupling strength. The mean firing rates predicted by the GLM are depicted in red (strong stimulation) and blue (weak stimulation). The experimentally measured rates are shown in black and gray. (H) Averaged information per spike estimated by the GLM. For the coupling strength measured in the fly the single spike information is maximal.

measured in the fly'), for both strong (red) and weak (blue) stimulation, the encoding of Vi's preferred rotation axis is significantly improved by 33% and 50%. As indicated by the black (strong) and gray (weak) dots, the information predicted by the GLM for a coupling strength of 0 and 1 could be experimentally verified. Increasing the coupling beyond the strength as found in the fly still increases the information till reaching a maximum at about 2.5 times the measured coupling strength. To test whether the general trend of the information as function of the coupling strength might be influenced by the adjustment of the stimulus filter, I re-calculated the information for the original GLM. As shown by the dotted lines in Figure 3.20C, for strong and weak stimulation the resulting information curves are only shifted downward by a constant offset. Hence, the shape of these curves is not influenced by the adjustment of the stimulus filter amplitude.

As expected from the arrangement of the coordinate system (see Figure 3.14A), Vi has no information about the y-axis irrespective of the coupling strength (Figure Figure 3.20D). As depicted in Figure 3.20E, although H1 provides information about the z-axis, only for large coupling strengths Vi carries information about this axis. However, for weak coupling strengths (from 0 to 1.5) Vi's information about the z-axis is negligible. To test whether this effect is reflected in Vi's rotation tuning, I calculated its elevation tuning in dependence of the coupling strength (Figure 3.20F). Increasing input from H1 is expected to shift Vi's elevation tuning towards negative angles. However, for coupling strengths up to 1.5, Vi's tuning is only slightly affected. Only for strong couplings the tuning is significantly shifted. As shown in Figure 3.20C, although the input from H1 improves Vi's rotation representation, Vi and H1 are clearly not optimally coupled in the fly. However, stronger coupling both neurons leads to increased firing rates (see Figure 3.20G), hence the stimulus encoding becomes energetically more expensive. A way to account for the consumed energy, when measuring the quality of the stimulus reconstruction, is to divide the information rate measured in bits per second by the mean firing rate. The resulting measure quantifies the information carried by a single spike. Interestingly, for both stimulus conditions, the information per spike is maximal for the measured coupling strength. Hence, the coupling strength between the two neurons is adjusted to a value such that the rotation tuning of Vi is nearly unaffected by inputs from H1 and that the information transmission from H1 to Vi is energetically optimal.

To test whether the improved stimulus representation by Vi is indeed due to the information about x-rotations provided by H1, the same analysis as presented in Figure 3.20 was applied to the uncorrelated stimulus condition, where independent (uncorrelated) rotations were presented to Vi and H1. If the input provided by H1 is uncorrelated to Vi's activity, it might be interpreted as additional noise source potentially impairing Vi's stimulus processing.

Since the connection is purely excitatory, Vi's firing rate is enhanced by inputs from H1 with increasing coupling strength (see Figure 3.21B). However, as expected, the information per spike is reduced when increasing the coupling between Vi and H1 (see Figure 3.21C). Since for small coupling strengths, the firing rate increases faster than the information per spike is reduced, the information rate is slightly increased (see Figure 3.21B). However, for strong couplings, also the information rate is clearly deteriorated. These findings demonstrate that the improved stimulus processing by Vi relies on the fact that Vi and H1 are stimulus correlated due to their shared sensitivity to x-rotations.

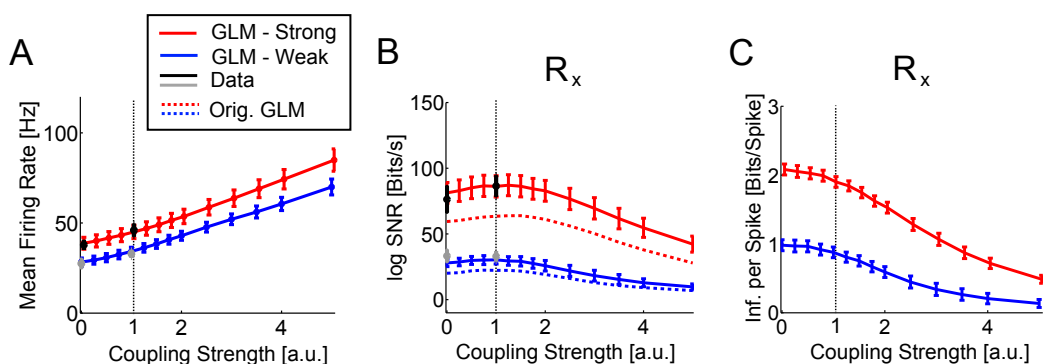


**Figure 3.21: Rotation Encoding by Vi for Uncorrelated Stimulation of Vi and H1.** (A) Mean firing rates of Vi in dependence of the coupling strength when uncorrelated rotation stimuli were presented on the left and right side of visual space (Red - Strong Stimulation; blue - Weak Stimulation). The measured values are shown in black and gray. Error bars denote the S.E.M. (C) Information of Vi about  $R_x$  during uncorrelated stimulation. The measured values are shown in black and gray. (B) Information per spike carried by Vi about  $R_x$  during uncorrelated stimulation. With increasing coupling strength the information per spike is reduced.

In the presented project, I characterized the functional connectivity of two heterolateral neurons (left Vi and right H1) located in the left and right lobula plate and tested the impact of their inter-hemispheric coupling on the encoding of optic-flow. To characterize the coupling of these neurons, I simultaneously recorded their spiking during presentation of random rotation stimuli and fitted a generalized linear model (GLM) to their responses. To exclude that the estimated coupling reflects common stimulus input due to overlapping receptive fields, the frontal binocular field was blanked such that both eyes were independently stimulated and, consequently, both neuron received independent feedforward inputs. The GLM reproduces the measured response correlations of Vi and H1. The coupling filters of the GLM strongly suggest an excitatory, uni-directional coupling from H1 to Vi, with the coupling strength depending on the stimulation strength. Ablating H1 in the GLM reduced the amplitude of Vi's rotation tuning. These predictions were verified

by stimulating only  $V_i$ , while  $H1$ 's activity was reduced by a small grating moving in its null direction. Next, I tested the dependence of  $V_i$ 's stimulus representation on the input from  $H1$ . It was found that the coupling increases the information carried by the spikes by 33% and 50% for strong and weak stimulation. Further investigation of the GLM revealed potential constraints that might determine the strength of the connection: First, the coupling strength is adjusted to a value such that the information per spike is maximal, i.e.  $V_i$  and  $H1$  are coupled in an energetically efficient way. Second, the coupling is still weak enough such that the  $V_i$ 's rotation tuning is nearly unaffected by the input from  $H1$ . This effect relies on two factors:  $V_i$  and  $H1$  are stimulus correlated and the coupling is weak such that uncorrelated input from  $H1$  does not significantly affect  $V_i$ 's stimulus encoding. Hence, simulating neurons with a generative model, whose components are directly fit to the data, allows analyzing the functional impact of lateral interactions which might not be expressed in the receptive field.



# Chapter 4

## Discussion

In this thesis, I functionally characterized the encoding of optic-flow by the lobula plate tangential cells. To this end, I pursued a system identification approach with the aim to describe the stimulus processing by the tangential cells by means of compact, easily interpretable single cell or two-cell models. A standard model to characterize sensory neurons is the linear-nonlinear (LN) model consisting of a linear receptive field followed by a static nonlinearity.

First, I described the spatio-temporal processing properties of the tangential cells by an LN-model. To estimate the components of the LN-model, I presented novel random motion stimuli comprising randomly moving dots (Brownian motion stimulus). The receptive field of an optic-flow processing neuron can be represented as a time-varying vector field (referred to as dynamic receptive field) describing how the preferred optic-flow pattern evolves through time. I found that the dynamic receptive fields of the tangential cells can be separated into a single spatial (vector field) and temporal component (one-dimensional temporal filter). When increasing the stimulus strength (through an increased density of moving dots), the gain and selectivity of the tangential cells is strongly reduced. To account for these modulations of the nonlinearity, I included explicit biophysical elements to the LN-model. The resulting model captures the gain and selectivity modulations by the stimulus strength and, thus, generalizes the LN-model.

The dynamic receptive field describes, what optic-flow pattern induces strongest responses, and therefore allows predicting which self-motion a specific tangential cell encodes. However, the receptive field does not permit to conclude how well the tangential cells act as self-motion sensors when confronted with more naturalistic stimuli and changing environments. To probe the self-motion encoding by the tangential cells, I presented dynamic rotational and translational self-motions in varying environments. To characterize the self-

motion processing, I fitted LN-models transforming the presented self-motion profile to the recorded firing rates. Especially, the linear filters describing the processing of rotations are stable across environments. However, the gain (steepness of the nonlinearity) is strongly modulated by the structure of the environment. Generally, rotations are slightly better represented by the neural responses than translations.

The receptive field and, therefore, the self-motion tuning of a tangential cell arises from the integration of the input from pre-synaptic local motion detectors and lateral interaction with further tangential cells. However, classical LN-models do not allow identifying the different origins of the inputs integrated by a cell. To understand how lateral interactions influence the properties of single neurons, I simultaneously recorded from two neurons (left Vi and right H1 cell), while presenting dynamic rotation stimuli. I then fitted to the recorded responses a generalized linear model (GLM). The GLM can be seen as an extension of the LN-model. By including an additional coupling filter, the GLM accounts not only for the stimulus dependence of a neurons firing rate, but also for lateral interactions between neurons. By means of the GLM, I found that H1 is uni-directionally coupled to Vi. This interaction improves the rotation encoding in Vi. The strength of the coupling is adjusted to a value such that the information per spike is maximized in Vi. However, the coupling is still weak enough such that the excitatory input from H1 does not shift Vi's rotation tuning.

## 4.1 Compartmental Modeling and System Identification

In sensory neuroscience, there exist two diametrically opposed approaches to model neurons. The first approach relies on bottom-up models: Based on rich anatomical and physiological data, the goal is to build a detailed biophysical *in silico* model of a single neuron or neural circuits. This is typically done by assembling the three-dimensional structure of a neuron from small cylinders (compartments) (Rall, 1964; Dayan and Abbott, 2001). Each compartment is equipped with a specific set of ion channels, whose dynamics are described by differential equations. Such a compartmental model can then be simulated by solving a large set of differential equations through numerical integration (Carnevale and Hines, 2006). The appeal of this approach is that having a detailed *in silico* model, all kinds of experiments can be carried out, allowing for a complete functional characterization of the input-output relation implemented by a neuron or neural circuit. However, the behavior of a compartmental model depends on an often large number of unknown parameters

which have to be fit to reproduce the physiological data. The corresponding error function is generally highly non-linear with multiple local minima. Hence, it is often unclear whether a given parameter set (although reproducing the physiological data) represents a unique solution (corresponding to the global minimum) or whether there might be more sets which exhibit a similar behavior. The existence of different solutions might severely restrict the generality of a compartmental model and, thus, limits its explanatory power. Hence, in the end, the parameter selection often does not depend on objective criteria as the unique solution of an error function, but rather on the intuition of the modeler.

The system identification approach tries to cope with this problem (Wu et al., 2006) by restricting the number of pre-assumptions on the anatomy, physiology, or structure of neurons or circuits. Top-down models such as LN-models or generalized linear models (GLMs) describe the input-output relationship of a neuron or circuit by a comparably small number of parameters. The unknown model components are fit by minimizing an error function. The appeal of LN-models or GLMs is that the corresponding error function has only one global maximum, thus defining a unique set of optimal parameters (Dayan and Abbott, 2001; Paninski et al., 2007). However, such top-down models are purely phenomenological: Although, providing a description of the neural input-output relationship, it is in most cases not possible to relate its components to physiological properties. E.g. changes in the neural gain or the coupling strength between neurons are captured by changes in the models components, however, how these changes are caused by the underlying biophysics often remains unclear.

A general aim of this thesis was to make the components of top-down models interpretable: To relate functional phenomena as the gain or selectivity to the physiological properties of a neuron, I extended the LN-model by explicitly including biophysical elements. The parameters of the resulting model can be still directly fit to the data by (automatically) minimizing an error function. This allowed me to relate modulations in the gain and selectivity of the fly tangential cells to changes in their input conductance and unbalanced excitatory and inhibitory driving forces (see Section 3.1).

Generalized linear models have been successfully applied to describe the functional connectivity of neural populations in the retina or cortex. However, the coupling filters which describe the lateral interactions between neurons do not necessarily correspond to existent synaptic connections (Shlens et al., 2006; Pillow et al., 2008). Instead, they might reflect shared input to a pair of neurons, shared noise, or overlapping receptive fields. To guarantee that the coupling filter between H1 and Vi describes the lateral interaction of these two neurons, I carefully adjusted the presented stimulus: First, the region in visual space where the receptive fields of Vi and H1 overlap was blanked. Second, to train the GLM, I

presented uncorrelated stimuli to Vi and H1 (see Section 3.3).

A goal of future research is to extend the generalized linear model such that it also captures changes in the neural gain and selectivity as the biophysical LN-model as well as changes in the coupling strength between the neurons. Such an approach allows compensating for one of the major flaws of top-down models: their ignorance of biophysical details.

## 4.2 Space-Time Separability of the Dynamic Receptive Fields

As described in Section 3.1, the dynamic receptive fields of the fly tangential cells are fully described by a single temporal and spatial component, i.e. they are space-time separable. This result post-hoc justifies earlier studies which either investigated the spatial lay-out of local preferred direction neglecting dynamic processing features (Krapp and Hengstenberg, 1996; Krapp et al., 1998, 2001), or merely focused on the temporal processing properties of the fly neurons (Safran et al., 2007; Fairhall et al., 2001; Brenner et al., 2000; Borst, 2003). The space-time separability implies that the tangential cells exhibit homogeneous dynamic properties. In contrast, it has been shown that the responses of optic-flow processing neurons in cortical area MST in monkeys arise from the contribution of multiple temporal components (Duffy and Wurtz, 1997): an unspecific followed by a specific response component exhibiting a clear tuning. However, if continuously varying optic-flow patterns are presented, the unspecific component disappears, and the neural responses vary smoothly with the displayed trajectory (Paolini et al., 2000). Similarly, the lobula plate tangential cells of flies also encode the degree to which a given velocity pattern matches the cells' receptive field. Further evidence for such a linear encoding of optic-flow by large-field motion-sensitive neurons has been provided for neurons in the accessory optic system in pigeons (Wylie et al., 1998).

The finding that the spatial and temporal components changed only slightly through an increase of the motion density suggests that the response of the tangential cells depends only weakly on second-order correlations in the stimulus. This is surprising given that each of the recorded neurons is inter-connected via electrical or chemical synapses to other tangential cells (Borst et al., 2010). A possible explanation for this finding might be that incoming synaptic inputs do not nonlinearly interact, but rather sum linearly as might be expected for electrical synapses. Alternatively, synapses connecting tangential cells might act on a very small time scale and affect more the exact timing of spikes than trial-averaged firing rates. Compared to other sensory systems, the fly tangential cells

behave astonishingly linearly: E.g. the visual cortex has been reported to be sensitive to higher-order correlations in visual textures (Purpura et al., 1994). Moreover, natural image statistics has been shown to change the receptive fields of neurons in V1 (David et al., 2004) as well as their gain (Felsen et al., 2005) also indicating that higher-order correlations affect the stimulus processing in visual cortex. Similarly, it has been demonstrated that the response properties of neurons in the auditory cortex are influenced by interactions in the spectrum of the presented auditory stimuli (Ahrens et al., 2008).

### 4.3 LN-Models and Adaptation

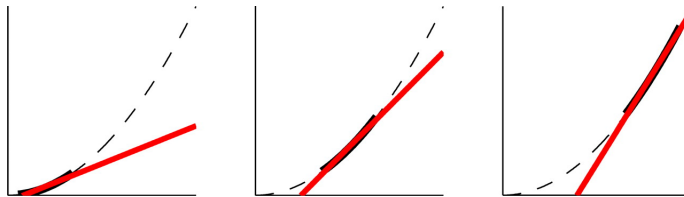


**Figure 4.1:** Three examples for approximating a parabolic function by a straight line. Depending on the sampled region (indicated by the thick black line) linear regression yields different fits (shown in red). Figure taken from Christianson et al. (2008).

Changes in the components of an LN-model, as observed for the input-output relation of the fly tangential cells, are often described as adaptations to changes in the stimulus statistics: It is assumed that a change in the model parameters corresponds to changed (adapted) parameters in the neurons. However, the presence of an adaptation mechanism cannot be necessarily deduced from modulations of the LN-model components by the presented stimulus ensembles. The input-output relation of neurons is typically highly nonlinear. As illustrated in Figure 4.1, sampling e.g. a quadratic nonlinearity in different regions by changing the stimulus statistics yields different linear approximations (Christianson et al., 2008). In such a case, the change in the LN-model is not caused by an adaptive mechanism which accumulates evidence about changes in the external world on a timescale governed by the stimulus statistics; rather, the input-output relation appears to be changed simply because the neuron responds differently to various stimulus ensembles due to its inherent nonlinearity. Notably, such changes happen instantaneously and do not depend on the stimulus statistics. However, explicitly modeling the involved nonlinearity should then correct for changes in the LN-model components (Borst et al., 2005; Wark et al., 2007; Ahrens et al., 2008). Indeed, I found that extension of the LN-model by a further nonlinear

term modeling the biophysics of dendritic integration accounts for the divisive and additive modulation of the input-output relation of the tangential cell by the density of presented dots (see Section 3.1). Explicitly modeling dendritic integration generalizes the resulting model, such that it can be applied to data sets of varying motion density, without the need to adjust its gain or selectivity. This finding suggests that for the presented stimuli no strong adaptation process is at work and that all changes in the input-output relation happen instantaneously. Hence, explicitly modeling excitatory and inhibitory input lines and subsequent dendritic integration in a finite cable might also allow for other sensory systems to disentangle changes caused by a fundamental biophysical nonlinearity from changes by an adaptation process.

A further study where the inclusion of a basic biophysical mechanism allowed improving the LN-model was provided by Pillow et al. (2005): To account for the dynamics and variability of spike generation, a noisy integrate-and-fire model driven by the linearly filtered stimulus and a post-spike current was fit and, thus, reproduced the reliability and selectivity of primate retinal ganglion cells.

## 4.4 Gain Modulation in Spiking Neurons

The biophysically extended LN-model captures the divisive (gain) and additive (selectivity) modulation of the input-output relation by the density of presented dots, thereby relying on the dendritic integration of synaptic inputs from local motion detectors in a finite cable (see Section 3.1). The current flowing in response to the presented stimuli is then transformed to the firing rate. Previously, however, it has been stated that, although changes in the membrane conductance can have a divisive effect on the membrane potential (Borst et al., 1995), they mainly act subtractive (or additive) on the neural firing rate (Holt and Koch, 1997). More recently, it has been shown that an increase of excitatory and inhibitory synaptic noise can also lead to a divisive modulation of the neural gain of a spiking cell (Chance et al., 2002). This type of gain modulation results from the combination of a subtractive shift of the neural input-output relation and the lowering of the spiking threshold due to the overall increase of synaptic input noise. A prerequisite of the presented biophysical model to exhibit a divisive effect on the firing rate is a large electrotonic distance between dendrite and spike initiation zone (axon). The large electrotonic distance effectively segregates the neuron into a dendritic and axonal compartment. As shown in Holt and Koch (1997), if the spike initiation zone and dendrite are not separated (as for a simple integrate-and-fire neuron), the excitatory and inhibitory conductances have no

divisive effect on the firing rate. Thus, the degree to which a neuron is electrically separated into a dendritic and axonal compartment determines, how strongly the gain and selectivity are affected by incoming synaptic inputs. This finding suggests that a pronounced neural compartmentalization might be generally advantageous for sensory neurons that need to adjust their dynamic coding range to the actual stimulus strength as the mean luminance, contrast, or motion density.

The input conductance of the finite cable (which is proportional to the parameter  $c$  in Equation 3.1) determines how strongly the gain is modulated by the total synaptic input. Interestingly, the baseline potential of the tangential cells in tethered flies has been shown to rise during flight (Maimon et al., 2010). This potential shift indicates an increased synaptic input to the tangential cells, thus increasing their input conductance. Consequently, during flight the neural gain might be even stronger affected by the amount of synaptic input, making the cells highly sensitive to variations in the strength and density of motion cues. The divisive modulation of the input-output relation adjusts the response range of the tangential cells to the global stimulus strength determined by the current motion density. This gain control mechanism can be interpreted as a normalization of the summed local dot velocities by the global stimulus strength. The summed local velocities as computed by the local motion detectors are thereby divided by the global stimulus strength as reflected in the total synaptic input from pre-synaptic motion detectors. Various studies have pointed out the importance of divisive normalization for explaining the tuning properties of cortical visual neurons (Carandini and Heeger, 1994; Rust et al., 2006), the processing of natural images (Schwartz and Simoncelli, 2001), and olfactory signals (Borst, 1983; Olsen et al., 2010). Models for divisive normalization typically assume that the response of a single neuron to a local stimulus is divided by the summed population activity, thus accounting for the global stimulus strength (as e.g. the mean luminance or contrast) of the surrounding scene. Shunting through an inhibitory feedback synapse has been proposed as a possible biophysical implementation of divisive normalization (Carandini and Heeger, 1994). Recent experimental studies showed that global inhibition underlies normalization of neurons in hippocampus and somato-sensory cortex (Pouille et al., 2009) as well as of projection neurons in the olfactory pathway of flies (Olsen et al., 2010). To adjust the neural gain by the overall strength of synaptic inputs, the presented model incorporates a divisive normalization mechanism relying on a feedforward architecture. In case of the tangential cells, the integration of synaptic inputs from pre-synaptic detectors already seems to be sufficient to adjust the neural coding range to the global stimulus strength and, thus, does not require a further global inhibitory mechanism. Such a feedforward model for divisive normalization might be a consequence of the large receptive field size of optic-

flow processing neurons: The receptive field of a single neuron is already large enough to reliably estimate the global stimulus strength without having to rely on the activity of neighboring cells. In this respect, it would be interesting to investigate, how neurons with large receptive fields in other systems such as cortical area MST or the accessory optic system in birds adjust their gain to the global stimulus strength.

## 4.5 Rotation and Translation Encoding by the Tangential Cells

In the experiments with the white-noise self-motion stimuli I found that rotations are better represented in the responses of the lobula plate tangential cells than translations (see Section 3.2).

This result is in line with a recent simulation study which showed that the strong resemblance of the receptive fields with rotational optic-flow patterns reduces the sensitivity to translations (Borst and Weber, 2011). To illustrate this finding Figure 4.2B depicts the rotation and translation tuning of an artificial cell whose receptive field was identical to the flow-field for a rotation about the x-axis. The rotation tuning of this ideal rotation sensor was calculated by the dot product between the receptive field and the flow fields induced by rotations around various body axis in a rectangular room. The flow fields were estimated by a two-dimensional array of Reichardt detectors. The response strength to a particular rotation or translation axis is color-coded on a sphere (Figure 4.2B). While the optimal rotation sensor exhibits a clear rotation tuning with a preference for rotations about the x-axis, it is insensitive to translations. Contrarily, an optimal translation sensor with a receptive field identical to a flow field resulting from a forward translation is insensitive to any rotation (Figure 4.2C). Hence, the rotational structure of the fly neurons' receptive fields might reduce their sensitivity to translations.

With the white-noise self-motion stimulus I tested the robustness of the self-motion encoding by the tangential cells. To this end, I confronted the flies with different environments to deliberately make it difficult to estimate the current self-motion. However, although this approach allowed studying the system at a variety of conditions, it is difficult to relate phenomena as changes in the linear filters or the nonlinearities to the underlying physiology. Contrarily, the Brownian motion stimulus was such designed that changes in the neural gain and selectivity could be related to changes in the cells' biophysical properties. This was possible, since for both presented stimulus conditions (sparse and dense motion), the stimuli did not differ locally. Hence, any changes in the processing were more likely to

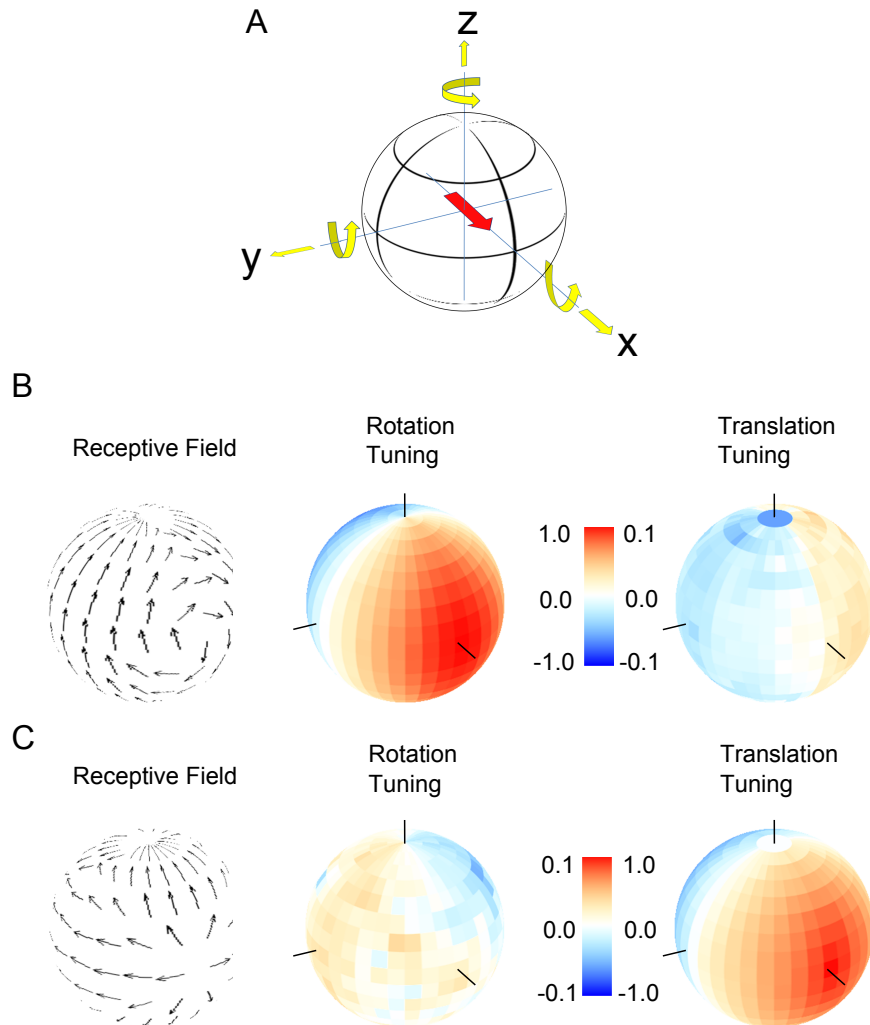


**Figure 4.2: Rotational and Translational Action Field of an Ideal Rotation and Translation Sensor.** (A) Definition of translation and rotation axes. The red arrow indicates the viewing direction of the fly. (B) Receptive field of an ideal rotation sensor for x-rotations (left). The rotation tuning is depicted by the coloring of the sphere. The rotation sensor responds strongest to rotations about the x-axis. Contrarily, it is nearly insensitive to translations along any axis. The black lines indicate x-, y-, and z-rotation axis or the x-, y-, and z-translation axis. (C) Receptive field of an ideal translation sensor. Its rotational tuning is weak for all rotation axes. Contrarily, its translation tuning is strong with a peak for forward translations. Figure modified from Borst and Weber (2011).

happen at the level of the tangential cells, where local motion signals are integrated, than in the pre-synaptic local motion detectors. However, in case of the self-motion stimulus, modulations of the gain or the linear filters could not be related to changes of the properties in the local motion detectors or in the physiology of the tangential cells. Moreover, it cannot be judged whether the observed gain modulation is large, or whether it is actually small due to the presence of an effective gain control mechanism at the level of the motion detectors or the lobula plate tangential cells. Hence, future models must include an Reichardt array simulating pre-synaptic elements and account for fundamental biophysical nonlinearities at the level of the tangential cells to better understand the physiological basis of phenomenological changes in the LN-models.

## 4.6 Receptive Fields and Generative Models

The functional properties of sensory neurons are traditionally studied using receptive fields which describe the general stimulus selectivity and sensitivity of a neuron (Rieke et al., 1999; Dayan and Abbott, 2001; Wu et al., 2006). The coupling between H1 and Vi is an example of an interaction whose effect is not expressed in the receptive fields of both neurons (see Section 3.3). Nevertheless, I found that the interaction between Vi and H1 improves Vi's stimulus encoding. However, the strength of motion sensitivities on the contralateral side of Vi's receptive field suggests, if at all, only a weak impact of neurons from the right lobula plate onto the left Vi cell. Although it might be possible to show via statistical tests that the contralateral motion sensitivities are non-zero, the significance of this interaction and the mechanism underlying the improved stimulus encoding cannot be deduced from the receptive field. Intriguingly, the reason why the interaction of the two neurons is not visible in Vi's receptive field relies on this mechanism: The input from H1 enhances the optic-flow encoding only if it is correlated with Vi's activity. However, typical protocols to map spatial receptive fields either employ local stimuli (e.g. (Krapp and Hengstenberg, 1996)) or global, spatially uncorrelated stimuli (e.g. (Marmarelis and Marmarelis, 1978; Weber et al., 2010; Wu et al., 2006)): Local stimuli are too weak to drive H1 strongly enough to excite Vi, whereas uncorrelated input from H1 due to uncorrelated stimulation does not influence Vi's stimulus encoding. Thus, receptive fields only show the impact of feedforward or lateral inputs whose effect on the neural firing rate does not depend on higher-order correlations. Hence, directly estimating the connectivity of neurons using a generative model permits to address the impact of neural interactions which might be largely missed in classical receptive field studies.

## 4.7 Noise Correlations and Generative Models

Especially in sensory cortex and the retina, correlations between simultaneously recorded neurons have been intensively studied with the aim to understand their impact on stimulus processing (Bair et al., 2001; Seung and Sompolinsky, 1993; Zohary et al., 1994) and to infer the structure and dynamics of the underlying connectivity (Kohn and Smith, 2005; Moore et al., 1970; Smith and Kohn, 2008; Takeuchi et al., 2011). Correlations induced by similar stimulus selectivity are typically removed yielding the so-called noise correlation (Brody, 1999). This quantity is used to study the size, temporal scale and directionality of the coupling between the correlated neurons. However, the exact value of the noise correlations is influenced by various factors as the temporal scale over which it is computed (Cohen and Kohn, 2011), the neural mean firing rates (de la Rocha et al., 2007), the behavioral state (Cohen and Maunsell, 2009; Takeuchi et al., 2011) and global activity changes that are often difficult to detect and account for (Brody, 1999). To avoid these problems with noise correlations, I pursued a model-based approach: I fitted a generative model to the recorded spike trains which explicitly accounts for various factors affecting the neuron's firing rate: The stimulus, spiking dynamics and lateral connectivity. The coupling filters allow for a direct quantification of the size and temporal scale of horizontal connections. Moreover, modifying model components as the coupling filter allows studying their impact on stimulus processing, and, thus, gives a more direct insight in the functional role of horizontal interactions.

Model-based approaches to understand the role of correlations were previously applied in studies on populations of retinal ganglion cells (Pillow et al., 2008; Schneidman et al., 2006; Shlens et al., 2006). These studies effectively described correlations by fitting models which account for pairwise neural interactions. The resulting models allowed exploring more directly the functional impact of correlations on the neural population activity, and, thus, identified the structure of the functional connectivity underlying population codes in the retina. Knowing the correlational structure of the neural code permits formulating constraints on optimal strategies for decoding the population activity, and, thus, outlines possible computations performed in upstream areas (Averbeck et al., 2006): It has been shown that a decoder which accounts for the correlations in the retina yields about 20% better stimulus reconstructions than a decoder which assumes that retinal ganglion cells are independent (Pillow et al., 2008). Moreover, knowing the structure and organization of functional interactions allows better constraining the components of generative models (Stevenson and Kording, 2011). However, previous model-based studies could not relate the correlated activity to specific synaptic couplings. Rather the functional connectivity

reflected correlations induced not only by lateral connectivity, but also by common feed-forward input, overlapping receptive fields or shared noise (Shlens et al., 2006). Hence, although these studies could not establish a link between existent physical couplings and their impact on stimulus processing. To circumvent this problem I explicitly chose a pair of identified neurons located in opposite brain hemispheres which could, thus, be independently stimulated via the left and right eye. The identified connectivity underlying the response correlations is also purely functional in the sense that it replaces an indirect coupling from H1 to Vi by a single filter. This filter can be directly related to an existent, synaptic interaction of two neurons and captures the directionality, dynamics and stimulus dependence of this interaction.

## 4.8 Dependence of Functional Connectivity on Stimulation Strength

Previous studies reported that the correlation between neurons in visual cortex depend on the stimulus strength (Nauhaus et al., 2009; Kohn and Smith, 2005). In Nauhaus et al. (2009), it was found that the distance travelled by a local-field potential (LFP) wave induced by a spike is reduced with increasing stimulus contrast. This effect suggests that under strong stimulus conditions neurons in the visual cortex are more driven by feedforward input than lateral connections. This is in line with our finding that the amplitude of the coupling filter is reduced with increasing stimulus strength (see Section 3.3). Hence, it seems that under conditions where there is strong evidence about the external stimulus, the activity of sensory neurons relies more on direct feedforward input. However, in situations where information about stimuli is less clear, responses of sensory neurons depend more on lateral connections. Hence, under such conditions, the lateral connectivity might be interpreted as a prior that accounts for the missing evidence from the sensory organs (Tkacik et al., 2010). The larger the noise in the input, the larger is the impact of the prior (coupling) on the neuron's response. Such a mechanism is only beneficial if the prior reflects the statistics of the encoded stimuli. E.g. the coupling filter between Vi and H1 only improves the stimulus representation in Vi, if an increased activity in H1 implies a rotation, which is also similar to Vi's preferred rotation axis. This condition is indeed fulfilled, since Vi and H1 are stimulus correlated for rotations. The biophysical mechanism underlying changes in the coupling strength between Vi and H1 and a thorough probabilistic interpretation of these findings will be the subject of future research.

## 4.9 Role of Correlations in Sensory Areas

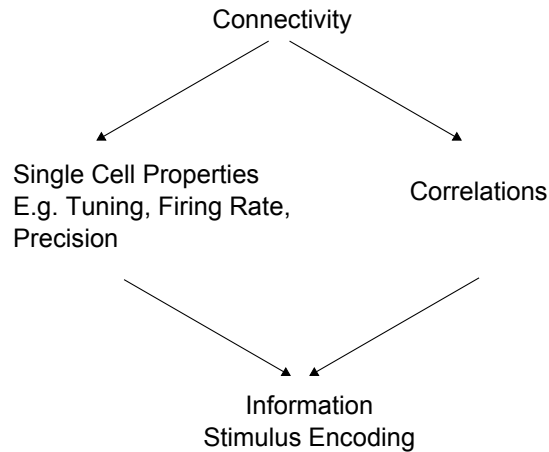


**Figure 4.3: Connectivity, Single Cell Properties, and Correlations.** Correlations are one of many effects resulting from lateral interactions between neurons. The underlying connectivity induces correlations, but also affects the computations in single neurons by changing their tuning, firing rate, or precision. Correlations between pairs of neurons and changes on the single neuron level must be both taken into account, when trying to understand how the connectivity in sensory areas influences stimulus processing.

Vi and H1 have different receptive fields and, correspondingly, respond preferentially to different optic-flow patterns. Therefore, coupling H1 to Vi might be assumed to shift Vis rotation tuning. However, although the coupling improves Vis stimulus encoding, its tuning is nearly unchanged. This effect relies on two factors: Vi and H1 are stimulus-correlated and the coupling is weak such that uncorrelated input from H1 does not significantly affect Vis stimulus encoding. Hence, more generally, positively coupling two neurons with similar stimulus selectivity should improve the stimulus representation in single neurons. Indeed, it has been found in visual cortex that neurons with similar direction or orientation have a higher likelihood to be connected (Ko et al., 2011) and their correlations increase with similarity of preferred stimuli (Kohn and Smith, 2005).

However, it has been demonstrated that positive correlations between stimulus-correlated neurons restrict the total amount of information carried by the whole population (Averbek et al., 2006; Zohary et al., 1994). From this perspective, positive couplings between neurons appear disadvantageous and, thus, might represent a factor limiting the strength of lateral interactions. However, in most cases it is unclear to what extent the connectivity underlying the correlations affects the properties of single neurons. It has been previously demonstrated that the lateral inputs of a neuron can change its receptive field (Farrow

et al., 2005), precision (Cafaro and Rieke, 2010) or gain (Olsen and Wilson, 2008). All these factors affect the stimulus processing, too. Thus, correlations between neurons are just one of many factors that constrain how neurons should be coupled to optimally process stimuli 4.3. Hence, a more thorough discussion of the effects of correlations should directly focus on the underlying connectivity and trade the resulting beneficial computations against potentially negative effects as correlated noise. This requires a systems approach that either allows separately activating feedforward and lateral input lines as it was the case for Vi and H1 or to directly manipulate the inputs to neurons (Cafaro and Rieke, 2010; Elyada et al., 2009). I am convinced, that for the future, a combination of careful sensory stimulation, targeted stimulation of interacting partners, and analysis of generative models will deepen our understanding of the connectivity in a variety of systems.

# Bibliography

- A.M. Aertsen and P.I. Johannesma. The spectro-temporal receptive field. A functional characteristic of auditory neurons. *Biol Cybern*, 42:133–143, 1981.
- M.B. Ahrens, J.F. Linden, and M. Sahani. Nonlinearities and contextual influences in auditory cortical responses modeled with multilinear spectrotemporal methods. *J Neurosci*, 28:1929–1942, 2008.
- T.D. Albright. Direction and orientation selectivity of neurons in visual area MT of the macaque. *J Neurophysiol*, 52:1106–1130, 1984.
- S. Atiani, M. Elhilali, S.V. David, J.B. Fritz, and S.A. Shamma. Task difficulty and performance induce diverse adaptive patterns in gain and shape of primary auditory cortical receptive fields. *Neuron*, 61:467–480, 2009.
- B.B. Averbeck, P.E. Latham, and A. Pouget. Neural correlations, population coding and computation. *Nat Rev Neurosci*, 7:358–366, 2006.
- B. Babadi, A. Casti, Y. Xiao, E. Kaplan, and L. Paninski. A generalized linear model of the impact of direct and indirect inputs to the lateral geniculate nucleus. *J Vis*, 10:22, 2010.
- W. Bair and J.A. Movshon. Adaptive temporal integration of motion in direction-selective neurons in macaque visual cortex. *J Neurosci*, 24:7305–7323, 2004.
- W. Bair, E. Zohary, and W.T. Newsome. Correlated firing in macaque visual area MT: Time scales and relationship to behavior. *J Neurosci*, 21:1676–1697, 2001.
- B. Bausenwein and K.F. Fischbach. Activity labeling patterns in the medulla of *Drosophila melanogaster* caused by motion stimuli. *Cell Tissue Res*, 270:25–35, 1992.

- B. Bausenwein, A.P. Dittrich, and K.F. Fischbach. The optic lobe of *Drosophila melanogaster*. II. Sorting of retinotopic pathways in the medulla. *Cell Tissue Res*, 267: 17–28, 1992.
- D.G.M. Beersma, D.G. Stavenga, and J.W. Kuiper. Retinal lattice, visual field and binocularities in flies. *J Comp Physiol*, 119:207–220, 1977.
- O. Bernander, C. Koch, and R.J. Douglas. Amplification and linearization of distal synaptic input to cortical pyramidal cells. *J Neurophysiol*, 72:2743–2753, 1994.
- M.J. Berry and M. Meister. Refractoriness and neural precision. *J Neurosci*, 18:2200–2211, 1998.
- C.M. Bishop. *Pattern Recognition and Machine Learning*. Springer, Berlin, 2008.
- A. Borst. Computation of olfactory signals in *Drosophila melanogaster*. *J Comp Physiol A*, 152:373–383, 1983.
- A. Borst. Noise, not stimulus entropy, determines neural information rate. *J Comput Neurosci*, 14:23–31, 2003.
- A. Borst and M. Egelhaaf. Direction selectivity of blowfly motion-sensitive neurons is computed in a two-stage process. *Proc Natl Acad Sci USA*, 87:9363–9367, 1990.
- A. Borst and J. Haag. The intrinsic electrophysiological characteristics of fly lobula plate tangential cells: I. Passive membrane properties. *J Comput Neurosci*, 3:313–336, 1996.
- A. Borst and J. Haag. Neural networks in the cockpit of the fly. *J Comp Physiol A*, 188: 419–437, 2002.
- A. Borst and J. Haag. *Invertebrate Neurobiology*, chapter Optic flow processing in the cockpit of the fly, pages 102–122. CSHL-Press, 2007.
- A. Borst and F.E. Theunissen. Information theory and neural coding. *Nat Neurosci*, 2: 947–957, 1999.
- A. Borst and F. Weber. Neural action fields for optic flow based navigation: A simulation study of the fly lobula plate network. *PLoS One*, 6:e16303, 2011.
- A. Borst, M. Egelhaaf, and J. Haag. Mechanisms of dendritic integration underlying gain control in fly motion-sensitive interneurons. *J Comput Neurosci*, 2:5–18, 1995.

- A. Borst, C. Reisenman, and J. Haag. Adaptation of response transients in fly motion vision. II: Model studies. *Vision Res*, 43:1309–1322, 2003.
- A. Borst, V.L. Flanagan, and H. Sompolinsky. Adaptation without parameter change: Dynamic gain control in motion detection. *Proc Natl Acad Sci USA*, 102:6172–6176, 2005.
- A. Borst, J. Haag, and D.F. Reiff. Fly Motion Vision. *Annu Rev Neurosci*, 33:49–70, 2010.
- V. Braitenberg. Patterns of projection in the visual system of the fly. I. Retina-Lamina projections. *Exp Brain Res*, 3:271–298, 1967.
- V. Braitenberg. Order and orientation of elements in the visual system of the fly. *Kybernetik*, 7:235–242, 1970.
- N. Brenner, W. Bialek, and R. de Ruyter van Steveninck. Adaptive rescaling maximizes information transmission. *Neuron*, 26:695–702, 2000.
- K.H. Britten. Mechanisms of self-motion perception. *Annu Rev Neurosci*, 31:389–410, 2008.
- C.D. Brody. Correlations without synchrony. *Neural Comput*, 11:1537–1551, 1999.
- T.M. Brotz and A. Borst. Cholinergic and GABAergic receptors on fly tangential cells and their role in visual motion detection. *J Neurophysiol*, 76:1786–1799, 1996.
- E. Buchner, S. Buchner, and I. Buelthoff. Deoxyglucose mapping of nervous activity induced in *Drosophila* brain by visual movement. *J Comp Physiol A*, 155:471–483, 1984.
- D.A. Butts and M.S. Goldman. Tuning curves, neuronal variability, and sensory coding. *PLoS Biol*, 4:e92, 2006.
- J. Cafaro and F. Rieke. Noise correlations improve response fidelity and stimulus encoding. *Nature*, 468:964–967, 2010.
- M. Carandini and D.J. Heeger. Summation and division by neurons in primate visual cortex. *Science*, 264:1333–1336, 1994.
- M. Carandini, J.B. Demb, V. Mante, D.J. Tolhurst, Y. Dan, B.A. Olshausen, J.L. Gallant, and N.C. Rust. Do we know what the early visual system does? *J Neurosci*, 25:10577–10597, 2005.

- T. Carnevale and M. Hines. *The Neuron Book*. Cambridge University Press, 2006.
- F.S. Chance, L.F. Abbott, and A.D. Reyes. Gain modulation from background synaptic input. *Neuron*, 35:773–782, 2002.
- E.J. Chichilnisky. A simple white noise analysis of neuronal light responses. *Network*, 12:199–213, 2001.
- G.B. Christianson, M. Sahani, and J.F. Linden. The consequences of response nonlinearities for interpretation of spectrotemporal receptive fields. *J Neurosci*, 28:446–455, 2008.
- M.R. Cohen and A. Kohn. Measuring and interpreting neuronal correlations. *Nat Neurosci*, 14:811–819, 2011.
- M.R. Cohen and J.H.R. Maunsell. Attention improves performance primarily by reducing interneuronal correlations. *Nat Neurosci*, 12:1594–1600, 2009.
- T. Cook and C. Desplan. Photoreceptor subtype specification: From flies to humans. *Semin Cell Dev Biol*, 12:509–518, 2001.
- H. Cuntz, A. Borst, and I. Segev. Optimization principles of dendritic structure. *Theor Biol Med Model*, 4:21, 2007.
- H. Cuntz, F. Forstner, J. Haag, and A. Borst. The morphological identity of insect dendrites. *PLoS Comput Biol*, 4:e1000251, 2008.
- S.V. David, W.E. Vinje, and J.L. Gallant. Natural stimulus statistics alter the receptive field structure of v1 neurons. *J Neurosci*, 24:6991–7006, 2004.
- P. Dayan and L.F. Abbott. *Theoretical Neuroscience*. MIT Press, 2001.
- J. de la Rocha, B. Doiron, E. Shea-Brown, K. Josic, and A. Reyes. Correlation between neural spike trains increases with firing rate. *Nature*, 448:802–806, 2007.
- G.C. DeAngelis, I. Ohzawa, and R.D. Freeman. Receptive-field dynamics in the central visual pathways. *Trends Neurosci*, 18:451–458, 1995.
- J.K. Douglass and N.J. Strausfeld. Visual motion detection circuits in flies: Peripheral motion computation by identified small-field retinotopic neurons. *J Neurosci*, 15:5596–5611, 1995.

- J.K. Douglass and N.J. Strausfeld. Visual motion-detection circuits in flies: Parallel direction- and non-direction-sensitive pathways between the medulla and lobula plate. *J Neurosci*, 16:4551–4562, 1996.
- C.J. Duffy and R.H. Wurtz. Multiple temporal components of optic flow responses in MST neurons. *Exp Brain Res*, 114:472–482, 1997.
- H. Eckert and DR. Dvorak. The centrifugal horizontal cells in the lobula plate of the blowfly *Phaenicia sericata*. *J Insect Physiol*, 29:547–560, 1983.
- M. Egelhaaf and A. Borst. Transient and steady-state response properties of movement detectors. *J Opt Soc Am A*, 6:116–127, 1989.
- M. Egelhaaf, A. Borst, and W. Reichardt. Computational structure of a biological motion-detection system as revealed by local detector analysis in the fly’s nervous system. *J Opt Soc Am A*, 6:1070–1087, 1989.
- H. Eichner, M. Joesch, B. Schnell, D.F. Reiff, and A. Borst. Internal structure of the fly elementary motion detector. *Neuron*, 70:1155–1164, 2011.
- Y.M. Elyada, J. Haag, and A. Borst. Different receptive fields in axons and dendrites underlie robust coding in motion-sensitive neurons. *Nat Neurosci*, 12:327–332, 2009.
- A.L. Fairhall, G.D. Lewen, W. Bialek, and R.R. de Ruyter Van Steveninck. Efficiency and ambiguity in an adaptive neural code. *Nature*, 412:787–792, 2001.
- K. Farrow, A. Borst, and J. Haag. Sharing receptive fields with your neighbors: Tuning the vertical system cells to wide field motion. *J Neurosci*, 25:3985–3993, 2005.
- K. Farrow, J. Haag, and A. Borst. Nonlinear, binocular interactions underlying flow field selectivity of a motion-sensitive neuron. *Nat Neurosci*, 9:1312–1320, 2006.
- G. Felsen, J. Touryan, F. Han, and Y. Dan. Cortical sensitivity to visual features in natural scenes. *PLoS Biol*, 3:e342, 2005.
- K.F. Fischbach and A.P.M. Dittrich. The optic lobe of *Drosophila melanogaster*. I. A Golgi analysis of wild-type structure. *Cell Tissue Research*, 258:441–475, 1989.
- M.O. Franz and H.G. Krapp. Wide-field, motion-sensitive neurons and matched filters for optic flow fields. *Biol Cybern*, 83:185–197, 2000.

- M.O. Franz, J.S. Chahl, and H.G. Krapp. Insect-inspired estimation of egomotion. *Neural Comput*, 16:2245–2260, 2004.
- S. Gao, S.-Y. Takemura, C.-Y. Ting, S. Huang, Z. Lu, H. Luan, J. Rister, A.S. Thum, M. Yang, S.-T. Hong, J.W. Wang, W.F. Odenwald, B.H. White, I.A. Meinertzhagen, and C.-H. Lee. The neural substrate of spectral preference in *Drosophila*. *Neuron*, 60: 328–342, 2008.
- M.N. Geffen, B.M. Broome, G. Laurent, and M. Meister. Neural encoding of rapidly fluctuating odors. *Neuron*, 61:570–586, 2009.
- G. Geiger and D.R. Naessl. Visual orientation behavior of flies after selective laser beam ablation of interneurons. *Nature*, 293:398–399, 1981.
- S. Gerwinn, J.H. Macke, and M. Bethge. Bayesian inference for generalized linear models for spiking neurons. *Front Comput Neurosci*, 4:12, 2010.
- J.J. Gibson. *Perception of the Visual World*. Boston: Houghton-Mifflin, 1950.
- J. Grewe, N. Matos, M. Egelhaaf, and A.-K. Warzecha. Implications of functionally different synaptic inputs for neuronal gain and computational properties of fly visual interneurons. *J Neurophysiol*, 96:1838–1847, 2006.
- J. Haag and A. Borst. Encoding of visual motion information and reliability in spiking and graded potential neurons. *J Neurosci*, 17:4809–4819, 1997.
- J. Haag and A. Borst. Recurrent network interactions underlying flow-field selectivity of visual interneurons. *J Neurosci*, 21:5685–5692, 2001.
- J. Haag and A. Borst. Orientation tuning of motion-sensitive neurons shaped by vertical-horizontal network interactions. *J Comp Physiol A Neuroethol Sens Neural Behav Physiol*, 189:363–370, 2003.
- J. Haag and A. Borst. Reciprocal inhibitory connections within a neural network for rotational optic-flow processing. *Front Neurosci*, 1:111–121, 2007.
- J. Haag and A. Borst. Electrical coupling of lobula plate tangential cells to a heterolateral motion-sensitive neuron in the fly. *J Neurosci*, 28:14435–14442, 2008.
- J. Haag, A. Vermeulen, and A. Borst. The intrinsic electrophysiological characteristics of fly lobula plate tangential cells: III. Visual response properties. *J Comput Neurosci*, 7: 213–234, 1999.

- J. Haag, W. Denk, and A. Borst. Fly motion vision is based on Reichardt detectors regardless of the signal-to-noise ratio. *Proc Natl Acad Sci USA*, 101:16333–16338, 2004.
- K. Hausen. Motion sensitive interneurons in the optomotor system of the fly. I. The horizontal cells: Structure and signals. *Biol Cybern*, 45:143–156, 1982a.
- K. Hausen. Motion sensitive interneurons in the optomotor system of the fly. II. The horizontal cells: Receptive field organization and response characteristics. *Biol Cybern*, 46:67–79, 1982b.
- K. Hausen. *Photoreception and Vision in Invertebrates*, chapter The lobula-complex of the fly: Structure, function and significance in visual behaviour, pages 523–559. Plenum Press, New York, 1984.
- K. Hausen and C. Wehrhahn. Microsurgical lesion of horizontal cells changes optomotor yaw response in the blowfly *Calliphora erythrocephala*. *Proc R Soc London Ser B*, 219: 211–216, 1983.
- M. Heisenberg and E. Buchner. The role of retinula cell types in visual behavior of *Drosophila melanogaster*. *J Comp Physiol A*, 117:127–162, 1977.
- M. Heisenberg, R. Wonneberger, and R. Wolf. Optomotor-blind (H31): A *Drosophila* mutant of the lobula plate giant neurons. *J Comp Physiol A*, 124:287–296, 1978.
- R. Hengstenberg, K. Hausen, and B. Hengstenberg. The number and structure of giant vertical cells (VS) in the lobula plate of the blowfly *Calliphora erythrocephala*. *J Comp Physiol A*, 149:163–177, 1982.
- G.H. Henry, B. Dreher, and P.O. Bishop. Orientation specificity of cells in striate cortex. *J Neurophysiol*, 37:1394–1409, 1974.
- G.R. Holt and C. Koch. Shunting inhibition does not have a divisive effect on firing rates. *Neural Comput*, 9:1001–1013, 1997.
- W. Horstmann, M. Egelhaaf, and A.K. Warzecha. Synaptic interactions increase optic flow specificity. *Eur J Neurosci*, 12:2157–2165, 2000.
- D. H. Hubel and T. N. Wiesel. Receptive fields and functional architecture of monkey striate cortex. *J Physiol*, 195:215–243, 1968.

- S.J. Huston and H.G. Krapp. Visuomotor transformation in the fly gaze stabilization system. *PLoS Biol*, 6:e173, 2008.
- M. Joesch, J. Plett, A. Borst, and D.F. Reiff. Response properties of motion-sensitive visual interneurons in the lobula plate of *Drosophila melanogaster*. *Curr Biol*, 18:368–374, 2008.
- M. Joesch, B. Schnell, S.V. Raghu, D.F. Reiff, and A. Borst. ON and OFF pathways in *Drosophila* motion vision. *Nature*, 468:300–304, 2010.
- H. Kazama and R.I. Wilson. Origins of correlated activity in an olfactory circuit. *Nat Neurosci*, 12:1136–1144, 2009.
- K. Kirschfeld. *Information Processing in the Visual Systems of Arthropods*, chapter The visual system of Musca: Studies on optics, structure and function, pages 61–74. Berlin, Heidelberg, New York: Springer, 1972.
- H. Ko, S.B. Hofer, B. Pichler, K.A. Buchanan, P.J. Sjöström, and T.D. Mrsic-Flogel. Functional specificity of local synaptic connections in neocortical networks. *Nature*, 2011.
- C. Koch, O. Bernander, and R.J. Douglas. Do neurons have a voltage or a current threshold for action potential initiation? *J Comput Neurosci*, 2:63–82, 1995.
- J.J. Koenderink and A.J. van Doorn. Facts on optic flow. *Biol Cybern*, 56:247–254, 1987.
- A. Kohn and M.A. Smith. Stimulus dependence of neuronal correlation in primary visual cortex of the macaque. *J Neurosci*, 25:3661–3673, 2005.
- H.G. Krapp and R. Hengstenberg. Estimation of self-motion by optic flow processing in single visual interneurons. *Nature*, 384:463–466, 1996.
- H.G. Krapp, B. Hengstenberg, and R. Hengstenberg. Dendritic structure and receptive-field organization of optic flow processing interneurons in the fly. *J Neurophysiol*, 79:1902–1917, 1998.
- H.G. Krapp, R. Hengstenberg, and M. Egelhaaf. Binocular contributions to optic flow processing in the fly visual system. *J Neurophysiol*, 85:724–734, 2001.
- R. Kurtz, A.K. Warzecha, and M. Egelhaaf. Transfer of visual motion information via graded synapses operates linearly in the natural activity range. *J Neurosci*, 21:6957–6966, 2001.
- M.F. Land. Visual acuity in insects. *Annu Rev Entomol*, 42:147–177, 1997.

- N.A. Lesica, J. Jin, C. Weng, C.-I. Yeh, D.A. Butts, G.B. Stanley, and J.-M. Alonso. Adaptation to stimulus contrast and correlations during natural visual stimulation. *Neuron*, 55:479–491, 2007.
- J.P. Lindemann, R. Kern, J.H. van Hateren, H. Ritter, and M. Egelhaaf. On the computations analyzing natural optic flow: Quantitative model analysis of the blowfly motion vision pathway. *J Neurosci*, 25:6435–6448, 2005.
- J.F. Linden, R.C. Liu, M. Sahani, C.E. Schreiner, and M.M. Merzenich. Spectrotemporal structure of receptive fields in areas AI and AAF of mouse auditory cortex. *J Neurophysiol*, 90:2660–2675, 2003.
- C.K. Machens, M.S. Wehr, and A.M. Zador. Linearity of cortical receptive fields measured with natural sounds. *J Neurosci*, 24:1089–1100, 2004.
- G. Maimon, A.D. Straw, and M.H. Dickinson. Active flight increases the gain of visual motion processing in *Drosophila*. *Nat Neurosci*, 13:393–399, 2010.
- P.Z. Marmarelis and V.Z. Marmarelis. *Analysis of physiological systems: The white-noise approach*. Plenum Press, New York, 1978.
- I.A. Meinertzhagen and S.D. O’Neil. Synaptic organization of columnar elements in the lamina of the wild type in *Drosophila melanogaster*. *J Comp Neurol*, 205:232–263, 1991.
- G.P. Moore, J.P. Segundo, D.H. Perkel, and H. Levitan. Statistical signs of synaptic interaction in neurons. *Biophys J*, 10:876–900, 1970.
- I. Nauhaus, L. Busse, M. Carandini, and D.L. Ringach. Stimulus contrast modulates functional connectivity in visual cortex. *Nat Neurosci*, 12:70–76, 2009.
- M. Okatan, M.A. Wilson, and E.N. Brown. Analyzing functional connectivity using a network likelihood model of ensemble neural spiking activity. *Neural Comput*, 17:1927–1961, 2005.
- S.R. Olsen and R.I. Wilson. Lateral presynaptic inhibition mediates gain control in an olfactory circuit. *Nature*, 452:956–960, 2008.
- S.R. Olsen, V. Bhandawat, and R.I. Wilson. Divisive normalization in olfactory population codes. *Neuron*, 66:287–299, 2010.

- J.E. O'Tousa, W. Baehr, R.L. Martin, J. Hirsh, W.L. Pak, and M.L. Applebury. The *Drosophila ninaE* gene encodes an opsin. *Cell*, 40:839–850, 1985.
- L. Paninski, J. Pillow, and J. Lewi. Statistical models for neural encoding, decoding, and optimal stimulus design. *Progress In Brain Research*, Unkown:1–3, 2007.
- M. Paolini, C. Distler, F. Bremmer, M. Lappe, and K.P. Hoffmann. Responses to continuously changing optic flow in area MST. *J Neurophysiol*, 84:730–743, 2000.
- R. Petrowitz, H. Dahmen, M. Egelhaaf, and H.G. Krapp. Arrangement of optical axes and spatial resolution in the compound eye of the female blowfly *Calliphora*. *J Comp Physiol A*, 186:737–746, 2000.
- J.W. Pillow, L. Paninski, V.J. Uzzell, E.P. Simoncelli, and E.J. Chichilnisky. Prediction and decoding of retinal ganglion cell responses with a probabilistic spiking model. *J Neurosci*, 25:11003–11013, 2005.
- J.W. Pillow, J. Shlens, L. Paninski, A. Sher, A.M. Litke, E.J. Chichilnisky, and E.P. Simoncelli. Spatio-temporal correlations and visual signalling in a complete neuronal population. *Nature*, 454:995–999, 2008.
- F. Pouille, A. Marin-Burgin, H. Adesnik, B.V. Atallah, and M. Scanziani. Input normalization by global feedforward inhibition expands cortical dynamic range. *Nat Neurosci*, 12:1577–1585, 2009.
- K.P. Purpura, J.D. Victor, and E. Katz. Striate cortex extracts higher-order spatial correlations from visual textures. *Proc Natl Acad Sci USA*, 91:8482–8486, 1994.
- W. Rall. *Neural Theory and Modeling*, chapter Theoretical significance of dendritic trees for neuronal input-output relations, pages 73–97. Stanford Univ. Press, Stanford, CA, 1964.
- W. Reichardt. *Sensory communication*, chapter Autocorrelation, a principle for the evaluation of sensory information by the central nervous system, pages 303–317. MIT Press and John Wiley & Sons, New York, London, 1961.
- D.F. Reiff, J. Plett, M. Mank, O. Griesbeck, and A. Borst. Visualizing retinotopic half-wave rectified input to the motion detection circuitry of *Drosophila*. *Nat Neurosci*, 13: 973–978, 2010.

- J.H. Reynolds and L. Chelazzi. Attentional modulation of visual processing. *Annu Rev Neurosci*, 27:611–647, 2004.
- F. Rieke, W. Bialek, and D. Warland. *Spikes*. Mit Press, 1999.
- D.L. Ringach, G. Sapiro, and R. Shapley. A subspace reverse-correlation technique for the study of visual neurons. *Vision Res*, 37:2455–2464, 1997.
- N.C. Rust, V. Mante, E.P. Simoncelli, and J.A. Movshon. How MT cells analyze the motion of visual patterns. *Nat Neurosci*, 9:1421–1431, 2006.
- M.N. Safran, V.L. Flanagan, A. Borst, and H. Sompolinsky. Adaptation and information transmission in fly motion detection. *J Neurophysiol*, 98:3309–3320, 2007.
- M. Sahani and J.F. Linden. *Advances in neural information processing systems*, chapter How linear are auditory cortical responses?, pages 109–116. MIT Press, Cambridge, MA, 2003.
- E. Schneidman, M.J. Berry, R. Segev, and W. Bialek. Weak pairwise correlations imply strongly correlated network states in a neural population. *Nature*, 440:1007–1012, 2006.
- B. Schnell, M. Joesch, F. Forstner, S.V. Raghu, H. Otsuna, K. Ito, A. Borst, and D.F. Reiff. Processing of horizontal optic flow in three visual interneurons of the *Drosophila* brain. *J Neurophysiol*, 103:1646–1657, 2010.
- D.P.A. Schulz and M. Carandini. An uncorrelated state for the cortex? *F1000 Biol Rep*, 2, 2010.
- O. Schwartz and E.P. Simoncelli. Natural signal statistics and sensory gain control. *Nat Neurosci*, 4:819–825, 2001.
- O. Schwartz, J.W. Pillow, N.C. Rust, and E.P. Simoncelli. Spike-triggered neural characterization. *J Vis*, 6:484–507, 2006.
- H.S. Seung and H. Sompolinsky. Simple models for reading neuronal population codes. *Proc Natl Acad Sci USA*, 90:10749–10753, 1993.
- J. Shlens, G.D. Field, J.L. Gauthier, M.I. Grivich, D. Petrusca, A. Sher, A.M. Litke, and E.J. Chichilnisky. The structure of multi-neuron firing patterns in primate retina. *J Neurosci*, 26:8254–8266, 2006.

- S. Single and A. Borst. Dendritic integration and its role in computing image velocity. *Science*, 281:1848–1850, 1998.
- S. Single, J. Haag, and A. Borst. Dendritic computation of direction selectivity and gain control in visual interneurons. *J Neurosci*, 17:6023–6030, 1997.
- M.A. Smith and A. Kohn. Spatial and temporal scales of neuronal correlation in primary visual cortex. *J Neurosci*, 28:12591–12603, 2008.
- I.H. Stevenson and K.P. Kording. How advances in neural recording affect data analysis. *Nat Neurosci*, 14:139–142, 2011.
- N.J. Strausfeld. *Atlas of an Insect Brain*. Berlin/Heidelberg: Springer, 1976.
- N.J. Strausfeld. *Photoreception and vision in invertebrates*, chapter Functional neuroanatomy of the blowfly’s visual system, pages 483–522. Plenum Publishing Corporation, 1984.
- N.J. Strausfeld. *Facets of Vision*, chapter Beneath the compound eye: Neuroanatomical analysis and physiological correlates in the study of insect vision, pages 317–359. Springer, Berlin Heidelberg New York, 1989.
- N.J. Strausfeld and J.K. Lee. Neuronal basis for parallel visual processing in the fly. *Visual Neuroscience*, 7:13–33, 1991.
- N.J. Strausfeld and H.S. Seyan. Convergence of visual, haltere, and prosternal inputs at neck motor neurons of *Calliphora erythrocephala*. *Cell Tissue Res*, 240:601–615, 1985.
- N.J. Strausfeld, H.S. Seyan, and J.J. Milde. The neck motor system of the fly *Calliphora erythrocephala*. *J Comp Physiol A*, 160:205–224, 1987.
- D. Takeuchi, T. Hirabayashi, K. Tamura, and Y. Miyashita. Reversal of interlaminar signal between sensory and memory processing in monkey temporal cortex. *Science*, 331:1443–1447, 2011.
- F.E. Theunissen and J.P. Miller. Representation of sensory information in the cricket cercal sensory system. II. Information theoretic calculation of system accuracy and optimal tuning-curve widths of four primary interneurons. *J Neurophysiol*, 66:1690–1703, 1991.
- G. Tkacik, J.S. Prentice, V. Balasubramanian, and E. Schneidman. Optimal population coding by noisy spiking neurons. *Proc Natl Acad Sci USA*, 107:14419–14424, 2010.

- P.K. Trong and F. Rieke. Origin of correlated activity between parasol retinal ganglion cells. *Nat Neurosci*, 11:1343–1351, 2008.
- W. Truccolo, L.R. Hochberg, and J.P. Donoghue. Collective dynamics in human and monkey sensorimotor cortex: Predicting single neuron spikes. *Nat Neurosci*, 13:105–111, 2010.
- J.H. van Hateren, R. Kern, G. Schwerdtfeger, and M. Egelhaaf. Function and coding in the blowfly H1 neuron during naturalistic optic flow. *J Neurosci*, 25:4343–4352, 2005.
- H. von Helmholtz. *Treatise on physiological optics (1867)*. Rochester, New York: Optical Society of America, 1925.
- B. Wark, B.N. Lundstrom, and A. Fairhall. Sensory adaptation. *Curr Opin Neurobiol*, 17:423–429, 2007.
- F. Weber, H. Eichner, H. Cuntz, and A. Borst. Eigenanalysis of a neural network for optic flow processing. *New J Phys*, 10:1–21, 2008.
- F. Weber, C.K. Machens, and A. Borst. Spatiotemporal response properties of optic-flow processing neurons. *Neuron*, 67:629–642, 2010.
- A. Wertz, J. Haag, and A. Borst. Local and global motion preferences in descending neurons of the fly. *J Comp Physiol A Neuroethol Sens Neural Behav Physiol*, 195:1107–1120, 2009.
- R.I. Wilson, G.C. Turner, and G. Laurent. Transformation of olfactory representations in the *Drosophila* antennal lobe. *Science*, 303:366–370, 2004.
- M.C.-K. Wu, S.V. David, and J.L. Gallant. Complete functional characterization of sensory neurons by system identification. *Annu Rev Neurosci*, 29:477–505, 2006.
- D.R. Wylie, W.F. Bischof, and B.J. Frost. Common reference frame for neural coding of translational and rotational optic flow. *Nature*, 392:278–282, 1998.
- S. Yamaguchi, R. Wolf, C. Desplan, and M. Heisenberg. Motion vision is independent of color in *Drosophila*. *Proc Natl Acad Sci USA*, 105:4910–4915, 2008.
- S. Yamaguchi, C. Desplan, and M. Heisenberg. Contribution of photoreceptor subtypes to spectral wavelength preference in *Drosophila*. *Proc Natl Acad Sci USA*, 107:5634–5639, 2010.

R. Zbikowski. Fly like a fly. *IEEE Spectrum*, 42:46–51, 2005.

E. Zohary, M.N. Shadlen, and W.T. Newsome. Correlated neuronal discharge rate and its implications for psychophysical performance. *Nature*, 370:140–143, 1994.

# Acknowledgments

From the beginning of my studies, I always had the vague vision of combining neuroscience and computer science. So, I attended a seminar on Computational Neuroscience. From a list of topics, I chose computer simulations of neurons by the Hodgkin-Huxley model, simply because it sounded very computational. Luckily, my supervisor was this nice guy who always had an interesting story to tell about each seminar topic. After my seminar, he proposed me to do an internship in his lab. I did this one year later. That is how I got to know Alexander Borst and, I'm convinced that this was the best way to get to Neuroscience. Later on, I told Hubert that it's really cool there in the lab, he should also join for an internship. One year later, Christian Machens visited our department. I was impressed by what he did and enjoyed talking to him. Once I've heard that he plans to collaborate with Axel, I knew that is my PhD-project.

Many thanks to Axel! My thanks range from patiently introducing me to neuroscience, being a great supervisor, gently pushing me to experiments, till demonstrating that doing science makes you a fulfilled person. He always gave me the feeling that what I did and what I'm going to do is something special. It is really motivating to know that you can count on Axel as a scientist and person at any time.

Many thanks to Christian for being a great, inspiring supervisor! He definitely shaped the way how I want to combine theory and experiments. I enjoyed a lot his thought improvisations during skype sessions. What really impressed me: Every time I went to Paris, I doubted what we could get out of the data. But, after two weeks we had a clear story.

Many thanks to Hubert for creating a challenging, intellectual atmosphere in P7 (and let's keep still about less intellectual moments).

Many thanks to Marion! Thanks for these great years and the patience when I had the feeling that right now I have to do this experiment.

Many thanks to Friedrich and Armin for always being optimistic and demonstrating that there is never a reason to be in bad mood.

Many thanks to Johannes for designing the fly-arena, Mathias for making it even better, Max for his enthusiasm, Stefan Glasauer for forming my thesis committee meetings to interesting discussions. I'm grateful to Bulle for his scepticism and his incredible technical knowledge, to Dierk and his unique way to see the things, and to Bettina for being the most important contributor to the Fly Meeting. I want to thank Renate for keeping the flies alive and the whole Borst department and the Griesbeck group for a very harmonious and inspiring atmosphere.

Finally, I want to thank the Graduiertenkolleg 1091 (Orientation and Motion in Space) for financial support.

# Curriculum Vitae

## Franz Weber

Nationality German

Date of Birth April 10, 1982

## Education

2007-2011 PhD at the Graduate School of Systemic Neurosciences (LMU Munich),  
Max-Planck Institute of Neurobiology  
Supervised by Prof. Dr. Alexander Borst and Dr. Christian Machens  
*System Identification of Optic-Flow Processing Neurons in the Fly:  
Single Cell and Small Circuit Models*

2007-2009 Master of Science (M.Sc.) in Neurosciences, LMU Munich (Grade: 1.2)

2006-2007 Master Program in Computational Science and Engineering  
TU Munich

2003-2006 Bachelor in Bioinformatics, TU and LMU Munich (Grade: 1.4)

2002-2003 Master Program in Biology, University of Regensburg

## Awards

12/2010 Rosa Laura and Hartmut Wekerle Award

## Teaching

10/2008-02/2009 Tutor for a lecture in Computational Neuroscience, LMU Munich

05/2010 Supervision in a Practical Course for Animal Physiology, LMU Munich

## Conferences

- 02/2008 Computational and Systems Neuroscience (Cosyne), Salt Lake City, Utah, USA.  
Contribution: Poster
- 02/2011 Cosyne, Salt Lake City, Utah, USA.  
Contribution: Talk
- 09/2011 The Assembly and Function of Neuronal Circuits, Ascona, Switzerland.  
Contribution: Poster

## Courses

- 08/2010 Methods in Computational Neuroscience, Woods Hole, MA, USA.

## Publications

- F. Weber, H. Eichner, H. Cuntz, and A. Borst. Eigenanalysis of a neural network for optic flow processing. *New J Phys* 10:1-21, 2008.
- F. Weber, C.K. Machens, and A. Borst. Spatiotemporal response properties of optic-flow processing neurons. *Neuron* 67(4):629-642, 2010.
- A. Borst and F. Weber. Neural action fields for optic flow based navigation: A simulation study of the fly lobula plate network. *PLoS One* 6:e16303, 2011.
- F. Weber, C.K. Machens, and A. Borst. Disentangling the functional consequences of the connectivity between optic-flow processing neurons. *Submitted*, 2011.

## Ehrenwörtliche Versicherung

Ich versichere hiermit ehrenwörtlich, dass die vorgelegte Dissertation von mir selbständig und nur unter Verwendung der angegebenen Hilfsmittel angefertigt wurde.

---

Franz Weber  
München, den